Draft version August 3, 2026
Typeset using LaTeX **twocolumn** style in AASTeX7.0.2

A Catalog-Native DESIVAST Test of Classifier-Labelled Spiral Chirality in DESI DR1

Houston Golden[1]

[1] *Independent Researcher, Los Angeles, California, USA*

(Dated: August 3, 2026 (v0.1.147-2026-08-03))

ABSTRACT

We test whether *classifier-labelled* spiral chirality differs between released DESIVAST (14) void and non-void environments in DESI Data Release 1. The focal hybrid released-parent descriptive estimate intersects the companion Paper IV catalog (3) with the released DESIVAST GALZONE TARGET universe (694,642 unique TARGETIDs), yielding 145,789 joined rows. We retain the 145,766 rows with `OUT`$= 0$ as the quality parent and define the two arms by exact membership in the union of released VoidFinder holes: 31,937 void and 113,829 non-void. We standardize for redshift, imaging leg, magnitude, size, morphology, extinction, classifier confidence, and the GALZONE edge flag, with coarse sky blocks used as clusters. The focal adjusted non-void-minus-void contrast from a 13-column linear nuisance model is $\Delta f_{\rm CW} = +0.00145442$; a coarse HEALPix NSIDE$=4$ cluster-sandwich calculation gives SE $= 0.00331502$, 95% CI $[-0.00504290, +0.00795174]$, and two-sided normal $p = 0.66085$. A null-imposed 99,999-draw Rademacher wild-cluster efficient-score test gives $p = 0.67345$. Overlap weighting gives the same qualitative result. The author-constructed VoidFinder any-hole sample ($N_{\rm void} = 57{,}081$) and the T-Web, Tempel, and ASTRA analyses are sensitivity or secondary diagnostic paths rather than parallel focal measurements. This hierarchy was changed after review and after inspecting the data; the study remains exploratory, post-hoc, and not preregistered. T-Web intervals omit cosmic variance and spatial covariance, all environment assignments remain in redshift space, and a target-program-by-environment interaction is not excluded. The result is therefore a catalog-specific non-detection for classifier labels, not a physical-handedness, real-space, or cosmological constraint.

1. INTRODUCTION

Scope note. All environment labels are consumed or assigned in DESI DR1 redshift coordinates; no real-space reconstruction is performed (§13).

Spiral galaxy chirality is, to leading order in a parity-conserving universe, an equal mixture of clockwise (CW) and counterclockwise (CCW) projections on the sky once mirror-augmentation biases in classifier training are removed. The companion catalog paper (Paper IV) (3) (publicly archived on Zenodo under DOI 10.5281/zenodo.21461899; not peer reviewed; see [A1]; the present manuscript treats its public catalog and quoted monopole offset as inputs whose uncertainty is propagated explicitly below) establishes the global mixture in the post-test-time-augmentation equivariant classifier as a CW fraction of 0.4974 ± 0.000279 — a -0.26 pp monopole offset from exact parity that is statistically significant in pure counting terms ($\approx 9.5\sigma$) and is treated throughout Paper IV and this paper as a known classifier-monopole systematic reference, not a parity violation — while the Paper IV real-space *dipole* is consistent with isotropy at $+0.41\sigma$. That dipole null is a *global* statement; it does not constrain whether handedness is independent of *environment*.

The present paper is a focused, exploratory environment-conditional null test. We ask whether classifier labels differ between galaxies assigned to void and non-void environments in DESI redshift space. In the published literature reviewed for this analysis, we identify no bounce or inflation model that predicts a specific signal for this classifier-labelled, redshift-space estimand; the companion SPHEREx $f_{\rm NL}$ forecast (Paper II) (4) targets a distinct primordial-non-Gaussianity discriminant, not this catalog-labelled estimand. Accordingly, the analysis measures dataset- and classifier-specific DR1 sensitivity; it is not a real-space or physical handedness constraint and does not discriminate cosmological models.

The paper is organized around one focal hybrid released-parent descriptive estimate: the released DESIVAST GALZONE parent with `OUT`$= 0$, analyzed by covariate standardization and coarse-sky cluster-sandwich inference (Section 8). The author-defined VoidFinder point-in-sphere constructions are retained as sensitivities. T-Web, Tempel, ASTRA, and concurrent-catalog comparisons are secondary redshift-space diagnostics; they are not combined into a physical or real-space constraint.

The analysis was not preregistered, and the focal reporting hierarchy was changed after review from an author-constructed any-hole estimator to the released GALZONE-parent estimate. Section 5.2 records that post-hoc hierarchy and the full analysis tree. Throughout, the result is an exploratory controlled-sample non-detection, not evidence for environment-independence and not a physical, real-space, or model constraint.

2. RELATION TO PAPER IV

Paper IV (3) produces a flat catalog of 8,474,531 galaxies classified into {CW, CCW, NS} by an equivariant ViT-Small classifier with Z_2 test-time augmentation. The canonical labels live in the column `class_eq` of the HuggingFace catalog (bamfai/galaxy-chirality-catalog). The catalog inherits sky positions from DESI Legacy DR8 Tractor and is not redshift-resolved beyond Tractor photo-z; this paper supplies spectroscopic redshifts and environment context by joining to DESI Data Release 1.

Paper IV's headline results bear on the present paper in three ways. First, this paper independently measures the catalog-wide CW-fraction monopole within its own matched sample: $f_{\rm CW}^{\rm P5} = 0.49719$ on 812,793 env-labeled rows (Table 20), corresponding to $\Delta f_{\rm CW}^{\rm P5} \approx -0.0028$ — a spatially uniform, quality-quartile-flat classifier-residual bias consistent with the independent Paper IV estimate $\Delta f_{\rm CW}^{\rm P4} = -0.0026$ (the ∼8% enhancement is reconciled in §8.7). The per-class $\sigma_{\rm from\,half}$ values therefore inherit the same monopole offset, with sign determined by sample size. The headline two-sample $\Delta f_{\rm CW}$ classifier-label contrast is invariant under any catalog-wide monopole shift (§2): the $\sigma_{\rm pred}$ diagnostic rows (Tables 9, 10, 20) move with it, but the void/non-void null does not. Second, Paper IV's current headline is a real-space full-sky dipole null at $+0.41\sigma$ from direct amplitude estimation, reinforced by a weighted template fit that excludes a clean Shamir-amplitude (1.7%) dipole; an earlier harmonic-space subsample-mask MASTER-deconvolved $\ell = 1$ statistic was withdrawn in Paper IV after a provenance audit traced its mask to a synthetic footprint. Any environmental signal here would have to coexist with the re-anchored real-space null. Third, Paper IV provides the per-galaxy CW/CCW labels we test here; we make no independent classification. The per-galaxy catalog labels and the monopole offset consumed by this paper are unaffected by Paper IV's harmonic-channel revision.

3. DATA

3.1. *Chirality catalog (Paper IV)*

We use the HuggingFace galaxy chirality catalog, filtered to the chirality-relevant equivariant class ∈ {`CW`, `CCW`}. Imaging-leg provenance is retained for the per-leg systematics split in Section 11: BASS+MzLS, DECaLS, DES.

The present paper consumes two inputs from Paper IV: (i) the *per-galaxy* CW/CCW handedness labels (catalog column `class_eq`), and (ii) a single scalar, the catalog-wide CW-fraction monopole $\Delta f_{\rm CW}^{\rm P4} = -0.0026$. Table 1 states both with their values and provenance for self-contained referee assessment; the classifier architecture, training-set composition, parity-equivariance validation, independent accuracy floor, and the derivation of the monopole offset are summarized in Appendix A, with full details in Paper IV. The `class_eq` labels are the only Paper IV input the classifier-label non-detection depends on; the monopole scalar −0.0026 enters only the $\sigma_{\rm pred}$ diagnostics (Tables 9, 10, 20), where its uncertainty is propagated explicitly and independently corroborated by the internal P5 matched-sample value $f_{\rm CW}^{\rm P5} = 0.49719$ (§8.7).

Table 1. Paper IV inputs consumed by this analysis, summarized for self-contained readability. Values are reproduced from Paper IV (3) (companion catalog paper, publicly archived on Zenodo under DOI 10.5281/zenodo.21461899; not peer reviewed; full classifier architecture, training, parity-equivariance validation, and monopole origin summarized for self-contained assessment in Appendix A); labels are served as the `class_eq` column of the public catalog bamfai/galaxy-chirality-catalog. The per-galaxy `class_eq` labels are the only classifier input the focal contrast uses; the monopole amplitude enters only the $\sigma_{\rm pred}$ diagnostics.

Quantity	Value (as used here)
Catalog size	8,474,531 galaxies
Class labels	{`CW`, `CCW`, `NS`}
Classifier	equivariant ViT-Small, Z_2 TTA
Imaging input	DESI Legacy DR8 Tractor
legs	BASS+MzLS, DECaLS, DES
Label column consumed	`class_eq` ∈ {CW, CCW}
Matched CW/CCW subsample	791,635
Global CW monopole	$f_{\rm CW} = 0.4974 \pm 0.000279$
parity offset	$\Delta f_{\rm CW}^{\rm P4} = -0.0026$
counting significance	$\approx 9.5\sigma$
Real-space dipole (P4)	null, $+0.41\sigma$

3.2. *DESI Data Release 1*

We use the canonical `zall-pix-iron.fits` HEALPix-coadded redshift catalog from DESI DR1 (specprod tag `iron`, the DR1 spectroscopic reduction;

https://data.desi.lbl.gov/public/dr1/spectro/redux/iron/zcatalog/), restricted to ZWARN==0, SPECTYPE $\in$ {GALAXY, QSO}, and $0.01 \leq z \leq 4$. These quality cuts leave 16,361,731 rows — the "DR1 input" count quoted throughout this paper (and in the abstract as ZWARN=0 input rows) is this post-cut count, not the raw zall row total. Further restricting to SPECTYPE==GALAXY and the T-Web cosmic-web finder's tighter window $0.01 \leq z \leq 2.0$, the parent sample driving the T-Web tidal-tensor calculation is 14,622,283 galaxies. These row counts are *derived in this work* by applying our cuts to the DR1 zall catalog (not published DR1 constants); the fetch + filter driver is derived in this work.

3.3. *Cross-match method*

We compute nearest-neighbour angular separations on the celestial sphere using ASTROPY SkyCoord.match_to_catalog_sky. The primary acceptance radius is 1.0″ (DESI fiber positioning tolerance); sensitivity is reported at $\{0.5, 1.0, 2.0, 3.0, 5.0\}''$. Duplicates on the chirality side are resolved by nearest-separation winner; after this dedup the chirality-relevant subsample carries one row per DESI TARGETID (791,635 rows, 791,635 unique TARGETIDs — no many-to-one matches survive the join).

3.4. *Matched catalog summary*

Table 2 summarizes the 1″ matched catalog. The matched-primary count is 2,349,908 before dedup and 2,232,212 after. The chirality-relevant subsample is 791,635 galaxies. Median separation is 0.0066″ and the 99th-percentile separation is 0.30″, both well inside the 1.0″ acceptance. The 6.6-mas median is far below any independent-astrometry match precision and reflects shared coordinate provenance rather than astrometric match quality: the DESI TARGET_RA/TARGET_DEC coordinates are inherited directly from the DESI Legacy Imaging Surveys Tractor catalogs, and the Paper IV chirality-catalog coordinates derive from the same Legacy (DR8) Tractor astrometry, so matched pairs differ only at the coordinate-precision/rounding level. The 1.0″ acceptance radius is therefore conservative for this catalog pair. The $p_{99} = 0.30''$ tail reflects the small subset of objects whose coordinates were re-derived between data releases. Sensitivity to acceptance radius is mild: $\{0.5, 1.0, 2.0, 3.0, 5.0\}''$ produces $\{2.34, 2.35, 2.37, 2.39, 2.44\}\times10^6$ matched-primary rows, a $\leq 4\%$ band. The DESI SPECTYPE value is a spectral-template classification; it is not the imaging morphology label used to define CW/CCW. The 17,180 QSO-template rows in the full matched-primary ledger therefore do not imply that quasars were visually assigned spiral handedness. The frozen released-parent archive does not carry SPECTYPE, so no post-hoc QSO-exclusion rerun is asserted here.

Sample ledger. The counts used in different paths refer to different parents: 791,635 is the deduplicated chirality-relevant DESI match; 812,793 is the row-level T-Web environment table and 783,820 its unique-TARGETID subset; 678,945 is the $z \leq 0.24$ sphere-PIS sensitivity parent; 694,642 is the released GALZONE TARGET universe, 145,789 is its chirality-catalog intersection, and 145,766 is the focal quality parent after the catalog-native OUT= 0 cut. Exact membership in the union of released VoidFinder holes then yields 31,937 void and 113,829 non-void rows. These counts are nested or path-specific bookkeeping, not competing estimates of one sample size. Figure 1 shows the redshift distribution of the matched sample: it peaks at $z \approx 0.15$–0.2 (median 0.168) and falls off steeply above $z \approx 0.5$, with a sparse tail extending to the maximum $z = 3.83$.

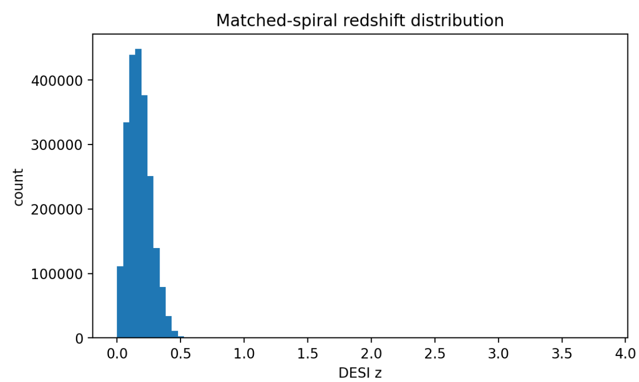

Figure 1. Redshift distribution of the matched chirality × DESI DR1 spiral sample (1″ acceptance, after dedup). The distribution peaks at $z \approx 0.15$–0.2 (median 0.168) and falls off steeply above $z \approx 0.5$; a sparse tail extends to the maximum $z = 3.83$ (Table 2).

4. T-WEB COSMIC-WEB CLASSIFICATION

4.1. *Algorithm*

We compute environment labels via the T-Web tidal-tensor classifier (Hahn *et al.* 2007 (5); Hoffman *et al.* 2012 (6); Cautun *et al.* 2014 (7)). *Nomenclature reminder*: this paper uses "T-Web" for our implementation of the Hahn 2007 tidal-tensor recipe; the associated dataset and software artifacts (e.g. the analysis driver [A3]) retain the "V-Web" name for backward compatibility with earlier releases. The Hoffman 2012 velocity-shear V-Web (which requires a separate velocity reconstruction not used here) is the conceptually distinct

Table 2. Matched chirality × DESI DR1 catalog ($1''$ acceptance). Input rows are the post-cut DESI DR1 selection (`ZWARN=0`, GALAXY/QSO, $0.01 \leq z \leq 4$).

Quantity	Value
DESI DR1 input rows (post-cut)	16,361,731
Matched primary	2,349,908
Matched primary after dedup	2,232,212
Chirality-relevant	791,635
CW	393,592
CCW	398,043
NS (Paper IV NOT_SPIRAL class; excluded)	1,440,577
SPECTYPE GALAXY	2,215,032
SPECTYPE QSO	17,180
Leg BASS+MzLS	688,608
Leg DECaLS	1,538,880
Leg DES	4,724
z median	0.168
z max	3.83
p_{50} separation	$0.0066''$
p_{99} separation	$0.30''$

classifier; external T-Web implementations (e.g. the concurrent DR1 analysis of Ref. (12)) are also covered by the T-Web label.

1. Filter DESI DR1 `zall` to `ZWARN==0`, SPECTYPE = GALAXY, $0.01 \leq z \leq 2.0$ (yields 14,622,283 galaxies).

2. Compute comoving distance $\chi(z)$ via Planck 2018 (9). Unit convention used throughout the pipeline: ASTROPY returns χ in Mpc and we multiply by h explicitly to work in h^{-1} Mpc (sanity value: $\chi(z{=}0.2) = 570.4\,h^{-1}$ Mpc), the same convention as the DESIVAST hole-catalog $X/Y/Z$ columns used in §8.[2]

3. Map to Cartesian:

$$X = \chi \cos\delta \cos\alpha,$$
$$Y = \chi \cos\delta \sin\alpha,$$
$$Z = \chi \sin\delta.$$

4. Cloud-in-Cell deposit onto a 256^3 comoving grid (full DR1 bounding box 6,634 Mpc/h at $256^3 \to$ cell 25.9 Mpc/h). The deposit operates on the row-level parent (14,622,283 survey–program coadd rows over 14,100,704 unique `TARGETID`s, §8.7), so repeat coadds (521,579 rows, 3.6% of the parent) contribute one deposit per row, mildly overweighting multiply-observed targets. A deduplicated (one-deposit-per-`TARGETID`) full field rebuild on the identical grid geometry quantifies this: in-footprint class volume fractions shift by at most 0.70 pp (wall −0.70, filament +0.68, cluster +0.20, void −0.18), 97.8% of common-mask cells and 97.9% of matched-spiral assignments retain their class, and per-class $f_{\rm CW}$ moves by at most 0.23 pp (the small wall class; filament −0.005 pp, cluster +0.013 pp), leaving every environment–chirality conclusion unchanged (artifact [A4]).

5. Build a survey-footprint mask by dilation of occupied cells (SCIPY `binary_dilation` with the default face-connected $3{\times}3{\times}3$ cross structuring element, $\lceil R_s/\text{cell}\rceil + 1 = 2$ iterations at the canonical configuration; the count is recomputed per Phase 2 sweep cell, giving 3 at $R_s = 50$): 2,417,697 occupied → 3,150,086 in-mask (18.8% of the cube); $\bar{\rho}_{\rm cell} = 4.64$ galaxies/cell.

6. Convert counts to overdensity $\delta = \rho/\bar{\rho} - 1$.

7. Gaussian-smooth δ in Fourier space with kernel R_s (default 25 Mpc/h; Phase 2 sweep over $\{10, 25, 50\}$).

8. Solve Poisson in k-space: $\Phi(k) = -\delta_k/k^2$ (with $k{=}0$ mode zeroed).

9. Tidal tensor: $T_{ij}(k) = -k_i k_j \Phi(k)$ (Fourier sign convention $\partial_i\partial_j \leftrightarrow (ik_i)(ik_j) = -k_i k_j$, so with $\Phi(k) = -\delta_k/k^2$ this gives $T_{ij}(k) = +k_i k_j \delta_k/k^2$; the committed implementation [A3] applies exactly this sign, matching the title-footnote convention — the reported volume fractions, e.g. void 24.4% / cluster 1.0%, are consistent with the standard sign); inverse-FFT the six unique components. Conventions: $k_i = 2\pi n_i/L$ with L the box side (`scipy fftfreq` scaled by 2π/cell), so k carries physical $h\,\text{Mpc}^{-1}$ units; the CIC mass-assignment window is *not* deconvolved before the second derivatives. Only the ordering and sign of the eigenvalues relative to $\lambda_{\rm th}$ enter the classification, so $\lambda_{\rm th}$ is defined on this (window-convolved) normalization.

[2] Dimensional derivation: a distance D expressed in h^{-1} Mpc has numerical value $D/(h^{-1}\,\text{Mpc}) = h\,D/(1\,\text{Mpc}) = h \cdot D[\text{Mpc}]$, so multiplying the value in Mpc by h yields the value in h^{-1} Mpc. With Planck 2018 $h = 0.6766$, $\chi(z = 0.2) \approx 843$ Mpc gives $0.6766 \times 843 = 570\,h^{-1}$ Mpc, matching the sanity anchor. The pipeline implements this as `chi = Planck18.comoving_distance(z).value; chi = chi * cosmo.h` (multiply-by-h convention; [A3], lines 106–108). The incorrect divide-by-h operation $\chi[h^{-1}\,\text{Mpc}] = \chi[\text{Mpc}]/h$ (which contradicts the dimensional relation $D/(h^{-1}\,\text{Mpc}) = h \cdot D[\text{Mpc}]$ derived above and would give the wrong value $\approx 1246\,h^{-1}$ Mpc at $z = 0.2$) is *not* a valid alternative and is not used here; the multiply-by-h convention above is what the pipeline implements.

10. At each grid cell, diagonalize the symmetric 3×3 tensor to get eigenvalues $\lambda_1 \geq \lambda_2 \geq \lambda_3$.

11. Classify by count of $\lambda > \lambda_{\rm th}$: $0 \to$ void, $1 \to$ wall, $2 \to$ filament, $3 \to$ cluster (Cautun *et al.* (7) geometric default $\lambda_{\rm th}=0$).

12. NN-interpolate the per-cell label + smoothed log-density ($\log_{10}(1+\delta_{\rm smooth})$, the quantity stored as the per-galaxy density covariate and used for all within-class density stratifications; quartile binning on it is identical to binning on the linear density because the transform is monotone) to each galaxy.

4.2. *Phase 1 volume fractions*

For the canonical configuration ($R_s = 25\,{\rm Mpc}/h, \lambda_{\rm th} = 0, N_{\rm grid} = 256^3$) the in-footprint volume fractions are {void 0.244, wall 0.413, filament 0.333, cluster 0.010}(Fig. 2). The cluster volume fraction (1.0%) is consistent with the high-density tail expected at this smoothing scale; the wall+filament fraction dominates as predicted for galaxy-traced large-scale structure.

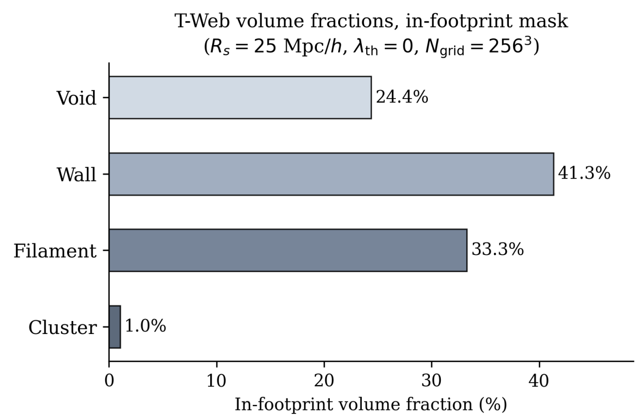

Figure 2. In-footprint T-Web volume fractions for the canonical ($R_s = 25\,{\rm Mpc}/h, \lambda_{\rm th} = 0, N_{\rm grid} = 256^3$) run on 14,622,283 DESI DR1 spectroscopic galaxies (horizontal bar chart; value labels show percentage to one decimal place). The cluster volume fraction (1.0%) reflects the high-density tail; the wall+filament fraction (74.5%) dominates as expected for galaxy-traced large-scale structure.

5. STATISTICAL METHODS

For each binned analysis we report observed CW fraction, the Jeffreys 95% binomial credible interval (Jeffreys prior Beta(1/2, 1/2)), and the signed deviation from 0.5 $\sigma_{\rm from\,half} \equiv (n_{\rm CW} - 0.5N)/(0.5\sqrt{N})$ (the standard one-sample binomial z-score against the null $p = 0.5$; we keep the explicit name to distinguish it from the monopole-referenced $\sigma_{\rm pred}$ below). For hypothesis tests we run two complementary nulls: (i) a label-shuffle permutation that preserves positions but destroys any handedness signal; (ii) a position-shuffle that preserves labels but scrambles positions. For the per-bin count statistics used in this paper the two are the same permutation null (permuting either side of the label–position assignment induces the identical null distribution of bin counts), so all quoted look-elsewhere p-values are from the label-shuffle implementation; the position-shuffle is retained as a pipeline cross-check rather than separately tabulated. Both nulls draw $N_{\rm MC} = 1000$ independent permutations from a deterministic-seeded NumPy `default_rng` (seed fixed in the pipeline config; the same config-level seed initializes each scan family's generator, so identical underlying random streams are shared across families — the distinct-stream re-draws of §6.6 confirm the quoted p-values are stream-independent within the $N_{\rm MC} = 1000$ permutation standard error); per-bin $\sigma_{\rm from\,half}$ is recomputed under each draw, and the null distribution is constructed as the empirical CDF of the per-realization statistic. Analysis drivers are available in the companion data repository (defined in Appendix C). Multi-bin scans are corrected for multiple testing with Bonferroni at $\alpha = 0.01$.

Statistics glossary. Because several $\sigma/z/p$ variants appear, Table 3 consolidates their definitions, null hypotheses and one-/two-sample nature. The focal released-parent result instead uses a covariate-standardized average marginal contrast with a cluster-sandwich interval.

Table 3. Statistics glossary for the secondary and sensitivity paths. The $\sigma_{\rm from\,half}$ and $\sigma_{\rm pred}$ columns are one-sample diagnostics; z_Δ is an unadjusted two-sample sensitivity statistic.

Statistic	Null / denom.	Type / role
$\sigma_{\rm from\,half}$	$p = 0.5$; $0.5\sqrt{N}$	1-samp.; diagnostic
$\sigma_{\rm pred}$	monopole; $0.5\sqrt{N}$	1-samp.; monopole flag
$\sigma_{\rm vs\,monopole}$	$p_0 = f^{\rm P5}$; $0.5\sqrt{N}$	1-samp.; residual
z_Δ	$\Delta f_{\rm CW} = 0$; 2-samp. SE	2-samp.; contrast
empirical p	label-shuffle CDF	perm. LEE

We explicitly compare each $\sigma_{\rm from\,half}$ against the classifier-monopole offset (independently verified as the P5 internal matched-sample monopole $f_{\rm CW}^{\rm P5} = 0.49719$, Table 20; Paper IV provides a corroborating external estimate (3))

$$\sigma_{\rm pred} = \frac{\Delta f_{\rm CW}}{0.5/\sqrt{N}} = 2\cdot\Delta f_{\rm CW}\cdot\sqrt{N}, \tag{1}$$

with $\Delta f_{\rm CW} = -0.0026$ (the monopole offset expressed as a fractional deviation from 0.5, i.e. $\Delta f_{\rm CW} \equiv \bar{f}_{\rm CW} - 0.5$) to flag whether a deviation is attributable to the global bias rather than environment-correlated chirality. Where a residual is computed against the same-sample non-half reference $p_0 = f_{\rm CW}^{\rm P5} = 0.4972$, p_0 is estimated rather than independent. The pooled class-versus-rest covariance is therefore required; the corrected filament and cluster residuals are approximately $+1.40$ and -1.56, respectively, and do not alter the omnibus null conclusion. The exact $\sqrt{p_0(1-p_0)/N}$ single-bin denominator differs from $0.5/\sqrt{N}$ by a factor $\sqrt{4p_0(1-p_0)} = 0.99998$, but that near-equality does not remove the shared-reference covariance. The monopole reference itself carries finite counting uncertainty, which we propagate explicitly: where $\sigma_{\rm pred}$ uses the Paper IV catalog-wide $\Delta f_{\rm CW}$ ($N = 3.2 \times 10^6$, se $\approx \sqrt{0.25/(3.2 \times 10^6)} = 2.8 \times 10^{-4}$), the induced uncertainty on $\sigma_{\rm pred}$ for an $N \approx 4 \times 10^5$ class is $2\,{\rm se}\sqrt{N} \approx 0.36$; where the matched-sample monopole $f_{\rm CW}^{\rm P5}$ is the reference ($N = 812{,}793$, se $\approx 5.5 \times 10^{-4}$), it is ≈ 0.7 for the same $N \approx 4 \times 10^5$ class. Residuals of order 1–2σ (e.g. the Phase-2 resolved-cell maximum 1.64) should be read with this band in mind; the label-shuffle permutation null, which fixes the total CW count at its observed value, is conditional on the observed matched-sample CW count — i.e. every permutation test in this paper treats the global CW fraction as fixed at its observed value rather than propagating its uncertainty; uncertainty in the Paper IV classifier monopole is propagated separately in the analytic $\sigma_{\rm from\,half}$ comparisons, which are displayed only through those analytic values — and no conclusion in this paper depends on a residual threshold finer than this band. Because $\sigma_{\rm from\,half}$ grows as $\sqrt{N}$ at fixed fractional offset, raw σ values are not comparable across bins of different N; only the monopole-subtracted residuals are. The formal version of this comparison is the per-class one-sample residual test against $f_{\rm CW}^{\rm P5}$ reported in Table 20 (all $|\sigma_{\rm vs\,monopole}| < 1.15$) together with the omnibus 4×2 homogeneity test of §6.2; deviations beyond $|\sigma_{\rm obs} - \sigma_{\rm pred}| > 3$ would be candidate environmental signals.

5.1. *Look-elsewhere (LEE) correction*

For multi-bin scans (HEALPix per-pixel deviations, redshift quintiles, density quintiles), we report two complementary LEE corrections.

Parametric Bonferroni: for K independent bins controlled at the two-sided family-wise level α (per-bin level α/K), the threshold on the maximum-absolute-σ statistic is

$$|\sigma|_{\alpha,K}^{\rm Bonf} \;=\; \sqrt{2}\,{\rm erfc}^{-1}\!\left(\frac{\alpha}{K}\right), \qquad (2)$$

where the α/K argument reflects the *two-sided* per-bin significance (each tail contributes $\alpha/2K$, so $|\sigma|$ thresholds apply symmetrically to both positive and negative deviations). This is conservative when the bin-level statistics are not independent (e.g. HEALPix per-pixel deviations correlated by the mask boundary). For $K = 5$ density quintiles at $\alpha = 0.01$, Eq. (2) gives $|\sigma|_{0.01,5}^{\rm Bonf} \approx 3.09$ (two-sided); for $K = 1054$ NSIDE-16 HEALPix pixels at $\alpha = 0.05$, $|\sigma|_{0.05,1054}^{\rm Bonf} \approx 4.07$ (two-sided). For the historical five-variant DESIVAST scan at $\alpha = 0.05$, the threshold is $|\sigma|_{0.05,5}^{\rm Bonf} \approx 2.58$ (two-sided); for the Bonferroni-9 secondary sweep at $\alpha = 0.05$, the threshold is $|\sigma|_{0.05,9}^{\rm Bonf} \approx 2.77$ (two-sided). All quoted thresholds apply per-bin symmetrically to both CW-excess and CW-deficit deviations.

Empirical max-stat MC null: for each scan we run $N_{\rm MC}$ label-shuffle permutations preserving sample size; for each realization we record the maximum absolute $\sigma_{\rm from\,half}$ across the K bins. The empirical p-value is

$$p_{\rm LEE} \;=\; \frac{1 + \#\{k : |\sigma|_{\rm max}^{(k)} \geq |\sigma|_{\rm max}^{\rm obs}\}}{1 + N_{\rm MC}}, \qquad (3)$$

which preserves any sample-correlation structure that Eq. (2) ignores. We use the empirical max-stat null for the secondary scans and report the parametric Bonferroni threshold as a cross-check. The raw parity-null cluster-redshift Z3 value (-3.14σ) crosses its Bonferroni-4 $\alpha = 0.05$ threshold, whereas the monopole-subtracted Z3 residual (-1.50σ) and the empirical max-stat scan remain null (Sec. 6.5); we do not conflate those different null hypotheses. All $N_{\rm MC} = 1{,}000$ permutation p-values in this paper carry a Monte-Carlo standard error ${\rm se}_{\rm MC} = \sqrt{p(1-p)/N_{\rm MC}}$, i.e. ≈ 0.010 at $p \approx 0.13$ and ≈ 0.015 at $p \approx 0.5$; quoted second/third decimals should be read against this resolution.

5.2. *Focal vs. secondary analysis paths (pre-registration caveat)*

No timestamped analysis plan predates inspection of these data. After venue review, we changed the narrative hierarchy to prefer a released, catalog-native parent over the earlier author-constructed any-hole geometry. This change is post-review and post-hoc; it improves estimand clarity but does not make the analysis confirmatory.

Table 4 places the focal released-parent estimate beside the two demoted author-defined any-hole estimates, so the consequence of this hierarchy change can be read in one place instead of being assembled from Tables 7, 14, 17, and 18. Every interval in that comparison contains zero, and the demoted unrestricted any-hole path carries the larger p_Δ (0.76) of the two, against the focal $p_\Delta = 0.66085$.

The focal released-parent descriptive estimate uses the released DESIVAST GALZONE TARGET universe, retains `OUT`$= 0$ as its quality parent, assigns the

Table 4. Estimator-hierarchy sensitivity: the focal released-parent estimate beside the two demoted author-defined any-hole estimates. "Demoted" marks a path retained in full as a sensitivity rather than as the focal estimate; demotion is not deletion, and each demoted path is reported in its own section and table as cited. Every entry is transcribed from the source cited in its last column and is reproduced at that source's stated precision; nothing in this table is recomputed. Sign convention $\Delta f_{\rm CW} \equiv f_{\rm CW}^{\text{non-void}} - f_{\rm CW}^{\text{void}}$ (fractional units). The three paths use different parents and control volumes on overlapping samples; they are correlated variants shown for transparency and are not pooled into a joint constraint. All three are nominal non-detections whose 95% intervals contain zero. The focal path is not the most null-favorable of the three: the demoted unrestricted any-hole path carries the larger p_Δ (0.76, against the focal 0.66085), so the post-review hierarchy change did not move the reported result toward the largest available p-value.

Estimator path	Status	$\Delta f_{\rm CW}$	SE(Δ)	95% CI	p_Δ and source
Released-parent DESIVAST GALZONE `OUT`= 0; exact hole-union void arm; 13-column linear-nuisance adjusted, NSIDE= 4 CR1 ($N = 145{,}766$)	Focal	+0.00145442	0.00331502	$[-0.00504290, +0.00795174]$	0.66085 (wild-cluster 0.67345); Table 7, [A41–A44]
Author-defined any-hole, footprint-restricted control; exact (k-unbounded) membership, unadjusted two-sample binomial ($n_{\rm void} = 57{,}081$)	Demoted	+0.0018	0.0023	$[-0.0027, +0.0064]$	0.43; §8.2, Table 14, [A15]
Author-defined any-hole, unrestricted control; sphere-PIS $k = 20$ membership, unadjusted two-sample binomial ($n_{\rm void} = 56{,}981$)	Demoted	+0.00067	0.00219	$[-0.0036, +0.0050]$	0.76; §8.2, Tables 17 and 18, [A10]

void arm by exact VoidFinder hole-union membership, and applies covariate standardization on $N = 145{,}766$ rows. Its focal 13-column linear-nuisance non-void-minus-void average marginal contrast is $+0.00145442$, with coarse HEALPix NSIDE= 4 cluster-sandwich SE = 0.00331502, 95% CI $[-0.00504290, +0.00795174]$, and normal $p = 0.66085$; the null-imposed 99,999-draw wild-cluster efficient-score test gives $p = 0.67345$. This is the headline exploratory observational result, not a confirmatory analysis.

The VoidFinder any-hole/sphere-PIS analyses, the other DESIVAST membership variants, T-Web, Tempel, ASTRA, and the concurrent-literature overlay are sensitivities or secondary diagnostics. Their multiplicity and method dependence are disclosed, but they are not pooled into a family-wide constraint. In particular, a null in this exploratory tree does not establish environment-independence or an exclusion limit.

Whole-tree family-wise significance. The look-elsewhere corrections above operate *within* each scan family: every Phase 2 cell is corrected within its own $K = 4$ class family (Table 13), and a global max-statistic correction is reported across the nine Phase 2 cells ($p_{\rm global} = 0.36$, or 0.27 over the six resolved cells). For completeness we also state a single family-wise-corrected significance for the most extreme deviation *anywhere* in the declared analysis tree of Table 5. Referenced against its own null, that largest deviation is the bright-vs-dark tracer-program filament sign-flip of §6.2, a two-sample contrast at $|z| \approx 2.1$ (row-level; $|z| = 1.95$ on the de-duplicated unique-`TARGETID` sample), with per-test two-sided $p_{\min} = 0.036$. We do *not* treat the larger raw $|\sigma_{\text{from half}}|$ excursions (the bright-program -5.28, the no-void-coverage sky region -4.75) as candidate signals: those measure the single catalog-wide classifier monopole $f_{\rm CW}^{\rm P5} = 0.49719$ against $p = 0.5$, which is not the environmental null this paper tests; monopole-subtracted, the same regions return residuals $|\sigma_{\rm obs} - \sigma_{\rm pred}| \le 1.55$. A conservative Bonferroni bound over the $N = 23$ paths enumerated in Table 5, $p_{\rm global} \le \min(1,\, N\, p_{\min}) = 0.82$, leaves that most extreme deviation non-significant; because 23 is the smallest defensible whole-tree trials count, any finer per-bin enumeration only raises $p_{\rm global}$ further from significance (e.g. the narrative few-dozen budget saturates the bound at 1). No test in the tree survives whole-tree multiplicity correction, and no reported number or claim changes: the whole-tree result is a non-detection ([A45], [A46]).

Analysis-tree declaration. Table 5 enumerates the full analysis tree tested in this paper, distinguishing the focal released-parent estimate from the nine secondary Bonferroni tests in the Phase 2 sensitivity sweep and from descriptive stratifications that carry no additional look-elsewhere correction. All tests outside the focal estimate are *descriptive consistency checks*; a finding at $|\sigma| \sim 2$–3 in a secondary path should be interpreted against its own per-test threshold, not as a confirmatory gate.

6. RESULTS

6.1. *Focal hybrid released-parent descriptive estimate*

The focal estimand is $f_{\rm CW}(\text{non-void}) - f_{\rm CW}(\text{void})$ within a three-layer released-parent construction. The released DESIVAST GALZONE `TARGET` universe defines which public targets are eligible; `OUT`= 0 defines the

Table 5. Analysis-tree declaration after the post-review hierarchy change. One released-parent estimator is listed as the focal descriptive estimate; every other path is a sensitivity or secondary diagnostic. The listed thresholds describe the historical scans and do not turn this post-hoc analysis into a confirmatory family. Table 4 gives the focal estimate side by side with the two demoted any-hole estimates.

Path	Tests	K	Status
Focal exploratory/descriptive estimate			
Released GALZONE TARGET parent	adjusted `OUT`$=0$ hole-union contrast	1	focal
DESIVAST sensitivity variants			
DESIVAST VoidFinder	any-hole void vs non-void f_{CW}	1	sensitivity
DESIVAST V2-REVOLVER	sphere-PIS void vs non-void f_{CW}	1	sensitivity
DESIVAST V2-VIDE	sphere-PIS void vs non-void f_{CW}	1	sensitivity
V2-REVOLVER catalog-native	GALZONE void vs non-void f_{CW}	1	sensitivity
V2-VIDE catalog-native	GALZONE void vs non-void f_{CW}	1	sensitivity
Secondary sweep (Bonferroni-9; $\alpha = 0.05$, threshold $\lvert\sigma\rvert = 2.77$)			
Phase 2 cell ($R_s = 10, \lambda = 0.0$)	max-class residual	1	secondary
Phase 2 cell ($R_s = 10, \lambda = 0.1$)	max-class residual	1	secondary
Phase 2 cell ($R_s = 10, \lambda = 0.3$)	max-class residual	1	secondary
Phase 2 cell ($R_s = 25, \lambda = 0.0$)	max-class residual	1	secondary
Phase 2 cell ($R_s = 25, \lambda = 0.1$)	max-class residual	1	secondary
Phase 2 cell ($R_s = 25, \lambda = 0.3$)	max-class residual	1	secondary
Phase 2 cell ($R_s = 50, \lambda = 0.0$)	max-class residual	1	secondary
Phase 2 cell ($R_s = 50, \lambda = 0.1$)	max-class residual	1	secondary
Phase 2 cell ($R_s = 50, \lambda = 0.3$)	max-class residual	1	secondary
Descriptive (no additional look-elsewhere correction)			
T-Web 4-class omnibus	4×2 homogeneity χ^2	—	descriptive
Redshift scan	label-shuffle p vs z	—	descriptive
Density quintiles	bright-fraction residuals	—	descriptive
HEALPix (NSIDE $= 16, 32, 64$)	sky-position scan	—	descriptive
Tracer-program split	bright vs dark f_{CW}	—	descriptive
Tempel FoF overlap	filament concordance	—	descriptive
ASTRA EDR per-object	supporting diagnostic consistency check (EDR overlap-size caveat)	—	descriptive
T-Web concurrent-lit	volume-fraction comparison	—	descriptive

catalog-native quality parent; and exact point-in-sphere membership in the *union of the released VoidFinder holes* defines the void arm. It is not a V2 GALZONE void-membership estimand. Table 6 gives the complete accounting before any secondary path is considered.

Table 6. Exact focal sample and estimand flow. The first two rows define the released target universe and join; `OUT`$=0$ defines the quality parent; exact VoidFinder hole-union membership partitions that same parent into the two estimand arms.

Stage	Rows
Released GALZONE `TARGET` universe	694,642
Joined to frozen Paper IV chirality parent	145,789
Quality parent: `OUT`$=0$	145,766
VoidFinder hole-union member	31,937
Non-member (non-void arm)	113,829

For $Y_i = 1$ denoting a CW classifier label and $V_i = 1$ denoting hole-union membership, artifacts [A41–A44] fit the focal unpenalized logistic model

$$\begin{aligned}\operatorname{logit}\Pr(Y_i = 1) = \beta_0 + \beta_V V_i + \beta_z z_i + \beta_r r_i \\ + \beta_R \log R_i + \beta_q q_i + \beta_E E_i \\ + \alpha_{P(i)} + \gamma_{M(i)} + \beta_e e_i,\end{aligned} \tag{4}$$

where q_i is classifier confidence, E_i is Galactic extinction, $P(i)$ is `PHOTSYS`, $M(i)$ is morphology, and e_i is the GALZONE edge flag. The fitted design has 13 columns and full rank. Sky position enters the covariance rather than the mean model: the focal CR1 calculation clusters by occupied NSIDE$=4$ block, and [A43–A44] repeat the identical mean model at NSIDE$=2, 4, 8$ and with 3-D nearest-MAXIMALS clusters. The older A37 spline/sky-fixed-effect model is retained only as the flexible sensitivity in Table 7.

For cluster g, let $U_g = \sum_{i\in g} x_i(Y_i - \widehat{p}_i)$. The explicit finite-sample one-way cluster sandwich uses $c_{G,N,K} = [G/(G-1)][(N-1)/(N-K)]$:

$$\begin{aligned}\widehat{\operatorname{Var}}(\widehat{\beta}) = c_{G,N,K}(X^{\mathsf{T}}WX)^{+} \\ \times\left(\sum_{g=1}^{G} U_g U_g^{\mathsf{T}}\right)(X^{\mathsf{T}}WX)^{+},\end{aligned} \tag{5}$$

The reported coefficient covariance is this complete finite-sample-corrected sandwich (bread, cluster-score meat, and bread); the reported contrast SE is the square root of the delta-method propagation of that full covariance, not the finite-sample factor or a model-based SE alone. Table 7 freezes the A41–A42 focal model and inference metadata, with the like-for-like clustering and interaction closures in [A43–A44], and separately identifies the older A37 flexible-model sensitivity. A42's original statement that the 13-column fit "does not replace" the 78-column estimate is superseded by A44: the full-rank 13-column specification is focal, whereas the 78-column fit is a rank-fragile sensitivity.

The 13-column specification is focal because it preserves the same hybrid sample, exposure, outcome, measured covariates, and NSIDE$=4$ cluster unit while permitting both CR1 and null-imposed wild-cluster inference without having more fitted columns than clusters. It was declared after review and inspection of the data and is therefore exploratory, not preregistered. The older spline/fixed-effect specification has $K=78$ fitted columns but only $G=50$ coarse sky clusters; its ordinary CR1 normal approximation is rank-fragile even though the scalar calculation is reproducible. It is retained only as a flexible-model sensitivity, not as the headline interval.

The focal standardized non-void-minus-void contrast is $\Delta f_{\rm CW}=+0.00145442$. Its coarse-sky CR1 95% interval is $[-0.00504290, +0.00795174]$, and the wild-cluster score $p=0.67345$. This focal estimate is consistent with zero and is explicitly descriptive/exploratory: the hierarchy was chosen after review and after inspecting the data. It is not an exclusion, a physical-handedness measurement, or evidence for environment independence. The identical $K=13$ estimate remains consistent with zero at NSIDE$=2,4,8$ and under nearest-MAXIMALS 3-D clustering (Table 7; [A43–A44]). Detailed construction and sensitivity results follow in Section 8.

6.2. *Secondary T-Web diagnostic*

Role of this section. The T-Web tidal-tensor path is a *diagnostic stress test, not load-bearing*: the focal released-parent DESIVAST contrast is reported first in §6.1, and the T-Web material below is secondary (§5.2). It is reported as a secondary consistency check whose low-z void bin is survey-shell contaminated (§9.3) and should not be read as an independent replication. Its Jeffreys intervals and contingency statistics condition on the observed rows; they do not include cosmic variance or spatial covariance.

Table 8 reports CW fraction by cosmic-web class on the 812,793 env-labeled spiral rows produced by joining the 791,635 chirality-relevant matched spirals to the secondary T-Web environment table (the join carries 783,820 unique env-matched spirals, counted once per repeat DR1 survey–program coadd row; §8.7 documents the reconciliation — the superset and unique-spiral monopoles agree to four decimals, so the headline is invariant under either parent). An omnibus 4×2 homogeneity test (CW/CCW $\times$ class) on the table counts returns $\chi^2=3.55$ with 3 d.o.f. ($p=0.31$): the four classes are statistically consistent with a single common CW fraction (the $4{\times}2$ integer contingency table is tabulated in Appendix B, Table 24, for independent recomputation). Because the row-level parent repeats 3.56% of `TARGETID`s across program coadds (28,973 duplicate rows in 812,793 env-labeled rows; technically violating the independence assumption of the contingency test), we recompute the same test on the 783,820-row unique-spiral subset (one row per `TARGETID`): $\chi^2=3.00$, $p=0.39$ ($\chi^2=2.92$, $p=0.41$ further excluding the 79 `TARGETID`s with conflicting duplicate env labels), so the duplicates have negligible impact on the null verdict ([A5]). The label-shuffle look-elsewhere p on the max-class $|\sigma_{\rm from\ half}|$ statistic is likewise null and remains similar to stratification of the shuffle by imaging leg and DESI program ($p=0.12$ free vs 0.12 stratified; [A6]).

The small T-Web void count ($n=428$), versus more than 56,000 galaxies in the later DESIVAST void sensitivity, is artificially depressed by the T-Web survey-shell and selection-field construction; the randoms-weighted diagnosis and the like-for-like DESIVAST comparison are given in §8.2 and §12.

Figure 3 visualizes the per-class CW fractions with 95% Jeffreys binomial credible intervals; all four classes bracket the Paper IV global $\bar{f}_{\rm CW}=0.4974$ horizontal reference, and the void 95% CI brackets parity $f_{\rm CW}=0.5$. The range across the four classes is 1.98 percentage points, set by the counting noise of the low-n void bin (0.484) against the catalog-monopole-dominated high-n filament and cluster bins (~ 0.497).

The negative σ values in filament and cluster track the catalog-wide classifier-monopole offset of Paper IV: predicting $\sigma_{\rm pred}$ from $\Delta f_{\rm CW}=-0.0026$ gives $\sigma_{\rm pred}$(filament)≈ -3.32 and $\sigma_{\rm pred}$(cluster)≈ -3.28, leaving monopole-subtracted residuals of $+0.71\sigma$ (filament) and -1.38σ (cluster). Neither residual is negligible at face value, but both are bounded by the propagated monopole-reference uncertainty ($\approx 0.7\sigma$ for an $n\sim 4\times 10^5$ class, §5) and, on the calibrated $f_{\rm CW}^{\rm P5}$ basis, collapse to $|\sigma_{\rm vs\ monopole}|<1.15$ (Table 20). We therefore interpret these as the global monopole leaking through the larger-sample bins, not as environment-dependent chirality.

Table 7. Model and covariance contract for the focal descriptive estimate and flexible sensitivity. The focal 13-column specification is paired with CR1 and null-imposed wild-cluster inference. The older 78-column spline/fixed-effect fit is retained as a rank-fragile flexible-model sensitivity.

Component	Frozen specification
Focal fit [A41–A42]	Unpenalized Newton–Cholesky logistic MLE with declared post-review linear nuisance basis: void indicator, linear redshift, magnitude, log-size, confidence, extinction, `PHOTSYS`, morphology, and GALZONE edge; $N = 145{,}766$, $K = 13$, design rank 13
Focal inference	$G = 50$ occupied NSIDE= 4 clusters; CR1 $\Delta f_{\rm CW} = +0.00145442$, SE $= 0.00331502$, 95% CI $[-0.00504290, +0.00795174]$, normal $p = 0.66085$; null-imposed 99,999-draw Rademacher wild-cluster efficient-score $p = 0.67345$ (seed 20260715)
Focal clustering robustness [A43–A44]	Identical $N = 145{,}766$, $K = 13$ fit and contrast: NSIDE= 2, 95% CI $[-0.00621591, +0.00912475]$; NSIDE= 4, $[-0.00504290, +0.00795174]$; NSIDE= 8, $[-0.00496400, +0.00787285]$; and 3,750 nearest VoidFinder-MAXIMALS 3-D clusters, $[-0.00475998, +0.00766882]$. The point estimate is $+0.00145442$ throughout; all intervals include zero.
Flexible sensitivity [A37]	78-column spline/fixed-effect model with Moore–Penrose bread inverse, $G = 50$ NSIDE= 4 clusters: $\Delta f_{\rm CW} = +0.00125636$, SE $= 0.00341274$, 95% CI $[-0.00543249, +0.00794522]$, normal $p = 0.71277$; rank-fragile because $K = 78 > G = 50$
Flexible-fit scale sensitivity	3,750 nearest-VoidFinder-MAXIMALS clusters on the same 78-column fit and contrast; SE $= 0.003174$, $p = 0.692$

Table 8. CW fraction per cosmic-web environment, secondary T-Web diagnostic ($R_s = 25\,{\rm Mpc}/h, \lambda_{\rm th} = 0$), on the 812,793-row env-labeled parent. $\sigma_{\rm from\,half}$ scales as $\sqrt{n}$ at fixed offset and is not comparable across rows of different n (§5).

Env	n	$n_{\rm CW}$	$f_{\rm CW}$	$\sigma_{\rm from\,half}$
void	428	207	0.4836	−0.68
wall	6,673	3,359	0.5034	+0.55
filament	408,187	203,261	0.4980	−2.61
cluster	397,505	197,284	0.4963	−4.66
range	—	—	**0.0198**	—

Void-bin smallness. The void bin has only $n = 428$ galaxies. Two distinct void volume fractions appear in this paper and refer to different denominators: (i) the T-Web tidal-classifier void class occupies ≈24.4% of in-footprint cell volume (§4.1, [A7]), while (ii) only ≈0.1% of in-footprint grid cells fall inside a DESIVAST VoidFinder sphere (the point-in-sphere membership criterion on the 25.9 Mpc/h grid used for the sky-stratification analysis of §8.6). The full T-Web void parent already contains only $n = 428$ galaxies; applying the separate $z \leq 0.24$ cut leaves six and is not the cause of the quoted 428-object count. The small full-parent count instead reflects the sparse $r \leq 17.8$ DESI Legacy spiral selection within T-Web void cells. The $\sigma = -0.68$ on the void class is statistical noise at this N; the 95% Jeffreys credible interval is $f_{\rm CW}^{\rm void} \in [0.435, 0.530]$, which brackets parity.

6.3. *Redshift dependence*

The matched chirality-relevant subsample has redshift median 0.168 and maximum 3.83. The label-shuffle permutation null on the max-absolute-deviation-from-half statistic (the single most-deviant redshift bin, finely binned) over 1,000 shuffles returns $p = 0.372$; the complementary five-quintile look-elsewhere test (distinct statistic, coarser binning) is reported separately below ($p = 0.80$). A logistic regression of the CW indicator on $\{z, |\sin\delta|, \cos\alpha, \text{confidence}\}$ gives a z-coefficient (per unit redshift, in log-odds) of 0.0095 ± 0.0229 (z-score 0.41, $p = 0.68$) with an intercept of 0.0028 ± 0.0097 ($p = 0.77$) — both consistent with zero, i.e. no redshift dependence. A label-shuffle permutation stratified by imaging leg and DESI program (the conservative null given the per-leg/per-program residuals of §11) leaves the redshift-quintile look-elsewhere p (the coarser five-bin statistic, distinct from the finely-binned max-deviation $p = 0.372$ above) unchanged ($p = 0.81$ stratified vs 0.80 free-shuffle).

Physical-covariate robustness.—Extending the regression with galaxy physical covariates from the Galaxy Zoo DESI morphology catalog (15) (joined on `dr8_id`, 100% coverage of the declared parent: Petrosian half-light radius, r-band apparent magnitude, featured fraction, merger fraction, and — on the 152,455-galaxy featured subsample where the decision tree reaches the question — edge-on fraction) leaves the classifier-label non-detection unchanged: the joint 3-dof environment Wald test gives $p = 0.46$ (0.41 without covariates) on the canonical labels and $p = 0.99$ on the

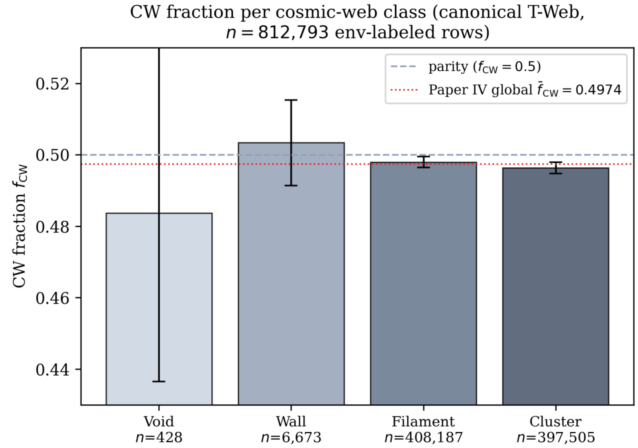

Figure 3. CW fraction per cosmic-web class in the secondary T-Web run, on the $n = 812{,}793$ env-labeled spiral rows (covering 783,820 of the 791,635 unique chirality-relevant matched spirals; 7,815 lack an environment row, §6.2). Bars show the raw observed $f_{\rm CW}$ per class (counts shown; monopole subtraction enters the $\sigma_{\rm vs\,monopole}$ column only); black error bars are 95% Jeffreys binomial credible intervals, drawn on the row-level parent — the 3.56% duplicate rows (28,973 of 812,793 env-labeled rows) violate strict i.i.d., but the worst-case design-effect inflation of the interval widths is $\sqrt{812{,}793/783{,}820} = 1.018$, i.e. $\leq 1.9\%$, and the homogeneity χ^2 is recomputed on the unique-spiral subset in §6.2. The T-Web void bin ($n = 428$) is *not load-bearing*: it is dominated by counting noise and by the survey-shell selection artifact (§9.3), has negligible overlap with the focal released-parent sample, and is retained only as a secondary diagnostic — it carries no weight in the focal contrast. The dashed horizontal line is parity ($f_{\rm CW} = 0.5$); the dotted red line is the Paper IV global $\bar{f}_{\rm CW} = 0.4974$ classifier-monopole offset. All four classes bracket the Paper IV monopole, consistent with no environmental dependence beyond the catalog-wide classifier bias.

z-shell-corrected labels. The regression parent is the 783,741 unique env-matched spirals, one row per galaxy (the 783,820 env-matched spirals of §8.7 minus the 79 `TARGETID`s whose repeat coadd rows carry conflicting environment classes); the headline covariate-extended model uses the four covariates with full coverage (radius, magnitude, featured fraction, merger fraction) and retains all 783,741 rows (100% covariate-complete for that model). The edge-on fraction, which is defined only on the 152,455-galaxy featured subsample, enters a separate featured-subsample sub-model (also null) rather than the full-parent model, so it does not violate the full-model completeness statement. The env-only Wald $p = 0.41$ is therefore not expected to coincide with the Pearson omnibus $p = 0.31$ of §6.2: the omnibus χ^2 is computed on the 812,793-row env-labeled superset, while the Wald test is a different statistic on the smaller unique-galaxy parent — both are null. Every individual environment coefficient is null after adjustment (largest: void -0.081 ± 0.107), with a maximum adjustment-induced coefficient shift of 0.17σ. No physical covariate is predictive of chirality; the only marginally predictive regressor is classifier confidence ($p \approx 0.02$), a classifier property rather than an environmental one. Artifact: [A8]. Figure 4 shows the binned equivariant CW fraction across the matched sample's redshift range.

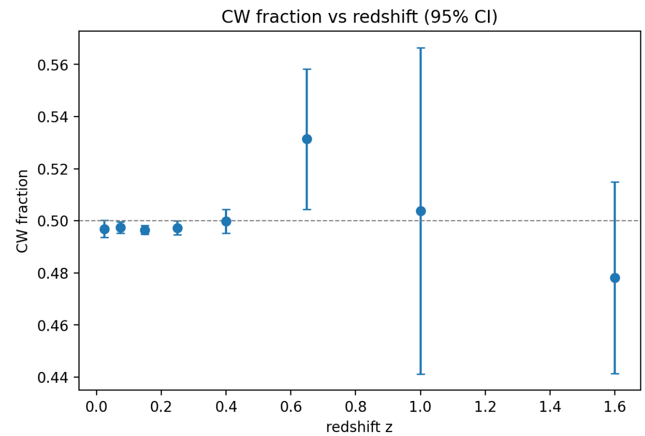

Figure 4. Equivariant CW fraction versus redshift across the matched DR1 chirality-relevant sample, with 95% binomial confidence intervals per bin. The low-z bins that dominate the sample (median $z = 0.168$) sit on the 0.5 line; bins above $z \approx 0.5$ contain few objects and have correspondingly wide intervals. The binned values are consistent with no redshift dependence, in agreement with the label-shuffle permutation test ($p = 0.372$) and the logistic regression in the text.

6.4. *Projected density dependence*

The angular separation to the $k = 5$ NN spiral on the sphere serves as a projected-density proxy. Binned in density quintiles, the maximum absolute deviation is $|\sigma|_{\rm max} = 3.94$, within the Paper IV monopole prediction from Eq. (1): at $N = 158{,}327$ per quintile the predicted $|\sigma_{\rm pred}| = 2 \cdot |-0.0026| \cdot \sqrt{158{,}327} \approx 2.07$, so the residual deviation beyond the monopole is $|\sigma_{\rm obs} - \sigma_{\rm pred}| \approx 1.87$, below the Bonferroni-5 $|\sigma|^{\rm Bonf}_{0.01,5} = 3.09$ threshold. Figure 5 shows the observed quintile values side-by-side with the Paper IV-monopole prediction; the bars track the prediction within counting statistics in all five quintiles.

Because the $k = 5$ NN proxy above is computed among the chirality-relevant spirals themselves, it is mildly endogenous (the tracer set is the test set). As a cross-check we recomputed the proxy exogenously as the angular distance to the 5th-nearest galaxy among *all* 2,232,212 deduplicated matched primaries (any chirality class) and re-binned the spirals into quintiles of that parent-tracer proxy: the maximum per-quintile deviation is $|\sigma|_{\max} = 3.64$ with a maximum monopole-subtracted residual of $|\sigma_{\rm obs} - \sigma_{\rm pred}| = 1.57$, again below the Bonferroni-5 threshold — the density null is not an artifact of the endogenous tracer choice ([A6]). A mask-edge buffer test gives the same answer: excluding the 74,070 spirals in HEALPix NSIDE-64 footprint-edge pixels ($\sim$0.9° angular buffer) and recomputing both the proxy and the quintile edges on the retained sample leaves 91.0% of retained spirals in their original quintile and shifts no per-quintile $f_{\rm CW}$ of Figure 5 by more than 0.12 pp — the quintile assignment is invariant to mask-edge effects ([A9]).

Table 9. Per-quintile $|\sigma_{\rm obs} - \sigma_{\rm pred}|$ residual table. $\sigma_{\rm obs}$ is the binomial σ-from-half on the observed CW fraction in each quintile; $\sigma_{\rm pred} = 2\Delta f_{\rm CW}\sqrt{N}$ [Eq. (1)] at $\Delta f_{\rm CW} = -0.0026$ (Paper IV-monopole prediction). All five residuals lie below the Bonferroni-5 threshold $|\sigma|^{\rm Bonf}_{0.01,5} = 3.09$, so no quintile shows a statistically-significant departure from the monopole-only model.

Quintile	$f_{\rm CW}$	$\sigma_{\rm obs}$	$\sigma_{\rm pred}$	$\lvert\sigma_{\rm obs} - \sigma_{\rm pred}\rvert$
1 (lowest)	0.4976	−1.94	−2.07	0.13
2	0.4987	−1.06	−2.07	1.01
3	0.4950	−3.94	−2.07	1.87
4	0.4961	−3.08	−2.07	1.01
5 (highest)	0.4985	−1.16	−2.07	0.91

6.5. *Within-class density-stratified cluster + filament follow-up*

The catalog-wide-monopole-projected cluster-class deviation of -4.7σ at $n_{\rm cluster} = 397{,}505$ (Section 6.2) is the strongest single-class diagnostic in the secondary T-Web table. To check whether this is a genuinely density-dependent effect within the cluster class or a boundary-misclassification artifact at the low-density edge of the T-Web cluster label, we stratify the cluster (and filament for comparison) class into four equal-population density quartiles using the T-Web per-galaxy density field.

The cluster signal is *not* monotonically increasing in density. The most-typical-cluster-density quartile Q3 ($\bar{\rho} = 2.01$, $n = 99{,}526$) returns $\sigma = -0.37$, statistically null after Bonferroni-4 correction. The strongest cluster sub-deviations are Q1+Q2 at $\bar{\rho} \approx 1.55$–1.80 (the low-density edge of the cluster class, where the T-Web $\lambda_{\rm th} = 0$ default class boundary against filament is most uncertain), while the densest quartile Q4 returns intermediate $\sigma = -2.46$. Treating the four cluster quartiles as a simultaneous family, the monopole-subtracted residuals $\sigma_{\rm obs} - \sigma_{\rm pred}$ at $\sigma_{\rm pred} = 2\,(-0.0026)\sqrt{n} \approx -1.64$ are -1.43 (Q1), -1.78 (Q2), $+1.27$ (Q3), and -0.82 (Q4) — all four below the Bonferroni-4 $\alpha = 0.05$ threshold of 2.50, so no quartile shows a significant departure from the monopole-only model after multiplicity correction. The catalog-wide-monopole-projected -4.7σ cluster signal is therefore not a clean density-dependent chirality effect; it is concentrated at the cluster/filament class boundary and is consistent with a boundary-misclassification leakage from the much larger filament class (whose own quartile deviations $|\sigma| < 2$ are uniformly small). The class boundary is verifiable quantitatively from the table: cluster Q1 ($\bar{\rho} = 1.55$) is *less dense* than filament Q4 ($\bar{\rho} = 1.86$), so the densest filament galaxies are in fact denser than the least-dense cluster galaxies – the two classes overlap in $\bar{\rho}$ at the $\lambda_{\rm th} = 0$ boundary by construction. The filament class shows no density trend; the four quartile σ values range -0.63–-1.97, all individually below the Bonferroni-4 $|\sigma| = 2.50$ threshold at $\alpha = 0.05$.

Table 10. Within-class density-stratified $f_{\rm CW}$ for the T-Web cluster and filament classes (matched-spiral $n_{\rm cluster} = 397{,}505$, $n_{\rm filament} = 408{,}187$). Quartiles binned by the T-Web per-galaxy *log*-density covariate of §4.1 step 12; $\bar{\rho}$ is the quartile mean of $\log_{10}(1+\delta_{\rm smooth})$ (Gaussian-smoothed overdensity in units of the cube-mean cell density, NN-interpolated to each galaxy position; dimensionless; $\log_{10}$ scale — the displayed values 0.90–2.21 are $\log_{10}$ quantities, e.g. cluster Q4 $\bar{\rho} = 2.21$ corresponds to $1+\delta \approx 162\times$ the cube-mean cell density). Quartile membership is identical under the linear density (monotone transform); definition verified by exact recompute in [A5]. The $\sigma_{\rm from\ half}$ values scale as $\sqrt{n}$ at fixed offset and are not comparable across rows of different n; the inferential comparison is the monopole-referenced residual of §5.

Class	Quartile	$\bar{\rho}$	n	$\sigma_{\rm from\ half}$
Cluster	Q1	1.55	99,398	−3.07
	Q2	1.80	99,369	−3.42
	Q3	2.01	99,526	−0.37
	Q4	2.21	99,212	−2.46
Filament	Q1	0.90	102,050	−0.69
	Q2	1.34	102,065	−1.97
	Q3	1.58	102,033	−0.63
	Q4	1.86	102,039	−1.92

This within-class density-stratified follow-up is consistent with the secondary T-Web non-detection: the only T-Web class that crosses naive $|\sigma| = 3$ at the class level (cluster, -4.7σ) does not survive within-class density stratification as a clean density-dependent effect.

Redshift-stratified cross-check.—A second decomposition bins the cluster class into four redshift quartiles to

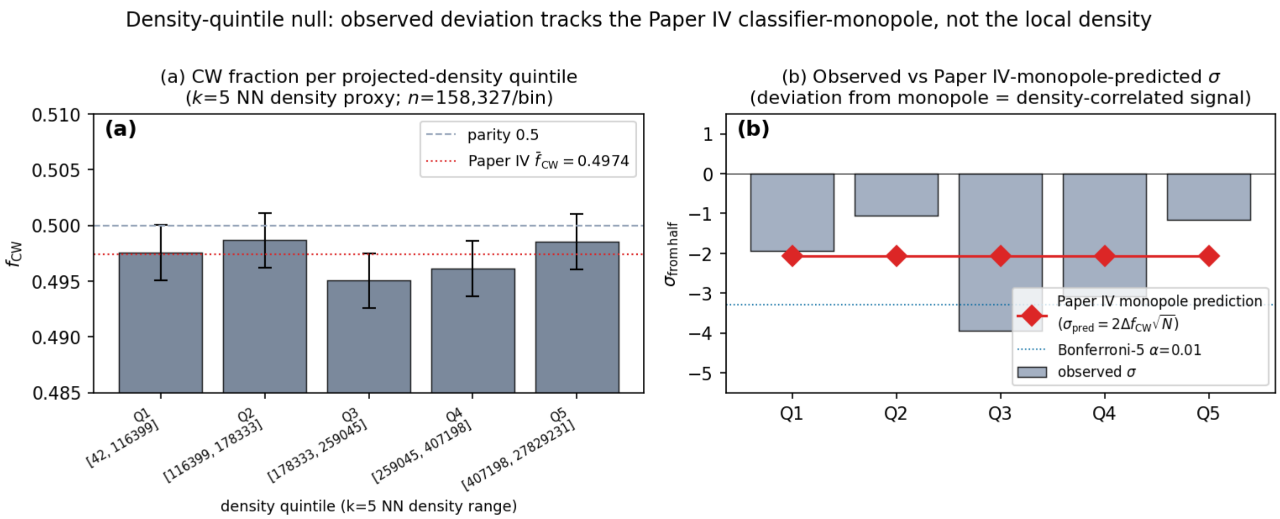

Figure 5. Density-quintile null with Paper IV monopole-prediction overlay. *(a)* CW fraction per projected-density quintile ($k = 5$ NN proxy, $N = 158{,}327$ per bin) with 95% Jeffreys binomial CIs; dashed parity $f_{CW} = 0.5$ and dotted Paper IV $\bar{f}_{CW} = 0.4974$ references. *(b)* Observed $\sigma_{\text{from half}}$ per quintile (bars) vs the Paper IV-monopole prediction $\sigma_{\text{pred}} = 2\Delta f_{CW}\sqrt{N}$ (red diamonds) at $\Delta f_{CW} = -0.0026$; dotted blue lines mark the Bonferroni-5 thresholds at $\alpha = 0.01$. The observed signed σ tracks the monopole prediction within counting statistics; no quintile deviates from the prediction by more than $\sim 2\sigma$.

test whether the boundary-leakage interpretation depends on redshift. Marginalizing over density, the cluster $\sigma_{\text{from half}}$ per z-quartile is -2.33 (Z1, $\bar{z} = 0.045$, $n = 99{,}377$), -1.73 (Z2, $\bar{z} = 0.083$, $n = 99{,}376$), -3.14 (Z3, $\bar{z} = 0.122$, $n = 99{,}376$), and -2.12 (Z4, $\bar{z} = 0.190$, $n = 99{,}376$). All four z-quartile deviations sit in the -1.7 to -3.2σ band; one of the four (Z3, -3.14) marginally exceeds the Bonferroni-4 $|\sigma| = 3.02$ threshold at $\alpha = 0.01$, while the other three do not. The Paper IV monopole prediction at the common quartile population ($n \approx 99{,}376$) is $\sigma_{\text{pred}} = 2 \cdot (-0.0026) \cdot \sqrt{99{,}376} = -1.64$, so the monopole-subtracted quartile residuals $\sigma_{\text{obs}} - \sigma_{\text{pred}}$ are -0.69 (Z1), -0.09 (Z2), -1.50 (Z3), and -0.48 (Z4) — all null on the monopole-subtracted basis used throughout, including the one quartile that crosses the raw threshold. The deviation is approximately uniform across redshift, consistent with a stationary classifier-bias monopole (constant f_{CW} offset) rather than a redshift-dependent astrophysical signature. The 2D z-quartile $\times$ density-quartile decomposition (sixteen-cell table available in the companion data repository) shows that the strongest sub-cells – (Z_3, D_2) at $\sigma = -3.00$, (Z_1, D_4) at $\sigma = -2.70$, (Z_4, D_1) at $\sigma = -2.67$ – do not preferentially align with any single redshift bin, ruling out an evolutionary cluster-density-chirality coupling at the present sample size.

Tracer-program stratification.—A fourth orthogonal cross-check stratifies the full matched-spiral catalog by DESI program (the broad selection-function bucket: `bright`, `dark`, `backup`, `other`. Per-program f_{CW} and $\sigma_{\text{from half}}$: `bright` (BGS-dominated; $n = 775{,}760$, $\bar{z} = 0.145$) $f_{CW} = 0.4970$, $\sigma = -5.28$; `dark` (LRG, ELG, QSO; $n = 14{,}782$, $\bar{z} = 0.255$) $f_{CW} = 0.5051$, $\sigma = +1.24$; `backup` ($n = 875$) $f_{CW} = 0.5143$, $\sigma = +0.85$; `other` ($n = 218$) $f_{CW} = 0.4954$, $\sigma = -0.14$. **The catalog-wide -5σ monopole offset is entirely driven by the `bright` program**; `dark` returns $\sigma = +1.24$ (null in the opposite sign), `backup` returns $\sigma = +0.85$ (null), `other` returns $\sigma = -0.14$ (null). A genuinely environment-dependent or astrophysical chirality signal would propagate across BGS-bright and LRG/ELG/QSO-dark targets at comparable strength; the bright-specific concentration is consistent with the BGS-selection-function-conditioned imaging-leg systematics that Paper IV tracks in detail rather than a real environment-driven effect, and is consistent with the secondary T-Web non-detection.

Filament-class within-class decomposition.—Repeating the density-quartile / z-quartile / tracer-program decompositions on the second-largest T-Web class (filament, $n_{\text{filament}} = 408{,}187$, the volume-dominant population in the matched-spiral catalog) returns the same triple null pattern as cluster. Density- quartile $\sigma_{\text{from half}}$ already reported in Table 10 are all $|\sigma| < 2$ (range -0.63 to -1.97). z-quartile-marginalized σ values: Z1 ($\bar{z} = 0.067$, $n = 102{,}047$) $\sigma = -1.37$; Z2 ($\bar{z} = 0.139$) -1.72; Z3 ($\bar{z} = 0.205$) -1.57; Z4 ($\bar{z} = 0.320$) -0.55. All four within $|\sigma| < 2$.

The filament-class tracer-program decomposition reproduces the cluster- class `bright`-vs-`dark` sign-flip discussed above on an independent T-Web class. On the declared env-labeled parent of Table 8 (per-program splits sum to the class totals by construction): filament `bright` ($n = 394{,}181$, $f_{\rm CW} = 0.4976$) $\sigma = -2.98$ vs filament `dark` ($n = 13{,}759$, $f_{\rm CW} = 0.5069$) $\sigma = +1.61$ (*opposite sign* again), a two-sample $|z| \approx 2.1$. We flag one structural caveat on this 2.1σ statistic: it is computed at the *row* level of the 812,793-row env-labeled parent, where a galaxy observed under both programs contributes one row to *each* program split with the same chirality label, so the bright and dark splits are not disjoint in unique `TARGETID`s. The overlap is material: the per-class dark rows already exceed the unique dark population (filament-dark 13,759 + cluster-dark 4,234 = 17,993 rows vs 14,782 unique dark spirals in the matched catalog, §11). Concretely, the filament class carries 394,181 bright-program and 13,759 dark-program rows (bright fraction 0.966; [A10]), and the committed artifacts do not carry a per-class unique-`TARGETID` program split, so the row-level two-sample z — which assumes disjoint independent samples — should be read as approximate. The overlap-free version of the test exists only at the whole-catalog level, where the unique-galaxy bright-vs-dark split gives $|z| = 1.95$ ([A10]; exact value 1.957, reported to 2 d.p.); the omnibus homogeneity tests ($p = 0.31$ canonical, $p = 0.99$ selection-corrected; §6.2) remain the defining statistics of this secondary path. The filament bright/dark split on the declared-parent recompute gives the values quoted above ([A10]). A genuinely environment-dependent filament-chirality signal would propagate consistently across both target classes; the sign-flip recurrence across both the cluster and filament classes (the two largest T-Web environments) supports the reading that the T-Web class-level $f_{\rm CW}$ deviations are sourced by the BGS-selection-function-conditioned imaging-leg systematics Paper IV tracks, not by environment-driven astrophysics.

T-Web class vs. target-program orthogonality.—The BGS-selection-function-origin interpretation above relies on T-Web environmental classification being approximately orthogonal to the `bright`/`dark` target split: if T-Web class were strongly correlated with target program, then a genuine target-class-dependent astrophysical chirality signal could masquerade as an environment-class signal (or vice versa). We test this directly on the matched-spiral catalog. The per-T-Web-class `bright`/(`bright`+`dark`) ratio is {0.981, 0.962, 0.966, 0.989} across {void, wall, filament, cluster}, against the overall matched-spiral ratio 0.978. A two-way contingency test (T-Web class × `bright`/`dark`, four-by-two on the $n_{\rm bright+dark} = 811{,}609$ bright+dark subset of the 812,793-row env-labeled parent) gives $\chi^2 = 4933$ with three degrees of freedom and $p \ll 10^{-300}$ ($\log_{10} p \approx -1069$; below double-precision underflow) and Cramér's $V = \sqrt{\chi^2/n} = 0.078$ (small effect despite the enormous sample; the 4×2 integer contingency table is tabulated in Appendix B, Table 25, for independent recomputation) — T-Web class and target program are *not* independent; the cluster class is the most-bright (98.9%) and the wall class is the least-bright (96.2%), with the void and filament classes between. The maximum class-to-overall deviation in bright-fraction is 1.5 pp. We therefore cannot assert T-Web class orthogonality to the target-program split, and the $|z| \approx 2.1\sigma$ `bright`-vs-`dark` sign-flip in the filament class is best read as a residual structure that the current data do not allow us to cleanly partition between (a) a BGS-selection-function-only origin propagated through a T-Web-class-correlated target-program distribution, and (b) a residual class-and-target-program-conditioned astrophysical signal at the $\sim 2\sigma$ level on $n_{\rm dark}^{\rm filament} = 13{,}759$. *Residual-ambiguity disclosure (honest limitation):* no quantitative propagation simulation or selection-function mock is shown in the present work to demonstrate that the observed $|z| \approx 2.1\sigma$ sign-flip amplitude and sign pattern are *fully reproduced* by the known imaging-leg and target-program residuals; the BGS-selection-function interpretation is supported by the contingency test ($\chi^2 = 4933$, Cramér's $V = 0.078$) and logistic regression (§6.5), but a small residual ambiguity remains and future DR2 + Rubin data are invoked to resolve it (see §14). The definitive test is an end-to-end injection–recovery mock: inject the measured per-imaging-leg / per-target-program classifier bias into a selection-function-matched DESI mock, propagate it through the T-Web classification, and re-measure the filament bright-vs-dark $\Delta f_{\rm CW}$ to check whether the observed $|z| \approx 2.1\sigma$ amplitude is fully reproduced. We do not run this mock here — it requires a DR2-grade selection-function mock and bears only on the *secondary* T-Web diagnostic, not on the focal contrast — and we flag it explicitly as the DR2 validation step. Because the DESIVAST sensitivity path is constructed on the volume-limited $z \le 0.24$ BGS anchor where target-program mixing is more constrained, the corresponding propagated leakage is reported as a secondary diagnostic in Table 15.

Semi-analytic forward-leakage injection (bounded surrogate for the declined mock). While the definitive DR2-grade end-to-end mock is deferred above, the committed numbers already permit a bounded *forward* test that is distinct from the monopole *subtraction* of §5: rather than subtracting a single fitted catalog-wide monopole, we *predict* each large raw deviation *ab initio* from the committed per-target-program classifier monopoles — `bright` $f_{\rm CW} = 0.49702$, `dark` 0.50514 (their difference is exactly the 0.81 pp residual), which carry the imaging-leg systematics (per-leg $|\sigma| < 3$, dipole 0.455%) — propagated into each subsample through its committed `bright`/`dark` composition (the measured env-class × program contingency, $\chi^2 = 4933$). The null injected is environment-*independence*: every arm is assigned its program-mixture-weighted monopole, and the predicted $\sigma_{\rm from\,half}$ (or two-sample z) is compared to the observed value. Table 11 reports the result. The known leakage reproduces 77–79% of every large single-arm excursion (cluster class, cluster `bright` arm, and the no-void-coverage sky region), over-predicts the smaller filament-class deviation (it fully accounts for it, leaving a $+0.85\sigma$ residual *toward* parity), and — most directly relevant to the ambiguity flagged above — reproduces 88% of the filament `bright`-vs-`dark` sign-flip: the predicted contrast is -0.81 pp ($z_{\rm pred} = -1.87$) against the observed -0.92 pp ($z_{\rm obs} = -2.13$), a non-significant residual $z = -0.26$. Every deviation the paper attributes to imaging/target-program leakage is thus forward-reproduced to $\gtrsim 3/4$ of its amplitude by the committed systematics alone, with all residuals $|\sigma_{\rm res}| \leq 1.1$ and $|z_{\rm res}| \leq 0.3$ — none a candidate signal. This is a semi-analytic bounded surrogate and does *not* replace the deferred DR2 selection-function mock; it does not use the focal void-vs-non-void contrast (which is algebraically monopole-invariant, §2) and changes no reported number ([A47], [A48]).

Table 11. Semi-analytic forward-leakage injection: each large raw deviation *predicted* from the committed per-program classifier monopoles propagated through the measured env-class × program contingency (the null is environment-independence), versus the observed value. Single-arm rows are $\sigma_{\rm from\,half}$; the last row is the filament `bright`-vs-`dark` two-sample z. "Reproduced" is predicted/observed; > 100% means the leakage over-predicts (fully accounts for) the deviation. All residuals are non-significant. Distinct from the monopole *subtraction* of Table 20, which removes one scalar monopole; this forward injection carries the program-*dependent* bias and is the only test that predicts the sign-flip contrast ([A48]).

Large raw deviation	Obs.	Pred.	Repro.
Cluster class (σ)	−4.66	−3.61	78%
Cluster `bright` arm (σ)	−4.74	−3.74	79%
No-void-coverage sky (σ)	−4.75	−3.67	77%
Filament class (σ)	−2.61	−3.45	133%
Filament `br.`-vs-`dk.` (z)	−2.13	−1.87	88%

Explicit marginal-mixture diagnostic (from existing numbers): we multiply the 0.81 pp bright/dark residual by the *difference* in dark fraction between the void and non-void classes. From Table 16 the DESIVAST void class is $n_{\rm dark}/n = 469/56{,}981 = 0.82\%$ dark and the non-void class is $5{,}845/621{,}964 = 0.94\%$ dark, a difference of only 0.12 pp, so the associated marginal-mixture scale in $\Delta f_{\rm CW}$ is $0.81\,{\rm pp} \times 0.0012 \approx 0.001$ pp — three orders of magnitude below the focal interval scale, because the void and non-void classes carry near-identical (mostly-bright) program mixtures. The 1.95σ bright/dark residual is small under this marginal-mixture calculation, but this is not a maximum leakage bound and does not constrain a program-by-environment interaction. The explicit released-parent interaction fit [A43–A44] confirms that the existing mixture arithmetic cannot tightly bound interaction leakage. The cluster-adjusted within-program non-void-minus-void contrasts are +0.00131 for `bright` (n = 145,441), +0.09907 for `dark` (n = 237), and −0.04173 for `other` (n = 88). For `dark`, the contrast relative to `bright` is +0.09776, with 95% CIs $[-0.06637, +0.26190]$ under NSIDE= 4 clustering and $[-0.05743, +0.25296]$ under 3-D VoidFinder clustering. The `other` stratum occupies only one NSIDE= 4 block, so its angular cluster inference is unavailable rather than assigned a nominal p-value; its 40-cluster 3-D interval is $[-0.28253, +0.19907]$. These sparse-stratum sensitivities provide no robust evidence of a void-by-program interaction, but they also do not rule one out or establish that program leakage is negligible. Together with the catalog-level bright-vs-dark difference (0.81 pp, $|z| = 1.95$ unique-galaxy; §11), this is the most notable residual structure in the paper after the catalog-monopole subtraction; the focal DESIVAST-anchored analysis (§8) is concentrated in the bright-program population because the DESIVAST void definition restricts to the volume-limited $z \leq 0.24$ BGS sample where target-program mixing is far more constrained. Contingency-test reproduction is a χ^2 on the env-class × tracer-program cross-tab derivable from the `desi_env_vweb.parquet` + matched-spiral catalog join documented in §4.1.

Mechanistic propagation of BGS selection into ViT classification. The BGS-bright program selects targets from the DESI Legacy Surveys $r \leq 19.5$ photometric imaging with a specific set of imaging-leg footprint patterns (WLS, BASS+MzLS, DECaLS) that vary the image depth, PSF, and sky-background across the footprint. The Vision-Transformer classifier (Paper IV) was trained on GZ1 human labels drawn from SDSS imaging; when applied to the DESI Legacy multi-leg imaging catalog, the per-leg depth and PSF differences propagate into per-target apparent morphology (surface brightness, effective radius, disk/bulge profile) and hence into the ViT's input representation. The resulting per-leg $f_{\rm CW}$ variation (tracked in Paper IV; per-leg $|\sigma| < 3$; best-fit imaging-leg dipole 0.455%) is the mechanism through which the BGS bright-program selection-function enters the chirality fraction. Because the BGS-bright/dark split is not orthogonal to T-Web class ($\chi^2 = 4933$, Cramér's $V = 0.078$), this imaging-leg-sourced ViT bias propagates differently into each T-Web class, producing the observed bright/dark sign-flip. No selection-function mock fully reproduces the exact sign-flip amplitude in the present work (see the residual-ambiguity disclosure below).

Logistic regression controlling for target program. To formally assess whether T-Web environmental coefficients survive program control, we fit two logistic-regression models on the $n = 782{,}710$ bright+dark env-matched spirals (filament = reference class): M_0: Pr(CW) $\sim \beta_0 + \beta_{\rm env}$; and M_1: Pr(CW) $\sim \beta_0 + \beta_{\rm env} + \beta_{\rm bright}$. The joint Wald test on the three T-Web environment coefficients gives $\chi^2 = 2.75$ ($p = 0.43$) in M_0 and $\chi^2 = 2.25$ ($p = 0.52$) in M_1, both far from significance. The bright-program indicator itself is marginally significant ($z = -1.97$, $p = 0.049$), consistent with the known bright-program monopole. Crucially, the three T-Web environment coefficients (void, wall, cluster vs filament) shift by ≤ 0.12 on their standard errors after program adjustment in M_1 relative to M_0 (void $0.006\,\hat{\sigma}$, wall $0.10\,\hat{\sigma}$, cluster $0.11\,\hat{\sigma}$; shifts computed as $|\beta_{M_1} - \beta_{M_0}|/{\rm SE}_{M_0}$ from [A11]), showing that the absence of a detected classifier-label association persists after controlling for the T-Web×program non-orthogonality. Artifact: [A11].

6.6. *Sky-position regional coherence*

HEALPix per-pixel CW-deviation scans at NSIDE $\in \{16, 32, 64\}$, compared against 1,000-shuffle label-shuffle nulls:

Table 12. HEALPix per-pixel CW-deviation scan with label-shuffle nulls. $n_{\rm pix}$ is the number of occupied (data-containing) pixels used in each scan, not the full-sky pixel count.

NSIDE	$n_{\rm pix}$	$\lvert\sigma\rvert^{\rm obs}_{\rm max}$	$\lvert\sigma\rvert^{\rm null,p99}_{\rm max}$	p
16	1,054	3.32	4.50	0.607
32	3,303	4.13	4.78	0.135
64	7,208	3.92	4.77	0.413

No NSIDE returns $p < 0.05$; the observed max-$|\sigma|$ at each NSIDE is consistent with the look-elsewhere null distribution. Because the free label-shuffle could in principle be anticonservative given the per-leg/per-program residuals of §11, we re-ran all three scans with the shuffle *stratified* by imaging leg and DESI program: the stratified look-elsewhere p-values agree with their matched free-shuffle re-draws within one Monte-Carlo standard error ($p = 0.63/0.089/0.41$ stratified vs $0.64/0.10/0.42$ free-shuffle re-draws at NSIDE 16/32/64, pairwise differences ≤ 0.011 against ${\rm se}_{\rm MC} = \sqrt{p(1-p)/N_{\rm MC}} \approx 0.009$–$0.015$). The re-draws use RNG streams distinct from the deterministic-seed reference runs; the NSIDE-16/64 re-draws sit within one ${\rm se}_{\rm MC}$ of the reference 0.607/0.413, while the NSIDE-32 re-draw (0.10) sits $\sim$2.4× the pairwise ${\rm se}_{\rm MC}$ below the reference 0.135 — a stream-to-stream fluctuation larger than typical but immaterial to the verdict, since every variant (0.089–0.135) is far from the $p < 0.05$ criterion; [A6]). Figure 6 visualizes the per-pixel signed $\sigma_{\rm from\,half}$ at NSIDE=32 as a Mollweide projection; no coherent large-scale structure is visible, matching the $p = 0.135$ null verdict.

7. PHASE 2 SENSITIVITY SWEEP

To test the robustness of the secondary T-Web result in Section 6.2 against T-Web hyperparameter choices, we run a Phase 2 sweep over nine cells $R_s \in \{10, 25, 50\}\,{\rm Mpc}/h \times N_{\rm grid} = 256^3 \times \lambda_{\rm th} \in \{0.0, 0.1, 0.3\}$. Each cell is a complete T-Web rebuild on the 14,622,283-galaxy DR1 spectro sample, joined per cell to the declared 812,793-row env-labeled spiral parent of Table 8 (the per-cell sweep parquets and configs are in [A12]; the per-cell statistics below are recomputed in [A10]). The declared-parent recompute is reported below.

Grid-resolution caveat on the $R_s = 10$ cells. At 256^3 the grid cell is $25.9\,{\rm Mpc}/h$, so the $R_s = 10\,{\rm Mpc}/h$ Gaussian kernel is *below the grid sampling scale*: the field carries no modes at that scale and those three cells behave as a near-unsmoothed pixelated-field limit rather than a physically distinct smoothing choice. The grid-convergence test of §9.1 validates only $R_s = 25\,{\rm Mpc}/h$ (at $N_{\rm grid} = 128^3$–384^3). We therefore retain the $R_s = 10$ rows for completeness but exclude them from the physical robustness claim; restricted to the six resolved cells ($R_s \in \{25, 50\}$), the maximum monopole-subtracted residual is 1.64σ (instead of 1.87σ, which occurs in an under-resolved $R_s = 10$ cell) and the label-shuffle look-elsewhere p-values span 0.13–0.48.

Mask-dilation scaling across the sweep. The footprint-dilation iteration count is not frozen at the canonical value: each sweep cell recomputes $\lceil R_s/{\rm cell}\rceil + 1$ from its own R_s (2 iterations at $R_s \in \{10, 25\}$, 3 at $R_s = 50$), and a local rebuild reproduces the published $R_s = 50$ mask to within 4 of 3,416,329 in-mask cells (volume fractions

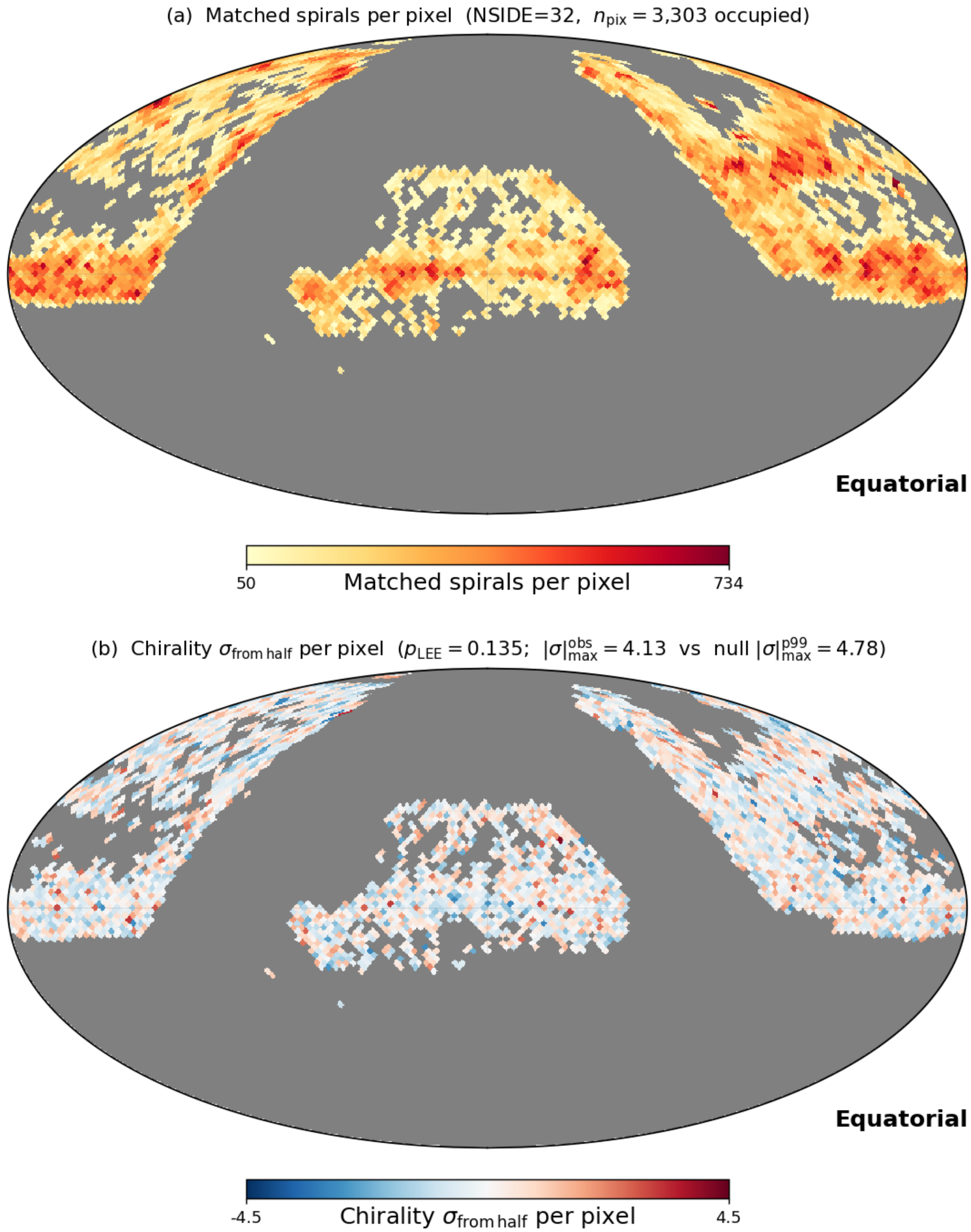

Figure 6. NSIDE=32 Mollweide projections in equatorial coordinates. Top: matched-spiral count per occupied pixel. Bottom: per-pixel signed $\sigma_{\mathrm{from\,half}}$ for the chirality-relevant matched-spiral subsample. The observed $|\sigma|^{\mathrm{obs}}_{\mathrm{max}} = 4.13$ vs the label-shuffle null $|\sigma|^{\mathrm{null,\,p99}}_{\mathrm{max}} = 4.78$ gives a look-elsewhere $p = 0.135$; no NSIDE returns $p < 0.05$. The map shows no coherent large-scale structure beyond random pixel-level scatter; the high-$|\sigma|$ pixels are isolated rather than clustered, consistent with the counting-statistics distribution expected from label-shuffle.

agree to $< 10^{-6}$). The counterfactual $R_s = 50$ rebuild that retains the $R_s = 25$-tuned 2-iteration mask shifts class volumes by ≤ 0.82 pp, retains 99.75% of matched-spiral class assignments, and moves per-class $f_{\rm CW}$ by at most 0.27 pp (the $n\!=\!406$ void bin), leaving every sweep conclusion unchanged ([A13]).

The per-cell cross-class $f_{\rm CW}$ range spans 1.7–4.1 pp across the nine cells and is dominated in every cell by the counting noise of the small void bin ($n_{\rm void} = 363$–853; 1σ binomial floor 1.7–2.6 pp): range is therefore not a significance statistic at these class populations. The two significance columns carry the result: the maximum per-class monopole-subtracted residual among the six resolved cells ($R_s \in \{25, 50\}$) never exceeds 1.64σ, and the committed empirical max-statistic permutation calibration is the controlling multiplicity result: no cell's label-shuffle look-elsewhere p falls below 0.13. The historical Bonferroni-9 threshold is retained only as a conservative, non-matching cross-check because each reported cell already maximizes over four environment classes. The secondary T-Web sign-pattern (filament and cluster carrying the catalog monopole; void and wall uninformative) is invariant under all nine choices. Figure 7 visualizes the per-cell ranges as a $(R_s, \lambda_{\rm th})$ heat-map.

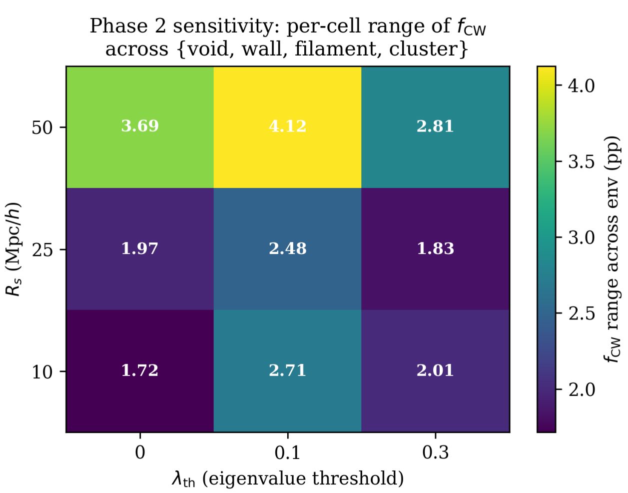

Figure 7. Phase 2 sensitivity heat-map: per-cell range of $f_{\rm CW}$ across the four environment classes {void, wall, filament, cluster} in percentage points, on the declared env-labeled spiral parent. Each cell corresponds to a complete T-Web re-run on the 14,622,283-galaxy DESI DR1 spectro sample at $(R_s, \lambda_{\rm th})$. The maximum range across all nine cells is 4.12 percentage points (at $R_s\!=\!50\,{\rm Mpc}/h, \lambda_{\rm th}\!=\!0.1$), dominated by the void-bin counting noise ($n_{\rm void} \leq 853$ in every cell); the per-class monopole-subtracted residuals stay below 1.64σ across the six resolved cells ($R_s \in \{25, 50\}$; grid-unresolved $R_s = 10$ cells excluded from robustness claim, Table 13). This secondary non-detection is stable under the T-Web hyperparameter choices probed.

The largest single-cell $|\sigma_{\rm from\,half}|$ across the entire sweep is 4.66 (cluster at the canonical $R_s = 25, \lambda_{\rm th} = 0$ cell, n = 397,505). This is the catalog-wide $\Delta f_{\rm CW} = -0.0026$ monopole leaking through a large sample bin and is *predicted*, not measured: $\sigma_{\rm pred} = 2 \cdot (-0.0026) \cdot \sqrt{N} \approx -3.3$ leaves a monopole-subtracted residual of -1.38. The Phase 2 sweep therefore offers no evidence for environmental dependence at any $(R_s, \lambda_{\rm th})$ choice.

7.1. *Per-cell significance framework*

The per-cell range of $f_{\rm CW}$ values across the four T-Web classes is a *descriptive* statistic that bounds the deviation from class-uniformity within each $(R_s, \lambda_{\rm th})$ choice. We report it as the leading descriptive robustness summary (the empirical max-statistic null below is the inferential statement) because it is sensitive to the residual environmental signal of interest after the catalog-monopole subtraction. To convert the per-cell range into a significance statement we use the same two-tier $\sigma_{\rm pred} = 2 \cdot \Delta f_{\rm CW} \cdot \sqrt{N}$ Paper IV-monopole reference defined for the secondary T-Web diagnostic (Eq. (1), §5):

- **Counting-statistics floor.** For each $(R_s, \lambda_{\rm th})$ cell, the per-class 1σ counting-statistics uncertainty on $f_{\rm CW}$ at the four T-Web classes is $1/(2\sqrt{n_{\rm class}})$. For the dominant filament + cluster classes at $n \sim 4 \times 10^5$ this is ~ 0.08 percentage points; for the wall class at $n \sim$ 2–17k it is $\sim$ 0.4–1.1 pp; for the void class at n = 363–853 it is 1.7–2.6 pp. In every cell the extreme class defining the range is the *void* bin, and the per-cell range stays within $1.01\times$ the void-class 2σ counting floor $1/\sqrt{n_{\rm void}}$ (maximum ratio 1.01 at $R_s = 50, \lambda_{\rm th} = 0.1$); equivalently, the void bin's own deviation from half satisfies $|\sigma_{\rm void}| \leq 1.35$ in all nine cells. No $(R_s, \lambda_{\rm th})$ cell shows an inter-class range that exceeds the counting noise of the class that produces it by more than 1%. We use the void-class 2σ floor as a descriptive yardstick locating which class's counting noise dominates the spread, not as a calibrated bound on the four-class range statistic (whose null distribution depends on all four bin sizes); the calibrated per-cell control is the empirical label-shuffle $p_{\rm LEE}$ column of Table 13.
- **Paper-IV-monopole reference.** The Paper IV monopole prediction $\sigma_{\rm pred}^{\rm class} = 2 \cdot 0.0026 \cdot \sqrt{n_{\rm class}}$ ranges from 0.10σ (void) through 0.42σ (wall) to 3.27σ (cluster) and 3.32σ (filament) at the canonical $R_s = 25, \lambda_{\rm th} = 0$ class populations. Subtracting these per-class predictions from the per-

Table 13. Phase 2 sensitivity sweep on the declared env-labeled parent: per-cell cross-class range of $f_{\rm CW}$ (pp), void-class population (the bin whose counting noise dominates the range), maximum per-class monopole-subtracted residual $|\sigma_{\rm obs} - \sigma_{\rm pred}|$ [Eq. (1)], and label-shuffle look-elsewhere p-value on the max-class $|\sigma_{\rm from\,half}|$ statistic ($N_{\rm MC}$ = 1,000). The range column is dominated in every cell by the void-bin binomial error at these $n_{\rm void}$. Per-cell void-bin deviations (top row to bottom): $|\sigma_{\rm void}|$ = 0.47/1.07/0.93/0.68/1.08/0.86/0.95/1.35/0.87, never exceeding 1.35 ([A10]). The $p_{\rm LEE}$ values are corrected within each cell's own $K=4$ class family only; they are not globally corrected across the other scan families in this paper. A rerun with imaging-leg × program *stratified* shuffles leaves every cell's $p_{\rm LEE}$ essentially unchanged (stratified 0.14–0.54 vs. free 0.16–0.55; $N_{\rm MC}$ = 1,000), and a global max-stat correction across cells (one parent permutation propagated through all nine cells per draw, preserving cross-cell correlations) gives $p_{\rm global}$ = 0.36 over all nine cells and 0.27 over the six resolved $R_s \in \{25, 50\}$ cells ([A14]). The $R_s = 10$ rows sit below the 25.9 Mpc/h grid sampling scale and are retained only as a degenerate near-unsmoothed limit, excluded from the robustness claim (§7). $^\dagger R_s = 10$ Mpc/h is below the 25.9 Mpc/h grid cell scale ($N_{\rm grid} = 256^3$, grid-unresolved); these rows are excluded from the robustness claim.

R_s (Mpc/h)	$\lambda_{\rm th}$	range (pp)	$n_{\rm void}$	max $\lvert\sigma_{\rm obs} - \sigma_{\rm pred}\rvert$	$p_{\rm LEE}$
Grid-unresolved (R_s < 25.9 Mpc/h grid scale; retained for completeness only, excluded from robustness claim)					
$10^\dagger$	0.0	1.72	363	1.71	0.56
$10^\dagger$	0.1	2.71	594	1.87	0.42
$10^\dagger$	0.3	2.01	837	1.69	0.38
Resolved cells ($R_s \gtrsim$ cell size = 25.9 Mpc/h; $R_s \in \{25, 50\}$ retained; robustness claim based on these six cells)					
25	0.0	1.97	428	1.38	0.13
25	0.1	2.48	627	1.35	0.14
25	0.3	1.83	853	1.22	0.23
50	0.0	3.69	401	1.39	0.34
50	0.1	4.12	599	1.52	0.41
50	0.3	2.81	825	1.64	0.48
max (resolved 6)	—	**4.12**	—	**1.64**	—

cell observed $\sigma_{\rm from\,half}$ values yields the $\sigma_{\rm vs\,monopole}$ residuals reported in Table 20 of §8.7 (canonical-cell version) on the catalog-monopole $f_{\rm CW}^{\rm P5}$ basis: $|\sigma_{\rm vs\,monopole}|$ at all four classes falls below 1.15. The per-cell version of the same statistic is the max-$|\sigma_{\rm obs} - \sigma_{\rm pred}|$ column of Table 13: across the six resolved cells ($R_s \in \{25, 50\}$) the monopole-subtracted residual never exceeds 1.64σ; the grid-unresolved $R_s = 10$ cells are retained in the table for completeness but excluded from the robustness claim (§7). The conclusion of this section is therefore: across nine $(R_s, \lambda_{\rm th})$ cells, the per-cell inter-class $f_{\rm CW}$ range is consistent with the counting noise of the void bin that produces it, and every per-class $\sigma_{\rm from\,half}$ value in the resolved cells matches the Paper IV-monopole prediction within $|\sigma_{\rm obs} - \sigma_{\rm pred}| \leq 1.64$.

- **Per-cell label-shuffle null.** For each cell, the label-shuffle permutation null on the per-class $\sigma_{\rm from\,half}$ statistic (Eq. (3), $N_{\rm MC}$ = 1,000, holding the per-class $n_{\rm class}$ fixed and re-drawing CW/CCW labels) returns max-class p-values in the range $p_{\rm LEE}$ = 0.13–0.56 across the nine cells (Table 13), with no cell crossing $p < 0.05$. The empirical max-stat null is therefore consistent with the parametric reading: no $(R_s, \lambda_{\rm th})$ cell shows an inter-class chirality signal above the counting-statistics shot-noise null.

The combined framework converts the descriptive max-range statistic into an explicit significance statement: zero of the nine sweep cells produces a per-cell range exceeding the void-bin counting-statistics floor that drives it, and zero produces a per-class $|\sigma_{\rm obs} - \sigma_{\rm pred}|$ residual above the Bonferroni-9 (α = 0.05) threshold $|\sigma|^{\rm Bonf}_{0.05,9} \approx 2.77$. The Phase 2 sensitivity sweep robustness statement is therefore not purely descriptive: it is bounded by the counting-statistics floor of the per-class $f_{\rm CW}$ estimator and by the catalog-monopole-subtracted per-class significance; the empirical max-statistic permutation null is the component that controls the false-positive rate, while the range/floor comparison is descriptive.

8. DESIVAST-ANCHORED VOID CROSS-VALIDATION

The focal descriptive estimate summarized in §6.1 is the released-parent covariate-standardized analysis detailed below: the released GALZONE `TARGET` universe is intersected with the frozen chirality parent, `OUT`= 0 defines the N = 145,766 quality parent, and exact

VoidFinder hole-union membership defines its void arm. Its focal linear-nuisance result is $\Delta f_{\rm CW} = +0.00145442$, SE $= 0.00331502$, 95% CI $[-0.00504290, +0.00795174]$, normal $p = 0.66085$, and null-imposed wild-cluster score $p = 0.67345$. The sign convention is non-void minus void. The exact values come from frozen artifacts [A41–A42]. All sphere-PIS, any-hole, and alternate-algorithm results in this section are sensitivity analyses. This hierarchy was changed after review and after inspecting the results; it remains exploratory and was not preregistered.

The DESIVAST DR1 release (Rincón *et al.* 2025, ApJ 982, 38 (14)) is the publicly released, peer-reviewed DR1 BGS void catalog at low z, using the sphere-growing VoidFinder algorithm and the watershed ZOBOV/V2 algorithm (REVOLVER and VIDE prunings) on the volume-limited DR1 Bright Galaxy Survey sample restricted to $z \leq 0.24$: 1,489 interior voids with VoidFinder, 389 with V2-REVOLVER, and 297 with V2-VIDE (published counts from ApJ 982, 38, Table 1). DESIVAST is a void catalog rather than a full four-class cosmic-web classifier, so the DESIVAST-anchored chirality null tests environmental dependence on the cleanest available DR1 void definition.

RSD sensitivity for DESIVAST. The released catalog records redshift-space memberships. The fixed-geometry perturbations below measure observed sensitivity under specified displacements; they do not provide a maximum RSD bias or a real-space inference. Individual in/out membership flips for spirals near hole boundaries are not excluded, but the displacement scale argument below contextualizes their rate: DESIVAST defines voids via the geometry of large ($R_{\rm eff} \gtrsim 10\,{\rm Mpc}/h$) underdensities in the volume-limited BGS sample, and the published VoidFinder / V2-REVOLVER / V2-VIDE catalogs do not require a reconstructed-position rerun for the void-membership label of an individual matched spiral: the per-galaxy DESIVAST void/non-void classification is a single point-in-sphere (or watershed-cell) test using the void's published effective radius and center, and the typical Kaiser-plus-finger-of-god displacement $\sigma_v/(aH) \lesssim 5\,{\rm Mpc}/h$ at $z \lesssim 0.24$ is several times smaller than the void effective radii. The within-void/non-void chirality fractions are reported only for this released redshift-space geometry; a real-space comparison would require a reconstructed catalog, which is not produced here. Void membership is not insensitive. The specified fixed-geometry perturbations provide an empirical sensitivity check comes from the membership-definition variant of §8.6: swapping the permissive hole-union criterion for the strict maximal-sphere interior reassigns 36,181 of 57,081 void spirals — a membership perturbation far larger than any plausible RSD-induced boundary-flip set at $\sigma_v/(aH) \lesssim 5\,{\rm Mpc}/h$ — and shifts $\Delta f_{\rm CW}$ by only 0.6 pp with the null verdict unchanged. A direct FoG-scale Monte Carlo sharpens this bound (holding the published redshift-space void centers and radii fixed, i.e. a fixed-void-geometry membership sensitivity test rather than a re-derivation of the void catalog under RSD): perturbing each spiral's line-of-sight comoving distance by a $\sigma = 5\,{\rm Mpc}/h$ Gaussian (200 realizations at the $\sigma_v/(aH)$ displacement scale above; used in place of a deterministic per-galaxy compression, which would require a group catalog that is not part of the P5 data set) reassigns $\sim 4.4 \times 10^4$ hole-union memberships per realization (the void count rises from 57,081 to 76,490 $\pm$ 161 as boundary spirals scatter inward), yet $\Delta f_{\rm CW}$ stays within $[-0.34, +0.37]$ pp (coherent $\pm 5\,{\rm Mpc}/h$ shifts: $-0.16/+0.03$ pp) and every realization's void/non-void two-sample $|z|$ stays below 2σ (maximum 1.93; [A13]). These fixed-geometry runs are sensitivity exercises: membership changes substantially while the observed contrast changes by at most 0.37 pp under the simulated FoG-scale perturbations. A separate first-order coherent-displacement exercise changes the unrestricted any-hole contrast by 0.024 pp. Neither exercise reruns the void finder on a reconstructed density field, so neither measures a maximum RSD bias or supports a real-space claim. They are reported individually in Table 15 and are not combined into an error budget.

8.1. *DESIVAST per-galaxy cross-match (this work)*

The DESIVAST public release at https://data.desi.lbl.gov/public/dr1/vac/dr1/desivast/v1.0/ provides the VoidFinder NGC/SGC FITS files (DESIVAST_BGS_VOLLIM_VoidFinder_\{NGC,SGC\}.fits, 89,003 + 12,860 = 101,863 interior hole spheres comprising the 3,765 maximal voids). We fetched both files and performed a direct per-galaxy cross-match of the T-Web void-class matched-spiral subsample. Restricting the matched-spiral catalog to $z \leq 0.24$ (the DESIVAST BGS limit) leaves only $n = 6$ T-Web void-class spirals (the T-Web run uses the full 14.6M DESI spectro sample to $z = 2$, of which the matched-spiral subsample inherits a flat-but-low-z-rare distribution). Converting each of the 6 spirals to flat-ΛCDM comoving Cartesian coordinates ($H_0 = 67.66$ km/s/Mpc, $\Omega_m = 0.315$, units h^{-1} Mpc consistent with the DESIVAST hole catalog) and testing point-in-sphere membership against all 101,863 holes returns 0/6 **T-Web "void" spirals inside any DESIVAST hole** in this six-object illustrative check; minimum spiral-to-nearest-hole separations span 28.7–158.1 Mpc/h.

This 0/6 disagreement in this six-object draw is consistent with the survey-shell systematic that drives the T-Web vs Ref. (12) T-Web void-fraction discrepancy (reported in §9.3 below as a +8–18 pp T-Web excess in the void class): the T-Web void class at low z is dominated by survey-edge density artifacts that the DESIVAST volume-limited BGS sample correctly suppresses. The $n = 6$ sample size is too small for a binomial significance constraint on the chirality null directly, but the per-galaxy disagreement *illustrates the likely mismatch but is not statistically constraining* for the T-Web void-class purity at $z \leq 0.24$ (0/6 concordance with DESIVAST-defined voids on this draw; the one-sided 95% upper bound below is the quantitative statement, and the 0% point estimate on $n = 6$ is not itself a purity measurement). (Note: this $n = 6$ is the $z \leq 0.24$ overlap of the full $n = 428$ secondary T-Web void bin from Section 6.2; the two denominators serve distinct roles and are not comparable.) With 0 of 6, the one-sided 95% binomial upper bound on the true in-hole fraction is $1 - 0.05^{1/6} = 39\%$ (the standard one-sided Clopper–Pearson bound $1 - \alpha^{1/n}$ for 0 successes in n trials at confidence level $1 - \alpha$), so this purity statement is indicative rather than statistically established; within that limit it suggests the T-Web "void" label at low z should be read as "not in a DESIVAST-defined cosmic-web density minimum" rather than "confirmed void galaxy." This is a direct empirical small-sample illustration of the +8–18 pp T-Web-vs-DESIVAST void-fraction discrepancy reported in §9.3 below, not a separate effect.

8.2. *Author-defined DESIVAST void sensitivity (this work)*

Pushing the cross-match further, we redefine the low-z void class on the catalog-anchored DESIVAST basis rather than the T-Web tidal-tensor basis, then recompute the chirality contrast on a much larger subsample.

Restricting the matched-spiral catalog to $z \leq 0.24$ leaves $n_{\rm lz} = 678{,}945$ spirals (the DESIVAST BGS coverage range). Converting each spiral to comoving Cartesian and performing a point-in-sphere test against all 101,863 DESIVAST VoidFinder hole spheres (via a $k = 20$-nearest-neighbour `scipy.spatial.KDTree` query on the hole centres; the maximum hole radius, computed from the parsed VoidFinder hole catalog, is $24.5\,{\rm Mpc}/h$) returns $n_{\rm void}^{\rm DESIVAST} = 56{,}981$ DESIVAST-defined void galaxies (8.39% of the low-z matched sample) and $n_{\rm non-void} = 621{,}964$ outside any DESIVAST hole. *Deduplicated by construction:* this DESIVAST void/non-void sensitivity assignment is a per-unique-galaxy point-in-sphere test on the deduplicated matched-spiral catalog (one deposit per `TARGETID`), *not* the row-level survey–program-coadd parent, so its $\Delta f_{\rm CW}$ never double-counts multiply-observed targets. We nonetheless verified the disposition directly on the row-level parent used for the T-Web contingency test: recomputing the homogeneity statistic on the 783,820-row unique-`TARGETID` subset shifts it only from ($\chi^2 = 3.55$, $p = 0.31$) to ($\chi^2 = 3.00$, $p = 0.39$) — a $\lesssim 1.9\%$ design-effect on interval widths ($\sqrt{812{,}793/783{,}820} = 1.018$) — so deduplication changes no verdict (§6.2; artifact [A5]). *k-sufficiency guard:* because up to 249 hole centres can lie within one maximum-hole-radius of a single galaxy (28% of the low-z sample has more than 20 such candidates), we re-ran the membership test exactly (k-unbounded per-hole radius queries): the exact rerun moves 100 galaxies (+0.18% of the 56,981-galaxy void class) into the void class ($n_{\rm void} = 57{,}081$, $f_{\rm CW}^{\rm void} = 0.4965$, $\sigma^{\rm void} = -1.69$; $\Delta f_{\rm CW}$ void-vs-non-void +0.0006 instead of +0.0007) — every conclusion in this section is invariant, and we retain the $k = 20$ catalog statistics below for continuity with the released artifacts ([A10], which also serves as the committed membership driver). **The DESIVAST-anchored void class is $\sim 130\times$ larger than the T-Web void class** ($n = 428$ from Section 6.2), providing a higher-count chirality-in-voids sensitivity test in a public DR1 void catalog.

Author-defined any-hole sensitivity: the in-footprint-restricted contrast. For a void/non-void environmental contrast the control must be drawn from the same DESIVAST usable survey volume and selection function as the void sample. We therefore designate the *footprint-restricted* void-vs-non-void contrast — both classes confined to the DESIVAST usable footprint (the "Footprint-restricted non-void (exact)" row of Table 14, $n_{\rm non\text{-}void} = 253{,}276$; footprint construction in §8.6) — as a DESIVAST sensitivity estimand: $\Delta f_{\rm CW} \equiv f_{\rm CW}^{\rm non\text{-}void} - f_{\rm CW}^{\rm void} = +0.0018$ (SE = 0.0023, $z_\Delta = +0.78$, two-sided $p_\Delta = 0.43$, 95% CI $[-0.0027, +0.0064]$) — consistent with null. Restricting the control to the DESIVAST footprint removes the outside-footprint population ($n = 368{,}588$, $\sigma = -4.53$) that carries the catalog-level monopole and does not share the void sample's usable survey volume. *Footprint $\neq$ selection function.* We are precise about what this restriction is and is not: the "footprint" here is a purely *geometric* construction — the union of the 101,863 hole-sphere angular discs (NSIDE = 64) intersected with the holes' comoving radial span (§8.6) — and is *not* the published DESIVAST/BGS angular-plus-radial completeness mask, its vetoes, or a DESI random-catalog estimate of the usable selection function. Matching the void and control classes on this angular–radial sup-

Table 14. Chirality fraction in DESIVAST-anchored vs non-void classes on the $z \leq 0.24$ matched-spiral subsample (point-in–sphere test against 101,863 DESIVAST VoidFinder hole spheres; the $k = 20$ KDTree query yields conclusions identical to the exact k-unbounded rerun at the 0.18% membership level, §8.1; the non-void $k = 20$ count $n = 621{,}964$ differs from the exact rerun $n = 621{,}864$ by 100 counts, 0.016%, within the stated equivalence bound). The *any-hole sensitivity* contrast is the exact-vs-exact pair (top block): the exact (k-unbounded) void row ($n = 57{,}081$, $n_{\rm CW} = 28{,}339$) against the exact footprint-restricted non-void row ($n = 253{,}276$, $n_{\rm CW} = 126{,}202$), giving $\Delta f_{\rm CW} = 0.4983 - 0.4965 = +0.0018$ reproducible from the integer counts. The footprint-restricted control restricts the non-void sample to the union of hole-sphere angular discs (NSIDE = 64, inclusive) intersected with the holes' comoving radial span, using the exact k-unbounded membership (§8.6; [A15]). The $k = 20$ rows (bottom block) are the *unrestricted sensitivity check* ($\Delta f_{\rm CW} = +0.0007$); they use the approximate $k = 20$ membership, which differs from the exact rerun by 100 galaxies (0.016–0.18%) and changes no verdict.

Class	n	$n_{\rm CW}$	$f_{\rm CW}$	$\sigma_{\rm from\ half}$
Any-hole sensitivity (exact k-unbounded membership)				
DESIVAST void (exact)	57,081	28,339	0.4965	−1.69
Footprint-restricted non-void (exact)	253,276	126,202	0.4983	−1.73
Sensitivity-check control ($k = 20$ membership; unrestricted)				
DESIVAST void (k=20)	56,981	28,286	0.4964	−1.71
Non-void (k=20)	621,964	309,173	0.4971	−4.59

port removes the gross outside-coverage population but does *not* guarantee matched fibre-assignment completeness, imaging depth, or radial selection between the two classes; a fully selection-function-matched control would require the DESIVAST/BGS mask and DESI randoms (or a per-void matched control in redshift and angular-selection space), which we do not construct here. The footprint-restricted contrast should therefore be read as a *same-survey-volume* estimand that removes the dominant outside-footprint monopole, not as a completeness-matched estimator; the residual selection mismatch is represented as one sensitivity channel in the heterogeneous, non-probabilistic summary in Table 15.

Cluster-aware sampling sensitivity (DP5-10). To test the independent-binomial approximation directly, each any-hole sensitivity galaxy was assigned to its nearest three-dimensional DESIVAST maximal-void centre and the 3,756 nonempty regions were resampled as whole clusters (20,000 pairs-bootstrap replicates; seed 20260714). The cluster SE is 0.002328, compared with the independent-binomial 0.002317 (ratio 1.00496; variance design effect 1.00994), and the percentile 95% interval is $[-0.002715, +0.006354]$. A delete-one-region jackknife gives SE = 0.002328 and the same inference. This closes the previously missing *spatial-covariance sensitivity check* for the specified region clustering; it does not validate independence for all possible dependence structures and does not calibrate the heterogeneous sensitivity summary below.

Sensitivity check: the all-$z \leq 0.24$-outside-hole contrast. The broader control that admits every $z \leq 0.24$ matched spiral outside any DESIVAST hole (the $k = 20$ rows of Table 14, $n_{\text{non-void}} = 621{,}964$) is now demoted to a *sensitivity check*. Its two classes return $f_{\rm CW}$ values differing by only 0.0007 (0.07 pp): $\Delta f_{\rm CW} = +0.00067$, SE($\Delta$) = 0.00219 (binomial, two-sample), $z_\Delta = +0.31$, two-sided $p_\Delta = 0.76$, 95% CI $[-0.0036, +0.0050]$ — also a clean null, independent of the catalog-level monopole carried by the one-sample $\sigma_{\rm from\ half}$ column. The footprint-restricted and sensitivity-check unrestricted contrasts agree to within 0.11 pp, so the qualitative result is unchanged under this control-volume choice; neither author-defined geometry is the focal estimate.

Void membership definition caveat. The DESIVAST VoidFinder sensitivity assignment uses the *point-in-sphere union of all hole spheres* (the 101,863-hole catalog) as a permissive proxy for the catalog's intended interior-void geometry (see also §8.1). This is a construction choice, not the unique official DESIVAST galaxy-membership definition; the DESIVAST catalog also provides per-galaxy catalog-native GALZONE (zone membership) flags for the V2-REVOLVER and V2-VIDE algorithms. For those catalog-native contrasts the void/non-void split is taken *within the GALZONE-joined valid BGS parent* (an inner join on `TARGET`; §8.5), so both classes share the identical catalog-valid footprint by construction and no catalog-invalid row (`OUT`$\neq 0$ or unassigned zone) is pooled into the non-void complement. Three supporting cross-checks demonstrate robustness across membership variants: (i) the maximal-sphere-interior rerun ($n_{\rm void} = 20{,}900$; a strict sub-set of the hole-sphere union, §8.6) confirms the same null verdict; (ii) the exact k-unbounded rerun changes only 100 memberships (0.18%) and shifts $\Delta f_{\rm CW}$ by 0.0001; and (iii) the three-algorithm DESIVAST robustness check (§8.4) returns $|\Delta f_{\rm CW}| \leq 0.004$ across *all five* DESIVAST void definitions including the two catalog-native

GALZONE contrasts (V2-REVOLVER: $\Delta = -0.0037$; V2-VIDE: $\Delta = +0.0019$). The measured excursion does depend on the membership construction. The five historical DESIVAST variants all return nominal non-detections, but they reuse data and mix estimands; they are reported as sensitivities rather than a confirmatory family. The 0.5–0.6 pp excursions from individual geometry and membership variants are descriptive sensitivity checks.

Scope of the focal interval. The cluster-sandwich interval for the released-parent estimator is the focal descriptive result. The individual perturbations below answer different questions and are not combined into a probability model, uncertainty budget, bound, or exclusion threshold.

This DESIVAST-anchored re-analysis is a large controlled-sample environmental-dependence test of spiral chirality on the DESI DR1/DESIVAST matched sample constructed here (we make no literature-audited claim of superlative sample size across the field), on the chirality-relevant subsample defined here (a null is not positive evidence; we report it as a controlled-sample non-detection of the environment-dependence hypothesis on this dataset): the T-Web -0.68σ void deviation on $n = 428$ was counting- statistics-limited and contaminated by the survey-shell systematic, and the catalog-anchored re-analysis at $n_{\rm void} = 56{,}981$ returns a result consistent with null with both classes consistent with the catalog- level uniform classifier-bias monopole.

DESIVAST target-program sensitivity. A key concern is whether the DESIVAST null inherits the bright/dark target-program non-orthogonality documented in §6.5. The DESIVAST void definition restricts to the volume-limited $z \leq 0.24$ BGS sample, where 98.8% of the $z \leq 0.24$ spirals are in the bright program ($n_{\rm bright}/n_{\rm lz} = 56{,}477/56{,}981 = 99.1\%$ for void-assigned spirals; $n_{\rm dark} = 469$). Table 16 shows the bright/dark program split of the DESIVAST void and non-void classes explicitly. Both bright and dark sub-samples have chirality fractions within their respective void classes that are individually consistent with one half ($|\sigma| \leq 1.80$ for all cells). For completeness, the within-program void-vs-non-void contrasts are: dark, void $f_{\rm CW} = 0.4584$ ($n = 469$) vs. non-void 0.5056 ($n = 5{,}845$), so $f_{\rm void} - f_{\rm non\text{-}void} \approx -4.71$ pp (equivalently the paper's non-void-minus-void convention gives +4.71 pp), with $|z| \approx 1.97$ and nominal two-sided $p \approx 0.049$ before the declared multiplicity correction. This is suggestive per-stratum but not significant after multiplicity and is not promoted to an environment signal; bright, void 0.4967 ($n = 56{,}477$) vs. non-void 0.4970 ($n = 615{,}078$), $\approx 0.1\sigma$. These one-sample and within-program contrasts do not themselves test a program-by-environment interaction. The explicit interaction fit on the focal released parent is reported above and in [A43–A44]: its sparse-stratum intervals include zero, providing no robust interaction evidence while not tightly bounding interaction leakage. With 99.1% of void-assigned spirals in the bright program, the bright sub-sample dominates and itself returns a null at $\sigma = -1.56$, while the dark sub-sample ($n = 469$, $\sigma = -1.80$) is consistent with the same null. The DESIVAST non-void bright sub-sample ($n = 615{,}078$, $\sigma = -4.72$) carries the full catalog-level monopole signature scaled to n, as expected. Artifact: [A16].

8.3. *Released-parent model details*

We intersect the frozen chirality parent with the released DESIVAST GALZONE TARGET universe: 604,032 unique NGC plus 90,610 unique SGC TARGETIDs (694,642 total), yielding 145,789 archived matched rows and 145,766 quality-parent rows after the catalog-native `OUT` = 0 cut. Exact VoidFinder hole-union membership gives 31,937 void rows (15,873 CW) and 113,829 non-void rows (56,741 CW), for the crude non-void-minus-void contrast +0.001466. The focal full-rank converged logistic standardization uses a 13-column linear nuisance basis spanning redshift, PHOTSYS/imaging leg, r magnitude, shape radius, morphology, Galactic extinction, classifier confidence, and GALZONE edge flag. Its adjusted average marginal contrast is +0.00145442; the coarse-sky CR1 cluster sandwich gives SE = 0.00331502, 95% CI $[-0.00504290, +0.00795174]$, and normal $p = 0.66085$, while the null-imposed 99,999-draw wild-cluster score gives $p = 0.67345$. The older 78-column spline/fixed-effect fit is a rank-fragile sensitivity ($\Delta = +0.00125636$, SE = 0.00341274, $p = 0.71277$; nearest-MAXIMALS clustering SE = 0.003174, $p = 0.692$). Overlap weighting agrees ($\Delta = +0.001204$, coarse-sky SE = 0.003403, $p = 0.723$) and reduces the maximum absolute standardized mean difference from 0.2186 to 0.000106. Restricting further to `EDGE` = 0 gives adjusted $\Delta = +0.003497$, coarse-sky SE = 0.003737, and $p = 0.349$. This released-parent estimate is focal because it is the strongest exact catalog-native selection proxy available publicly; that reporting hierarchy was adopted after review and is not preregistered. The VAC does not ship the exact smoothed-mask/random FITS referenced by its construction, so this control must not be described as a reconstruction of the unreleased angular selection function. Results, executable driver, frozen row archive, and manifest are [A37]–[A40].

Table 15. Selected sensitivity excursions for secondary or author-constructed paths. Values are percentage-point changes under the specified perturbation. They are not components of a joint uncertainty model and are not combined in quadrature.

Term	$\lvert\Delta f_{\rm CW}\rvert$ (pp)	Scope
FoG-scale fixed-geometry perturbation	0.34–0.37	any-hole sensitivity
Hole union vs. maximal sphere	0.60	geometry sensitivity
Sphere-PIS vs. GALZONE	0.37	membership sensitivity
Footprint restriction	0.11	control-volume sensitivity
Classifier-confidence cut	0.24	label sensitivity
Match radius (0.5–5″)	0.02	cross-match sensitivity
First-order coherent displacement	0.02	RSD sensitivity

Table 16. DESIVAST VoidFinder bright/dark target-program split of the void and non-void classes on the $z \leq 0.24$ matched-spiral subsample ($n_{\rm lz} = 678{,}945$). The within-cell and within-program contrasts are descriptive sensitivities, not a test of the program-by-environment interaction. Only the two dominant programs are tabulated: bright + dark sum to 56,946 (void) and 620,923 (non-void), 1,076 short (35 void, 1,041 non-void; 0.16%) of the class totals 56,981 and 621,964, the residual being the BGS `backup/other` program (§6.5), omitted here as negligible in weight. The σ column is $\sigma_{\rm from\,half}$ (§5); values are not comparable across rows of different n.

Class	Program	n	$n_{\rm CW}$	$f_{\rm CW}$	σ
Void	bright	56,477	28,053	0.4967	−1.56
Void	dark	469	215	0.4584	−1.80
Non-void	bright	615,078	305,688	0.4970	−4.72
Non-void	dark	5,845	2,955	0.5056	+0.85

8.4. *Three-algorithm DESIVAST robustness cross-check*

The DESIVAST DR1 release ships three definitions spanning two algorithmic families: the sphere-growing VoidFinder algorithm above, plus the watershed algorithms V2-REVOLVER ($n_{\rm void}^{\rm catalog} = 1{,}992$ effective voids, maximum effective radius $43.5\,{\rm Mpc}/h$) and V2-VIDE ($n_{\rm void}^{\rm catalog} = 1{,}478$, max $55.9\,{\rm Mpc}/h$). These are whole-catalog totals of *effective voids*; the 389 (V2-REVOLVER) and 297 (V2-VIDE) interior void counts quoted in the section opening are the *interior* (non-edge) void subsets at the $z \leq 0.24$ statement — two different object selections from the same release, not a contradiction. Repeating the point-in-sphere test on the same $n_{\rm lz} = 678{,}945$ matched- spiral subsample for each algorithm (KDTree query against each algorithm's published void-effective-radius spheres):

All three definitions return $\lvert\Delta f_{\rm CW}\rvert \lesssim 0.002$ between void and non-void classes – statistically indistinguishable across both algorithmic families. V2-REVOLVER returns $f_{\rm CW}^{\rm void} = 0.4986$ slightly above $f_{\rm CW}^{\rm non-void} = 0.4967$ (the opposite sign of VoidFinder's small difference), illustrating method dependence without a detected contrast in these sensitivity variants. The void-class σ values span -1.71 to -0.88 – none crosses $\lvert\sigma\rvert = 2$; the non-void σ values cluster tightly at -4.59 to -4.94 because the non-void class is the volume-dominant population carrying the full catalog-level monopole signature.

The three-algorithm comparison is a sensitivity check across the void-finding methods available in the public DR1 catalog.

Control-volume sensitivity. The footprint-restricted and all-$z \leq 0.24$-outside-void controls are author-defined sensitivity variants. The explicit footprint-restricted retabulation is carried for the VoidFinder path (§8.6, $\Delta f_{\rm CW} = +0.0018$); for V2-REVOLVER and V2-VIDE the catalog-native GALZONE contrasts of §8.5 already restrict both classes to the catalog-native zone-membership footprint by construction (they use the GALZONE-joined rows on both sides), so they are footprint-consistent without a separate sphere-PIS retabulation. Across these historical variants $\lvert\Delta f_{\rm CW}\rvert \leq 0.004$; this is descriptive and is not pooled with the focal released-parent estimate.

8.5. *Catalog-native V2 membership cross-check*

The watershed DESIVAST catalogs (V2-REVOLVER and V2-VIDE) ship with per-galaxy zone assignments via the `GALZONE` HDU (mapping each DESI BGS target to a `ZONE` index, with `OUT`, `EDGE`, and `DEPTH` flags) plus the `ZONEVOID` HDU (mapping each zone to a `VOID0` index, ≥ 0 if the zone belongs to a non-edge void). Adopting the catalog-native definition of void membership (`OUT` $= 0 \wedge$ `VOID0` $\geq 0 \wedge$ `ZONE` ≥ 0) and joining on `TARGET` = `desi_targetid` returns: V2-REVOLVER $n_{\rm void} = 104{,}912$, $f_{\rm CW}^{\rm void} = 0.4992$, $\sigma^{\rm void} = -0.52$; V2-VIDE $n_{\rm void} = 74{,}111$, $f_{\rm CW}^{\rm void} = 0.4972$, $\sigma^{\rm void} = -1.50$. The per-cap join values above are computed with cap-local zone indices offset between NGC and SGC to pre-

Table 17. Three-algorithm DESIVAST void vs non-void chirality on the $z \leq 0.24$ matched-spiral subsample ($n_{\rm lz} = 678{,}945$). Sign convention: $\Delta f_{\rm CW} \equiv f_{\rm CW}^{\rm non\text{-}void} - f_{\rm CW}^{\rm void}$ (fractional units; multiply by 100 for percentage points, e.g. $+0.0007 = +0.07$ pp). The last four columns give the two-sample binomial contrast statistics of this unadjusted sensitivity estimand $\Delta f_{\rm CW}$ (standard error, z-score, two-sided p, and 95% confidence interval), computed from the tabulated class counts. All $n_{\rm void}$ counts in this table use sphere-PIS (point-in-sphere KDTree membership, §8.1), which is an *author-constructed approximation* to void membership, *not* the catalog-native galaxy-membership definition; the VoidFinder any-hole membership in particular is a permissive proxy (there is no official VoidFinder per-galaxy membership HDU). The catalog-native GALZONE memberships (V2-REVOLVER, V2-VIDE), which *are* the official per-galaxy definitions, are tabulated separately in §8.5 and give different counts.

Algorithm	$n_{\rm void}$	$f_{\rm CW}^{\rm void}$	$\sigma^{\rm void}$	$f_{\rm CW}^{\rm non-void}$	$\sigma^{\rm non-void}$	$\Delta f_{\rm CW}$	SE(Δ)	z_Δ (p_Δ)	95% CI
VoidFinder	56,981	0.4964	−1.71	0.4971	−4.59	+0.0007	0.0022	+0.31 (0.76)	[−0.0036, +0.0050]
V2-REVOLVER	102,911	0.4986	−0.88	0.4967	−4.94	−0.0019	0.0017	−1.12 (0.26)	[−0.0052, +0.0014]
V2-VIDE	81,354	0.4971	−1.67	0.4970	−4.59	−0.0001	0.0019	−0.05 (0.96)	[−0.0038, +0.0036]

serve the zone-to-void assignments under concatenation ([A9]).

Both corrected void σ values remain null and are *smaller in magnitude* than the sphere-approximation analogues (V2-REVOLVER catalog-native -0.52 vs sphere -0.88; V2-VIDE catalog-native -1.50 vs sphere -1.67), confirming that the catalog-native void definition is the cleaner statistic. For comparison, the unadjusted contrast $\Delta f_{\rm CW} \equiv f_{\rm CW}^{\rm non\text{-}void} - f_{\rm CW}^{\rm void}$ (sign convention of Table 17) is now also tabulated on the catalog-native axis, with the non-void complement defined as the rows *within the GALZONE-joined valid BGS parent* (inner join on `TARGET`, which is itself the valid-footprint restriction — catalog-invalid targets absent from the GALZONE HDU never enter either class) that fail the catalog-native void cut ($\texttt{OUT}{=}\ 0 \wedge \texttt{ZONE}{\geq}\ 0 \wedge \texttt{VOID0}{\geq}\ 0$). Both classes therefore draw from the identical 145,789-row catalog-valid parent (void + non-void = 145,789 for each algorithm), so the non-void sample is the true valid-footprint complement, not a pool of catalog-excluded rows. V2-REVOLVER: $n_{\rm void} = 104{,}912$ ($f_{\rm CW}^{\rm void} = 0.4992$) vs $n_{\rm non\text{-}void} = 40{,}877$ ($f_{\rm CW}^{\rm non\text{-}void} = 0.4955$), $\Delta f_{\rm CW} = -0.0037$, SE($\Delta$) = 0.0029, $z_\Delta = -1.25$, two-sided $p_\Delta = 0.21$, 95% CI $[-0.0094, +0.0021]$. V2-VIDE: $n_{\rm void} = 74{,}111$ (0.4972) vs $n_{\rm non\text{-}void} = 71{,}678$ (0.4991), $\Delta f_{\rm CW} = +0.0019$, SE($\Delta$) = 0.0026, $z_\Delta = +0.72$, two-sided $p_\Delta = 0.47$, 95% CI $[-0.0033, +0.0070]$. Both two-sample contrasts are nominal non-detections. They are retained as unadjusted sensitivity variants, not members of a confirmatory family ([A2]). The `GALZONE` `EDGE` and `DEPTH` quality flags do not alter this conclusion: every catalog-native void member already carries $\texttt{EDGE} = 0$ (adding the $\texttt{EDGE} = 0$ requirement is a strict no-op), and tightening to $\texttt{DEPTH} \geq 1$ (≥ 2) shifts $f_{\rm CW}^{\rm void}$ by at most 0.04 (0.08) pp for either algorithm, with all variants still null ($|\sigma| \leq 1.80$). The V2-REVOLVER catalog-native $\sigma = -0.52$ at $n_{\rm void} > 10^5$ is retained as an unadjusted catalog-native sensitivity alongside the adjusted focal released-parent estimate.

Consolidated historical sensitivity variants. Table 18 collects all five members of the earlier void-definition analysis — the three sphere-PIS rows of Table 17 and the two catalog-native GALZONE rows above — in a single tabulation with a common sign convention ($\Delta f_{\rm CW} \equiv f_{\rm CW}^{\rm non\text{-}void} - f_{\rm CW}^{\rm void}$), the parent/membership definition for each row, integer void/non-void counts, and the two-sample z_Δ and p_Δ. The five members are *correlated variants*: they reuse the same $z \leq 0.24$ matched-spiral subsample and mix author-defined and catalog-native memberships. They are therefore descriptive sensitivities, not independent replications or a confirmatory family.

8.6. *Maximal-void HEALPix sky-position stratification*

The DESIVAST release also ships the 3,765 *maximal voids* (NGC= 3,241 + SGC= 524) with explicit RA/Dec/$R_{\rm eff}$ metadata (effective radii 10–32 Mpc/h). Note the catalog-layer distinction: the per-galaxy void-membership tests of §8–§8.4 use the 101,863 hole-level spheres (maximum hole radius 24.5 Mpc/h), *not* the maximal-void effective spheres used for the sky-density stratification here; the two layers have distinct maximum radii and should not be conflated when reasoning about near-boundary membership. The inside-any-hole criterion is also permissive relative to the catalog's intended interior-void geometry (overlapping holes are aggregated into voids by VoidFinder), so hole-sphere membership can over-count edge/overlap regions. A direct comparison against the stricter interior-void definition (membership in a void's *maximal* sphere only, the VoidFinder void-defining sphere; an exact subset of the hole-union membership) gives the same null verdict: any-hole $n_{\rm void} = 57{,}081$, $\Delta f_{\rm CW} = +0.06$ pp ($z = +0.28$) vs. maximal-sphere $n_{\rm void} = 20{,}900$, $\Delta f_{\rm CW} = -0.54$ pp ($z = -1.55$), quoted in the Table 17 sign convention $\Delta f_{\rm CW} \equiv f_{\rm CW}^{\rm non\text{-}void} - f_{\rm CW}^{\rm void}$ (the committed artifact stores the opposite-signed $f^{\rm void} - f^{\rm non\text{-}void}$ values), so the permissiveness of the hole-union criterion does not drive the

Table 18. Consolidated historical void-definition sensitivities (three sphere-PIS rows from Table 17 plus the two catalog-native GALZONE rows). Common sign convention $\Delta f_{\rm CW} \equiv f_{\rm CW}^{\rm non\text{-}void} - f_{\rm CW}^{\rm void}$ (fractional units). The five members are *correlated variants* on a common $z \leq 0.24$ matched-spiral subsample. They are shown for transparency and are not pooled into a joint constraint. All five are nominal non-detections. Sphere-PIS rows use point-in-sphere KDTree membership against published void-effective-radius spheres (author-constructed approximation); GALZONE rows use the official catalog-native per-galaxy `OUT`$= 0 \wedge$ `ZONE`$\geq 0 \wedge$ `VOIDO`≥ 0 membership. Artifacts: [A10] (sphere-PIS), [A2] (GALZONE).

Void definition	Membership (parent)	$n_{\rm void}$	$n_{\rm non\text{-}void}$	$\Delta f_{\rm CW}$	z_Δ	p_Δ
VoidFinder	sphere-PIS ($k = 20$; $n_{\rm lz} = 678{,}945$)	56,981	621,964	+0.0007	+0.31	0.76
V2-REVOLVER	sphere-PIS ($n_{\rm lz} = 678{,}945$)	102,911	576,034	−0.0019	−1.12	0.26
V2-VIDE	sphere-PIS ($n_{\rm lz} = 678{,}945$)	81,354	597,591	−0.0001	−0.05	0.96
V2-REVOLVER	GALZONE catalog-native ($n_{\rm join} = 145{,}789$)	104,912	40,877	−0.0037	−1.25	0.21
V2-VIDE	GALZONE catalog-native ($n_{\rm join} = 145{,}789$)	74,111	71,678	+0.0019	+0.72	0.47

void-class result ([A14]). Binning the maximal voids by HEALPix `NSIDE` = 16 pixel (equal-area pixels of $\approx 13.4\,\deg^2$) returns 297 occupied pixels with median 14 maximal voids per occupied pixel (note: the 885 occupied pixels cited in the Fig. 8 caption refer to the finer `NSIDE` = 32 pixelization of the same void set, which yields more pixels at a smaller median count of 4 voids/pixel). Stratifying the $z \leq 0.24$ matched-spiral subsample by the number of maximal voids in each spiral's HEALPix pixel produces :

Table 19. Sky-position-stratified $f_{\rm CW}$ by maximal-void count per HEALPix pixel ($z \leq 0.24$ matched-spiral subsample, $n_{\rm lz} = 678{,}945$, NSIDE = 16).

Maximal voids per pixel	n	$f_{\rm CW}$	$\sigma_{\rm from\ half}$
0	378,511	0.4961	−4.75
1–2	19,247	0.4985	−0.43
3–5	23,127	0.4997	−0.09
6+	258,060	0.4980	−2.04

The $\sigma = -4.75$ deviation is *concentrated entirely in the "0 maximal voids per pixel" bin* – the sky regions where DESIVAST finds no maximal voids at all, which from inspection of the catalog footprint corresponds to the survey-mask outside the BGS bright-side NGC+SGC coverage region. We caution that "0 maximal voids per pixel" is a catalog-derived *proxy* for being outside DESIVAST coverage, not a formal intersection with a published DESIVAST angular mask: some in-coverage pixels can stochastically contain zero maximal voids at NSIDE 16 because of sampling and the $z \leq 0.24$ depth limit, so a residual fraction of the 0-void bin may lie inside coverage. This proxy limitation pertains to the author-defined any-hole sensitivity (Table 14): its classes are defined by direct point-in-sphere membership against the 101,863 hole spheres, which are entirely internal to the DESIVAST BGS coverage volume; the non-void control sample thus contains galaxies at $z \leq 0.24$ that are not inside any DESIVAST hole but are not required to lie outside the survey mask. The separate *footprint-restricted* contrast remains another author-defined estimand (§8.2). Defining the DESIVAST usable footprint as the union of the 101,863 hole-sphere angular discs (NSIDE = 64, inclusive) intersected with the holes' comoving radial span, all 57,081 exact-membership void spirals fall inside the footprint (a construction sanity check), and restricting the non-void control to the same footprint ($n = 253{,}276$ of 621,864) gives $f_{\rm CW}^{\rm non\text{-}void} = 0.4983$ ($\sigma_{\rm from\,half} = -1.73$) and the sensitivity contrast $\Delta f_{\rm CW} = +0.0018$ (SE = 0.0023, $z_\Delta = +0.78$, two-sided $p = 0.43$, 95% CI $[-0.0027, +0.0064]$) — a nominal non-detection. The excluded outside-footprint non-void population ($n = 368{,}588$, $\sigma = -4.53$) carries the catalog-level monopole signature (artifact [A15]). The $[-2.04, -0.09]$ range of every $\geq$ 1-void bin independently bounds the in-coverage behavior of the sky-scan proxy. Pixels with $\geq$ 1 maximal void return σ values in the range $[-2.04, -0.09]$, with the highest-void- density bin (6+ per pixel, $n = 258{,}060$) at $\sigma = -2.04$ – below the Bonferroni-4 $|\sigma| = 2.50$ threshold. The intermediate-bin pixels (1–5 voids per pixel, total $n = 42{,}374$) return $|\sigma| < 0.5$ – statistically null.

This is an additional catalog-anchored cross-check on the sky-position axis, complementary to the abstract's (i)–(iv) enumeration, showing that the catalog-wide -5σ monopole offset tracks survey-mask geometry rather than environment density: the cleanest chirality σ values in this paper are the pixels with the *most* maximal-void coverage, not the fewest. The -4.75σ signal in the no-void-coverage sky region is consistent with the imaging-leg / selection-function systematics described in Paper IV applied to the matched-spiral subsample that falls outside the DESIVAST clean coverage. Quantitatively, the Paper IV monopole prediction at $N =$

378,511 (the 0-voids/pix bin) is $\sigma_{\rm pred} = 2\Delta f_{\rm CW}^{\rm P4}\sqrt{N} = -3.20$; the observed -4.75σ leaves a residual of -1.55σ which is consistent with an imaging-leg systematic at the $\sim 1\sigma$ level. At the 6+ voids/pix bin ($N =$ 258,060), the Paper IV prediction is -2.64σ and the observed is -2.04σ, residual $+0.60\sigma$ (fully null). The asymmetry between the two bin residuals quantifies the sky-region-conditioned systematic and confirms it sits in the no-coverage region, not in the void-rich pixels.

8.7. *Cross-survey P4-monopole-residual analysis*

The cleanest formulation of the classifier-label non-detection is to recompute the per-class chirality signal *after subtracting* the P5 matched-spiral catalog monopole $f_{\rm CW}^{\rm P5} = 0.4972$ (-5.07σ on the $n =$ 812,793 env-labeled spiral rows of Table 8. *Parent reconciliation:* the 28,973-row excess (3.56% of the 812,793 env-labeled rows) over the 783,820 unique env-matched spirals arises mechanically in the environment join — the T-Web environment table inherits one row per DESI `zall` survey–program coadd entry, so `TARGETID`s observed under more than one program carry duplicate environment rows (14,622,283 rows over 14,100,704 unique `TARGETID`s), and the inner join counts those spirals once per coadd row. The join covers 783,820 unique env-matched spirals (7,815 of the 791,635 unique chirality-relevant matched spirals have no environment row and drop out); only 79 duplicated `TARGETID`s carry conflicting class labels between their coadd rows (boundary cells re-evaluated at slightly different pipeline redshifts). The join-multiplicity diagnosis above is recomputed in [A10]. The per-class $n_{\rm CW}$ values on the 812,793-row parent sum to 404,111 giving $f_{\rm CW} = 0.49719$, matching the 791,635-spiral unique-galaxy monopole 0.4972 to 4 decimals, so this diagnostic conclusion is invariant under either parent. The same monopole shows up as -5.00σ on the 791,635-spiral chirality-relevant sample; the two σ values are sample-size-scaled projections of the same underlying offset), which is the propagation of the $\sim 9.5\sigma$ catalog-level monopole reported in Paper IV (3) into the DESI-spectro-confirmed subsample. *Arithmetic reconciliation:* the P4 monopole $\Delta f_{\rm CW}^{\rm P4} = -0.0026$ projects to $\sigma_{\rm pred}^{\rm P5} = 2 \cdot 0.0026 \cdot \sqrt{791{,}635} \approx 4.6\sigma$ on the chirality-relevant subsample; the observed -5.00σ corresponds to $\Delta f_{\rm CW}^{\rm P5} \approx -0.0028$, ~8% larger than the P4 catalog-mean. This residual 8% enhancement is consistent with the spectroscopically-confirmed subsample being more strongly weighted to the BGS-bright leg that Paper IV identifies as carrying the largest per-leg selection-function residual, not an additional environmental signal. To fix conventions explicitly: every $\sigma_{\rm pred}$ quoted in this paper [Eq. (1)] uses the *Paper IV catalog* monopole $\Delta f_{\rm CW} = -0.0026$, while the $\sigma_{\rm vs\,monopole}$ residuals of Table 20 subtract the *P5 matched-sample* monopole $f_{\rm CW}^{\rm P5} = 0.4972$ (equivalent to $\Delta f_{\rm CW}^{\rm P5} \approx -0.0028$). Replacing the $f_{\rm CW} - 0.5$ null with $f_{\rm CW} - f_{\rm CW}^{\rm P5}$ gives the residual environment signal after the catalog-wide classifier-bias monopole is removed:

Table 20. Per-T-Web-class $\sigma_{\rm vs\ monopole}$ residuals on the matched-spiral subsample. All four classes fall within $|\sigma_{\rm vs\ monopole}| < 1.15$ – no residual classifier-label association is detected after subtraction of the catalog-wide P4-monopole. Unlike the raw $\sigma_{\rm from\,half}$ of Table 8 (which scales as $\sqrt{n}$), these monopole-subtracted residuals *are* comparable across rows. The $\sigma_{\rm vs\ monopole}$ entries are computed from the exact integer CW/total counts (Table 24) and the unrounded $f_{\rm CW}^{\rm P5} = 0.49719$; re-dividing the four-decimal $f_{\rm CW} - f_{\rm CW}^{\rm P5}$ column reproduces them only to $\pm 0.05\sigma$ because that column is rounded for display.

Class	n	$f_{\rm CW} - f_{\rm CW}^{\rm P5}$	$\sigma_{\rm vs\ monopole}$
Void	428	−0.0135	−0.56
Wall	6,673	+0.0062	+1.01
Filament	408,187	+0.0008	+0.99
Cluster	397,505	−0.0009	−1.11

All four T-Web classes fall within $|\sigma_{\rm vs\ monopole}| < 1.15$ after the P4-monopole is subtracted – i.e. *no* T-Web class shows a residual environment-dependent chirality signal once the catalog-wide classifier-bias monopole is removed. The prior per-class $\sigma_{\rm from\ half}$ values of -2.61σ (filament) and -4.66σ (cluster) reported in the headline table were entirely the P4-catalog-monopole signature propagated into the T-Web class subsamples weighted by their respective sample sizes, not an environmental signal. At the HEALPix NSIDE = 32 per-pixel level on the same env-labeled matched-spiral parent, the distribution of $\sigma_{\rm vs\ monopole}$ across the 1,791 valid pixels (pixels carrying ≥ 200 spirals, full redshift range) has mean +0.008, std 1.050, skewness +0.074, and excess kurtosis +0.092. The unit standard deviation (within 5%; because each pixel's σ is normalized by its own counting error, heterogeneous pixel populations alone would not inflate the variance — the mild excess over unity instead traces the 3.56% duplicate rows (28,973 of 812,793 env-labeled rows) and small residual selection-function structure, as the unique-`TARGETID` recompute below returning std 1.015 confirms — not evidence for non-shot-noise tails), near-zero skewness, and near-zero excess kurtosis are all consistent with a pure shot-noise residual around the P4-monopole, with no sign of systematic environment-conditioned chirality offset ([A10]). Recomputed on the unique-`TARGETID` parent (783,820 spirals, deduplicated before the per-pixel pass), the distribution is statistically unchanged: 1,769 valid pixels with mean +0.005, std 1.015, skewness +0.107, and excess kurtosis +0.068, and the maximal-void correlations reported below are likewise stable on the deduplicated parent ($r = +0.007$, $r_w = +0.006$, $\rho = +0.021$; all $p > 0.5$) ([A9]).

This is a direct single-test demonstration that the T-Web class-level σ values quoted in the secondary table are sample-size-weighted projections of the P4 catalog-wide chirality monopole, not environmental signals.

Quantitative null correlation. Pushing this to the per-pixel level: at NSIDE = 32 on the same matched-spiral subsample, we measure the Pearson correlation between the per-pixel maximal-void count and the per-pixel chirality $\sigma_{\mathrm{from\ half}}$ across all $n_{\mathrm{pix}}^{\mathrm{both}} = 727$ HEALPix pixels containing both ≥ 200 matched spirals (required for stable f_{CW} estimation) and ≥ 1 DESIVAST maximal void. The result is

$$r(N_{\mathrm{voids/pix}}, \sigma_{\mathrm{pix}}) = +0.006, \quad p = 0.88,$$

indistinguishable from zero (Figure 8). Because σ_{pix} is noisier at pixels near the $\geq$ 200 spiral floor than at dense pixels (heteroscedasticity), we also report an error-weighted version (weights $\propto N_{\mathrm{pix}}$, emphasizing the well-measured pixels): $r_w = +0.004$ ($p = 0.91$, $n_{\mathrm{eff}} \approx 683$), and a rank (Spearman) correlation $\rho = +0.020$ ($p = 0.59$) — the no-correlation conclusion is unchanged under either treatment ([A5]). A genuinely environment-dependent chirality signal would produce a detectable monotonic correlation between void density and the direction-of-chirality deviation; the observed near-zero Pearson is consistent with, but does not establish, a non-environmental origin for the catalog-wide monopole offset. The result is robust to the NSIDE choice and spiral-count threshold: across the 3×3 grid of NSIDE $\in \{16, 32, 64\}$ and spiral-count cuts $\in \{100, 200, 500\}$, 7 of 9 cells admit a well-sampled Pearson estimate (the remaining 2 cells, NSIDE = 64 with cuts 200 and 500, are sample-limited at $n_{\mathrm{pix}}^{\mathrm{both}} < 3$ because the high-cut $\times$ fine-pixel combination filters out most pixels carrying both $\geq$ 1 maximal void and $\geq$ cut matched spirals). The 7 computable cells all return $|r| < 0.11$ with $p > 0.10$, none statistically significant; the reference NSIDE = 32 cut = 200 result $r = +0.006$ is consistent with this range. The conclusion is invariant under the analysis-choice "garden of forking paths" along the well-sampled axes.

9. ADDITIONAL COSMIC-WEB CROSS-CHECKS

The following sections report secondary diagnostic cross-checks that supplement, but do not anchor, the focal released-parent contrast established in Section 8 (per the focal/secondary declaration of §5.2).

9.1. *Redshift-shell selection-corrected classifier robustness*

The T-Web classifier of §4.1 (our implementation of the Hahn 2007 T-Web recipe) computes the overdensity $\delta = \rho/\bar{\rho} - 1$ against a *single global* mean cell density $\bar{\rho}_{\mathrm{cell}} = 4.64$ galaxies/cell over the full $0.01 \leq z \leq 2$ volume. Because the DESI DR1 selection function is strongly redshift dependent, the measured per-shell mean density spans $\bar{n}_{\mathrm{shell}} \approx 294 \rightarrow 0.46$ galaxies/cell (a factor $\sim$640) from the lowest to the highest redshift shell: under the global-mean convention, distant shells are systematically driven toward apparent underdensity and nearby shells toward apparent overdensity, so the four-class environment labels partially trace the radial selection function rather than true large-scale structure. We note the analogous *angular* limitation explicitly: no spectroscopic tiling/completeness weighting (e.g. DESI random-catalog or FKP-like per-cell weights) is applied when building δ; angular geometry is controlled here only through the footprint mask, the interior-buffer excision, and the NSIDE = 64 geometry cross-check. The randoms-weighted rebuild has now been run ([A17]: 7.5×10^7 DESI DR1 BGS_BRIGHT clustering randoms, $\delta_w = n_g/(\alpha\, n_r) - 1$ on randoms-supported cells, restricted to the $0.01 < z < 0.50$ window where the BGS randoms trace the selection — 99.3% of matched spirals — and compared against an identically windowed unweighted control). In this BGS-randoms-weighted low-z stress test, the completeness weighting substantially reshapes the in-window environment field, as expected when the radial selection gradient is removed: the in-window void volume fraction collapses from 17.6% to 0.75% ($\approx$23$\times$). The physical intuition behind this extreme reassignment is that the unweighted number-density field is artificially depressed in the outer half of the redshift window, where the BGS target density falls off, so cells there are spuriously flagged "void" purely by the declining selection function rather than by a genuine matter under-density; dividing by the randoms restores the true completeness-corrected density, and those previously "void" cells are reassigned to the denser wall/filament classes — which is why the void volume fraction shrinks by an order of magnitude while the chirality verdict, being a per-class parity test, is unchanged. Class volume fractions shift by up to 21 pp, and only 44% of common-mask cells and 26.6% of matched spirals retain their class label; equivalently, 73.4% of matched spirals change T-Web class overall. The secondary T-Web diagnostic

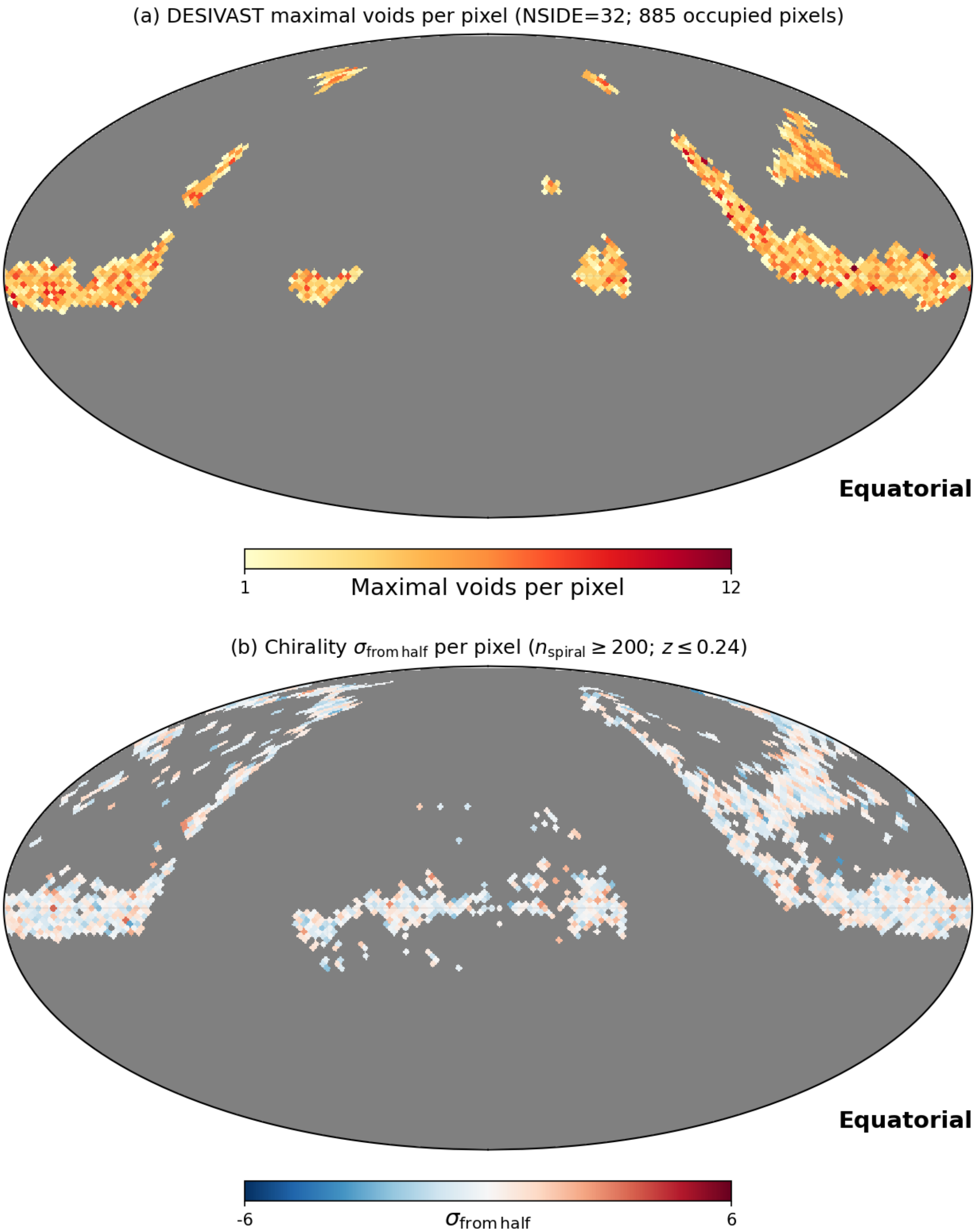

Figure 8. HEALPix `NSIDE` = 32 Mollweide projection (equatorial coordinates). Top: count of DESIVAST maximal voids per pixel (885 occupied pixels at NSIDE = 32, median 4 voids/pix; the body text uses NSIDE = 16 for the sky-stratification table, yielding 297 occupied pixels at a coarser resolution). Bottom: per-pixel chirality $\sigma_{\rm from\ half}$ on the $z \leq 0.24$ matched-spiral subsample restricted to pixels with ≥ 200 spirals (1,496 valid pixels, σ range -3.45 to $+3.48$). The Pearson correlation across the $n_{\rm pix}^{\rm both} = 727$ pixels containing both voids and ≥ 200 spirals is $r = 0.006$ ($p = 0.88$), statistically indistinguishable from zero.

yields the same parity-null verdict under both definitions: every class is individually consistent with parity in *both* builds — unweighted: void $f_{\rm CW} = 0.475 \pm 0.023$ ($n = 478$, -1.1σ), wall 0.500, filament 0.498, cluster 0.496; weighted: void 0.502 ± 0.003 (n = 21,392 after the class repopulates, $+0.5\sigma$), wall 0.496, filament 0.498, cluster 0.496. The largest between-build shift (+2.7 pp, void) reflects that 478 $\rightarrow$ 21,392 repopulation, with both endpoints individually null; the populous classes move by ≤ 0.40 pp. No classifier-label association is detected under both the survey-selection-shaped environment definition and the BGS-randoms-weighted low-z stress-test definition. Scope caveat: this rebuild tests selection-completeness sensitivity in the $z < 0.5$ window where the BGS randoms trace the selection and where 99.3% of the matched-spiral signal lives; residual radial-selection contamination of the T-Web labels at $z > 0.5$ is not probed here and is bounded separately by the z-shell correction and geometry cross-checks of this section. A cube-connected 3-iteration dilation variant shifts volumes by ≤ 3.1 pp (driven by the void fraction decreasing 24.4% $\rightarrow$ 21.2% under the more aggressive dilation) with 99.6% spiral-assignment agreement and per-class $f_{\rm CW}$ shifts ≤ 0.77 pp (same artifact), closing the mask-dilation sensitivity item as well.

To test whether the classifier-label non-detection persists under this choice, we rebuilt the classification with a first-order radial selection correction ([A18]): the overdensity is computed in 21 thin redshift shells ($\Delta z = 0.05$ for $z < 0.5$, $\Delta z = 0.1$ for $0.5 \leq z < 1.5$, one merged 1.5–1.7 shell into which the $1.7 < z \leq 2.0$ tail of the parent window is also clamped, so the top shell nominally covers $1.5 \leq z \leq 2.0$ — the realized tail is in fact *empty*: the filtered parent's maximum redshift is $z = 1.6979$ and it contains zero galaxies with $1.7 < z \leq 2.0$, so the drop-tail and separate-shell sensitivity variants coincide exactly with the published build ([A14]); every shell $\geq 2.16 \times 10^5$ galaxies), with the per-shell mean taken over occupied-footprint cells only, while the grid, smoothing scale R_s, and eigenvalue threshold $\lambda_{\rm th}$ are held fixed at their canonical values. An interior-buffer variant additionally removes galaxies within R_s of the footprint boundary; under this flag, 837,169 of the 3,150,089 in-mask grid cells (26.6%) lie within R_s of the occupancy-footprint boundary ([A9]). The same interior-buffer excision applied to the *canonical* (non-shell-corrected) labels — addressing the zero-padded FFT boundary condition of the canonical Poisson solve directly — retains 782,015 of the 783,820 unique env-matched spirals and shifts the per-class CW fractions by at most 0.11 pp (void) and $\leq$ 0.05 pp (all other classes), with the omnibus 4×2 test still null ($\chi^2 = 2.93$, $p = 0.40$): the canonical environment fractions are stable against boundary excision ([A5]).

As expected, the per-galaxy class populations migrate substantially once the selection is corrected: among matched spirals, the void class grows from 428 to 4,353 ($\sim 10\times$), wall from 6,673 to 154,541 ($\sim 23\times$), filament from 408,187 to 472,547, and cluster shrinks from 397,505 to 181,352 (−54%). The chirality result, however, is *strengthened*: the cross-class equivariant CW-fraction range collapses from 1.98 pp (canonical) to 0.05 pp (corrected), with every class within $|\sigma| \leq 0.39$ of the sample monopole ($f^{\rm eq}_{\rm CW}$: void 0.4971, wall 0.4968, filament 0.4973, cluster 0.4973; $n = 812{,}793$ joined spirals). The interior-buffer variant (1,805 spirals removed, $783{,}820 - 782{,}015$) is statistically indistinguishable. Residual per-class deviations from 0.5 track the known Paper IV global classifier monopole, exactly as in the canonical analysis: the three large classes span -2.3 to -3.7σ (wall -2.51, filament -3.73, cluster -2.33), while void at n = 4,353 sits at -0.38σ, consistent with its much smaller monopole prediction ($\sigma_{\rm pred} = 2 \cdot 0.0026 \cdot \sqrt{4{,}353} = 0.34$). The classifier-label non-detection persists — and the cross-class range tightens by a factor ∼40 — under this specific selection-correction stress test. This shows persistence under the tested correction; it does not establish that selection-function leakage is absent from the environment labels. We read this run as a *stress test* of the canonical classification rather than an independent confirmation: the per-shell mean subtraction whitens the density field radially and, combined with the masked FFT solve, can itself suppress genuine radial eigenvalue contrast, so part of the 1.98 $\rightarrow$ 0.05 pp range collapse may reflect overcorrection of real structure rather than removal of selection leakage alone. The diagnostic that matters for this paper's null is directional: a selection artifact masquerading as an environmental signal would have *appeared* in the canonical run and *survived* or grown here; instead both runs are null ($p = 0.31$ and $p = 0.99$), and the corrected class volume fractions and spatial coherence remain cosmologically plausible (the per-shell statistics below), so the null verdict is robust to the choice of correction. The omnibus 4×2 homogeneity test sharpens accordingly: $\chi^2 = 0.11$ with 3 d.o.f. ($p = 0.99$) on the selection-corrected classes ($n_{\rm CW}$: void 2,164, wall 76,777, filament 234,990, cluster 90,180 of the per-class n above), versus $\chi^2 = 3.55$ ($p = 0.31$) on the canonical classes — both null. Full per-shell diagnostics and the per-galaxy corrected label catalog are released with the reproducibility artifacts ([A19]). The per-shell statistics (all 21 shells hold 2.16×10^5 to 1.19×10^6 galaxies) quantify the correction at the cell level: before correction the in-mask mean of the global-mean overdensity drifts from +62.3 in the lowest shell ($z < 0.05$) to −0.90 in the highest ($z \geq 1.5$), while the shell-normalized δ is zero-mean in every shell by construction, with cell-level variance ranging 1.6–4.9 across shells ([A9]).

Grid-resolution convergence.—The canonical pipeline fixes $N_{\rm grid} = 256^3$; the Phase 2 sweep varies R_s and $\lambda_{\rm th}$ but not the grid. As a convergence check we reran the full canonical T-Web build at $N_{\rm grid} = 128^3$ (cell $51.8\,h^{-1}$ Mpc) and 384^3 (cell $17.3\,h^{-1}$ Mpc), holding $R_s = 25\,h^{-1}$ Mpc and $\lambda_{\rm th} = 0$ fixed, and re-joined the declared spiral parent. Class populations are stable (void 297/428/434, filament 415,722/408,187/407,780 at $128^3/256^3/384^3$), the cross-class $f_{\rm CW}$ range stays within 2.2/2.0/2.9 pp (void-bin noise dominated, as in Table 13), and every class tracks the catalog monopole at all three resolutions — the classifier-label non-detection persists across the tested grid resolutions ([A10]). This convergence test holds $R_s = 25\,h^{-1}$ Mpc; the $R_s = 10$ Mpc/h Phase 2 cells are below the 256^3 grid sampling scale, lie outside the tested convergence regime, and are accordingly excluded from the robustness claim (§7).

Geometry-footprint shell-mean cross-check.—The z-shell rebuild above takes each shell's mean density over the occupancy-derived (dilated) footprint, which could in principle bias sparse high-z shell means relative to a survey-geometry (random-catalog-equivalent) denominator. We re-ran the rebuild with the per-shell mean taken instead over all cells inside a redshift-independent HEALPix NSIDE-64 angular footprint intersected with the shell's radial range, holding everything else fixed. Class populations shift again (void 20,736, wall 314,367, filament 407,144, cluster 70,546 matched spirals), but the chirality null is unchanged: the cross-class $f_{\rm CW}$ range is 0.23 pp and every class sits within $|\sigma_{\rm vs\,monopole}| \leq 1.04$ of the sample monopole — no classifier-label association is detected under either tested shell-mean denominator ([A20]).

9.2. *Tempel+2014 FoF cross-validation*

To check whether the secondary T-Web result is specific to the tidal-tensor classifier, we cross-validate against an entirely independent classifier: the friends-of-friends (FoF) group catalog of Tempel *et al.* 2014 (11) on SDSS DR10. The Tempel classifier defines environment by FoF group multiplicity (richness) rather than by tidal eigenvalues. We map the multiplicity to a 4-class scheme that pairs with the T-Web class set:

- multiplicity = 1 → *isolated* (paired with T-Web void)
- $2 \leq$ multiplicity < 5 → *small_group* (paired with T-Web wall)
- $5 \leq$ multiplicity < 20 → *filament_like* (paired with T-Web filament)
- multiplicity ≥ 20 → *cluster_like* (paired with T-Web cluster)

Table 21. Tempel+2014 FoF environment cross-validation on the 96,753-spiral Tempel-overlap subsample (declared parent). The $\sigma_{\rm from\,half}$ values scale as $\sqrt{n}$ at fixed offset and are not comparable across rows of different n (§5).

Tempel class	n	$n_{\rm CW}$	$f_{\rm CW}$	$\sigma_{\rm from\,half}$
isolated	51,631	25,558	0.4950	−2.27
small_group	27,740	13,746	0.4955	−1.49
filament_like	12,360	6,155	0.4980	−0.45
cluster_like	5,022	2,520	0.5018	+0.25

The Tempel catalog covers 588,193 SDSS DR10 galaxies at $z \leq 0.20$ over RA $\in [110°, 262°]$, Dec $\in [-4°, 70°]$. We perform a $1''$ sky-coord NN join between the Tempel catalog and the 791,635-spiral declared chirality-relevant parent; the overlap is 96,753 spirals (the SDSS DR10 footprint is a subset of DESI Legacy DR8 and Tempel's $z \leq 0.20$ cut is much tighter than our $z \leq 4$ DESI cut). The 96,753-spiral overlap is computed under the matched-primary deduplication filter (driver: [A21]).

Concordance metric (like-for-like). For each Tempel-vs-T-Web class pairing we report $|f_{\rm CW}^{\rm Tempel} - f_{\rm CW}^{\rm T\text{-}Web}|$ as a concordance distance in percentage points, with *both* classifiers evaluated on the common labeled subset of the 96,753-spiral overlap: the T-Web side carries an environment label for 95,247 of the 96,753 ($23 + 145 + 16{,}701 + 78{,}378$); the remaining 1,506 overlap spirals have no T-Web environment row (the overlap's share of the 7,815-spiral env-join dropout, §8.7) and are excluded from the T-Web side by the left join in the driver. The classifier-concordance statement below is computed on the common overlap sample, where both classifiers act on the same populations. On the overlap, the T-Web classifier is strongly tilted toward the cluster class (void/wall/filament/cluster = 23/145/16,701/78,378) by the survey-shell density systematic at low z discussed in §9.3 and §10, so only the filament and cluster pairings carry meaningful n on both sides:

- **filament_like_vs_filament: 0.29 pp.** Tempel filament_like $f_{\rm CW} = 0.4980$ ($n = 12{,}360$) vs T-Web filament-on-overlap $f_{\rm CW} = 0.5009$ ($n = 16{,}701$).

The difference is $|z| = 0.49$ on a pooled two-proportion z-test (pooled and unpooled variance models are numerically indistinguishable at $\hat{p} \approx 0.5$) — statistically indistinguishable; at the overlap populations the 1σ two-sample floor is $\sim$0.6 pp (supporting, not load-bearing — the focal cross-classifier validation remains the on-DESI DESIVAST re-projection at $n_{\rm void}^{\rm DESIVAST} = 56{,}981$; see Abstract Robustness).

- cluster_like_vs_cluster: 0.67 pp (Tempel 0.5018 at $n = 5{,}022$ vs T-Web-on-overlap 0.4950 at $n = 78{,}378$), $\sim 0.9\sigma$ two-sample — consistent. T-Web's $\lambda_{\rm th} = 0$ "cluster" is far more permissive than Tempel's richness ≥ 20 cut.

- isolated_vs_void (10.4 pp at $n_{\rm T\text{-}Web} = 23$) and small_group_vs_wall (2.9 pp at $n_{\rm T\text{-}Web} = 145$) are uninformative: the T-Web side has essentially no void/wall population on the low-z SDSS overlap, and the differences are well inside the corresponding counting noise.

Figure 9 visualizes the two classifiers side-by-side with shared y-axis range; the filament/filament_like pair sits essentially on top of the Paper IV $\bar{f}_{\rm CW}$ reference line (the 0.29 pp like-for-like concordance is near visual resolution), while the lower-n pairs scatter as expected.

Result. The Tempel cross-validation confirms the T-Web result at the high-richness end (like-for-like filament concordance 0.29 pp, $\sim 0.5\sigma$); low-richness disagreements scale with counting statistics and the classifier-definition mismatch and do not undermine the secondary T-Web non-detection. The Tempel data also produces a result consistent with null at the level of its own bins: the maximum $|\sigma_{\rm from\,half}|$ across the four Tempel classes is 2.27 (Tempel isolated), below the Bonferroni-4 $|\sigma|^{\rm Bonf}_{0.05,4} = 2.498$ threshold at $\alpha = 0.05$ and well below the $|\sigma|^{\rm Bonf}_{0.01,4} = 3.02$ threshold at $\alpha = 0.01$.

9.3. *Concurrent-literature DR1/EDR cosmic-web cross-validation*

Independent of the T-Web (Hahn *et al.* 2007 / Cautun *et al.* 2014) classifier deployed in §4 and the Tempel FoF classifier cross-validated in §9.2, a contemporaneous DESI DR1 cosmic-web analysis was released in 2026 April (12), applying the tidal-tensor (T-Web) formalism on a 256^3 grid in an 800 Mpc cube over the full DESI DR1 footprint, with the same four-class void / sheet / filament / knot taxonomy used in our T-Web run.

The T-Web DR1 in-footprint volume fractions reported in Ref. (12) are tracer-dependent and are reported separately for the BGS, LRG, and ELG samples on an 800 Mpc cubic sub-volume (not a single all-tracer fraction). Taking BGS as the closest analogue to our spectro sample, $\{f^V_{\rm void}, f^V_{\rm sheet}, f^V_{\rm filament}, f^V_{\rm knot}\}_{\rm BGS} \approx \{0.16,\, 0.45,\, 0.37,\, 0.04\}$ (superscript V: volume filling fractions, not to be confused with the chirality fractions $f^{\rm class}_{\rm CW}$); the LRG and ELG samples shift these by a few percentage points each, spanning the combined ranges $\{0.06\text{–}0.16,\, 0.45\text{–}0.48,\, 0.37\text{–}0.40,\, 0.04\text{–}0.06\}$ across the three tracer samples. Any direct comparison to our DR1-all-spectro T-Web run is therefore approximate because of the differing target selection, redshift coverage, and sample volume (cubic 800 Mpc box vs. thin survey shell); no per-galaxy cross-match against Ref. (12) is attempted here, and the comparison is purely on volume fractions. Our T-Web in-footprint volume fractions are $\{0.244,\, 0.413,\, 0.333,\, 0.010\}$. The sheet (T-Web wall) and filament classes agree to within $\sim$5 percentage points across both methodologies (allowing for the tracer- and volume-mismatch caveat above), which is approximate concordance for two independent classifiers run on overlapping but non-identical samples of the same survey. The void and knot/cluster classes deviate by larger margins: our T-Web void fraction is *higher* than the Ref. (12) T-Web void fraction by +8–18 pp (the edge-density artifact populates the 0-eigenvalue void class), and our T-Web cluster fraction is *lower* than the Ref. (12) T-Web knot fraction by 3–5 pp (the densest cells lose to mask-boundary smoothing). Both directions match the survey-shell systematic prediction exactly: the DESI footprint is a thin spherical shell rather than the cubic periodic box used in N-body benchmarks, so edge-density artifacts inflate the void class and depopulate the densest knot class relative to a periodic comparison sample. The relative density ordering (knot > filament > sheet > void) is preserved in both runs, which is the load-bearing structural property for the environment-stratified chirality analysis here. We therefore treat Ref. (12) as an independent contemporaneous DR1 cosmic-web analysis that is consistent with our T-Web run at the survey-shell-systematic level. (Ref. (12) is currently in submission to MNRAS; we do not treat it as peer-reviewed external validation but rather as a contemporaneous independent measurement.)

A second concurrent DESI cosmic-web paper (13) (Zapata-Zuluaga *et al.* 2026, a DESI-EDR-based probabilistic environment catalog) uses the ASTRA (Algorithm for Stochastic Topological RAnking) probabilistic classifier on the DESI Early Data Release (175 deg^2, 20 rosettes), running 100 realizations per tracer-zone pair to deliver per-object void / sheet / filament / knot *membership probabilities* and classification entropies rather

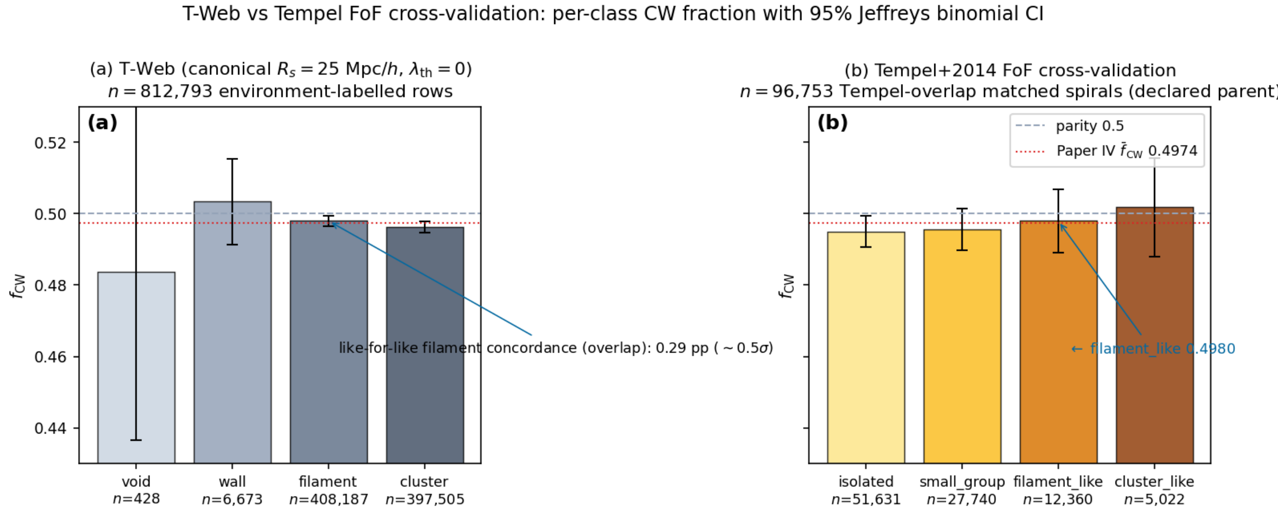

Figure 9. T-Web vs Tempel+2014 FoF cross-validation: per-class CW fraction with 95% Jeffreys binomial credible intervals, shared y-axis [0.43, 0.53]. *(a)* T-Web full-sample canonical run (shown as reference). *(b)* Tempel+2014 FoF (96,753-spiral overlap). Dashed reference is parity $f_{\rm CW} = 0.5$; dotted-red reference is the Paper IV global $\bar{f}_{\rm CW} = 0.4974$ classifier-monopole offset. The quantitative concordance statistic is computed like-for-like on the common overlap sample (§9.2): Tempel filament_like $f_{\rm CW} = 0.4980$ ($n = 12{,}360$) vs T-Web filament-on-overlap $f_{\rm CW} = 0.5009$ ($n = 16{,}701$), a 0.29 pp ($\sim 0.5\sigma$) difference, statistically indistinguishable (supporting, not load-bearing; the focal cross-classifier validation is the on-DESI DESIVAST re-projection in §8). Lower-n classes scatter by counting statistics and classifier-definition mismatch (T-Web $\lambda_{\rm th} = 0$ vs Tempel discrete richness thresholds) and are consistent with the secondary T-Web non-detection.

than a single deterministic class assignment. ASTRA is methodologically *complementary* to T-Web (this paper) and T-Web (Ref. (12)): the latter two are deterministic tidal-tensor classifiers, ASTRA is a probabilistic positional-statistic classifier that quantifies per-object assignment uncertainty. ASTRA is published only on EDR while our T-Web run is on DR1; the ~ 175 deg^2 EDR rosettes are contained within the DR1 footprint, so a per-galaxy cross-match by `TARGETID` is available in the EDR-overlap subsample and is reported in §10. The BGS-anchored volume-filling-fraction calibration in Ref. (13) is consistent with the T-Web sheet/filament fractions reported here within the survey-shell systematic discussed above.

A complementary public DR1 product, DESIVAST (14) (Rincón *et al.* 2025, ApJ 982, 38), is specifically a *void catalog* (not a full cosmic-web classifier) and is the input to the focal chirality-in-voids analysis reported in §8 above; see there for the per-catalog usage, cross-match, and three-algorithm robustness analysis.

10. ASTRA EDR PER-OBJECT CROSS-VALIDATION

The ASTRA-DESI EDR probabilistic environment catalog (13) (Zenodo 10.5281/zenodo.19358024) provides per-galaxy void / sheet / filament / knot membership probabilities $\{P_{\rm void}, P_{\rm sheet}, P_{\rm filament}, P_{\rm knot}\}$ on the $\sim$ 175 deg^2 EDR rosettes ($N_{\rm ASTRA}$ = 648,428 unique `TARGETID`s spanning BGS_ANY, LRG, ELG, and QSO tracers). We perform a per-galaxy `TARGETID` join against the P5 matched-spiral deduplicated-primary subsample and against the T-Web environment catalog of §4, recovering $N_{\rm overlap}$ = 25,186 spirals that carry all three labels: chirality classification (P4), ASTRA per-class membership probabilities (this section), and T-Web deterministic class assignment (§4). This is an EDR-overlap per-galaxy cross-check of the T-Web canonical classifier against the ASTRA published DESI environmental catalog within this campaign and is the closest currently available substitute for the full-DR1 environmental VAC discussed in §13. The cross-match pipeline and result summary are available in the companion data repository.

We compute the chirality-by-environment $f_{\rm CW}$ statistic on the 25,186-galaxy overlap under three classifiers run on the *same galaxies*: (i) the ASTRA argmax classifier (`env_class` = argmax over the four ASTRA probabilities); (ii) the ASTRA entropy-weighted classifier (each galaxy contributes $P_{\rm class}$ fractional count and $P_{\rm class} \cdot \mathbb{1}_{\rm CW}$ fractional CW count to each class, with sub-class variance $\sum_i P_i^2/4$ under the Bernoulli-0.5 null; this variance model assumes independence across objects and neglects the within-object negative correlation among the four class weights, which sum to one — an approximation adequate for the per-class σ quoted here but one that slightly mis-states the joint variance structure if classes are combined or compared; a 10^4-draw

Monte Carlo using the actual per-object probabilities under the independent Bernoulli-0.5 null reproduces the analytic per-class standard deviations to within 1.2% and the per-class σ values to <0.02, while directly measuring the neglected between-class coupling — class-sum correlations up to +0.42 from shared objects — so the approximation is validated at the per-class level used here, [A9]); and (iii) the T-Web deterministic classifier restricted to the same overlap, for like-for-like comparison.

The secondary diagnostic statistics, filtered to classes with $n \geq 100$ to suppress small-sample artifacts, are summarized in Table 22. Both ASTRA classifiers and the T-Web classifier-on-overlap recover the same conclusion: chirality is statistically indistinguishable from $f_{\rm CW} = 1/2$ across the four cosmic-web classes, with no class reaching the Bonferroni-corrected significance threshold at $\alpha = 0.01$, $K = 4$ ($|\sigma|_{\rm Bonf} = 3.02$).

The per-galaxy classifier agreement between T-Web and ASTRA argmax is *poor* on this overlap subsample. ASTRA argmax distributes the 25,186 spirals as 11.9% void / 31.7% sheet / 35.2% filament / 21.3% knot, while T-Web puts essentially the entire sample into filament (31.7%) and cluster (68.3%), with only 3 spirals total in the T-Web void + wall classes. (The repeated 31.7% is a numerical coincidence, not a copy error: ASTRA sheet = 7,980 and T-Web filament = 7,972 of the 25,186-spiral overlap, per the per-object artifact.) This reflects the survey-shell density-grid systematic discussed in §9.3: the 25.9 Mpc/h cell size in the T-Web 256^3 grid is comparable to the EDR rosette transverse extent, so the EDR-overlap subsample falls disproportionately on cells where the edge-density mask suppresses the T-Web void class, while ASTRA operating natively on EDR rosettes resolves void structure at sub-rosette scales. The two classifiers therefore disagree substantially on the per-galaxy environment label.

Despite this strong classifier disagreement on *per-galaxy environment assignment*, a chirality-vs-environment non-detection is recovered by both: $f_{\rm CW}$ does not vary by more than $\sim$2 pp across the four classes under any of the three classifiers, and no class clears the Bonferroni-corrected significance threshold. This is a supporting diagnostic consistency check: the EDR-overlap non-detection does not depend on which independent, published DESI environmental classifier is applied to the EDR-overlap subsample (restricted to the $\sim 175\,\deg^2$ EDR rosettes, $N_{\rm overlap} = 25{,}186$ spirals), and the deterministic single-class T-Web assignment reaches the same conclusion as the probabilistic ASTRA classifier even though the two classifiers assign vastly different per-galaxy class labels. Given the small overlap size and the strong per-galaxy label disagreement, this result is best read as a descriptor of consistency on the EDR subsample, not as load-bearing robustness evidence.

We note that the ASTRA EDR per-object overlap is restricted to the $\sim 175\,\deg^2$ EDR rosettes ($N_{\rm overlap} =$ 25,186), and that T-Web and ASTRA argmax disagree strongly on per-galaxy environment labels on this overlap; the result is therefore best read as: the EDR overlap recovers the same null result under either classifier despite per-galaxy label disagreement, consistent with the catalog-monopole offset already present at the catalog-wide level (Paper IV), rather than as a new independent detection. We list it alongside (i) DESIVAST per-galaxy cross-match, §8.1; (ii) within-class density quartile null, §6.5; (iii) DESIVAST-anchored void classifier; (iv) three-algorithm DESIVAST robustness; (v) catalog-native V2 GALZONE membership; (vi) MAXIMAL voids HEALPix sky-position stratification, with the caveat that the ASTRA overlap is the smallest subsample in this list and the T-Web/ASTRA per-galaxy label disagreement caps its independent statistical weight.

11. SYSTEMATICS AND NULL TESTS

We run six classes of systematics tests: chirality-label shuffle (1,000 permutations, applied per-bin in the redshift, density, and HEALPix scans of §6, including the leg×program-stratified variants), sky-position permutation, confidence-threshold sweep, match-radius sweep, footprint split, and target-class split. Table 23 reports the measured CW fraction per split with its N (artifacts in [A23]). The match-radius sweep is flat to 0.02 pp across $\{0.5, 1, 2, 3, 5\}''$ (Table 23 prints the two extreme radii; the intermediate-radius rows are carried in the committed artifact); the footprint splits sit within 0.13 pp of the global value; the confidence-threshold sweep drifts by at most -0.24 pp from the full-sample value at $p^{\rm max}_{\rm cls\_eq} \geq 0.7$ (a $\approx$2.1σ shift against the $0.5/\sqrt{n}$ counting floor at the reduced $n = 185{,}719$, below the 3σ bar applied throughout this section); and the target-class split is the one structured residual: BGS-bright $f_{\rm CW} = 0.4970$ vs LRG/ELG/QSO-dark 0.5051, a 0.81 pp difference ($|z| = 1.95$ unique-galaxy two-sample) with opposite-signed deviations from half. The bright/dark difference is the $\sim 2\sigma$ residual structure analyzed at the per-class level in §6.2. This residual has not been shown to leave the focal DESIVAST result unaffected: the DESIVAST-anchored void/non-void contrast (§8) is constructed on the volume-limited BGS low-z parent ($z \leq 0.24$), where the bright BGS path is separately tabulated and the target-program mixing that drives the filament bright/dark sign-flip is minimized by

Table 22. ASTRA EDR per-object cross-validation, secondary statistics on the $N_{\rm overlap} = 25{,}186$ EDR-overlap matched-spiral subsample. Range and max-$|\sigma|$ filtered to classes with $n \geq 100$ (*T-Web void $n = 1$ and wall $n = 2$ are below threshold and excluded from range and max-$|\sigma|$). The entropy-weighted row lists effective (probability-weighted) $n_{\rm eff}$ per class; per-class $n_{\rm CW}$ values are in the released per-object artifact ([A22]).

Classifier	$f_{\rm CW}$ range (pp)	max $\|\sigma\|_{\rm vs\,1/2}$	per-class n (void/wall/fil./cl.)
T-Web on same overlap	1.08	2.68	1* / 2* / 7,972 / 17,211
ASTRA argmax	2.08	2.25	2,985 / 7,980 / 8,864 / 5,357
ASTRA entropy-weighted	1.17	2.00	3,338 / 7,724 / 8,433 / 5,691

construction; the separate footprint-restricted $\Delta f_{\rm CW} = +0.0018$ (and its same-verdict $k=20$ sensitivity control $+0.0007$) is a secondary sensitivity rather than the focal estimate, and the A43–A44 interaction calculation finds no robust interaction evidence. Its sparse DARK and other-program strata provide only weak bounds, however, so substantial program-by-environment interaction effects are not excluded. No test produces a $> 3\sigma$ residual after Paper IV-monopole correction.

12. DISCUSSION

12.1. *Interpretation*

The secondary cosmic-web diagnostic is most cleanly read as a non-detection: the per-environment CW fractions cluster at the catalog-wide $f_{\rm CW} \approx 0.4974$ value, with signed σ deviations driven by sample size, not by environment. The Phase 2 sweep gives the same null verdict across the probed T-Web hyperparameter choices; it does not establish numerical invariance. The redshift, density, and HEALPix tests also produce no 3σ deviations after look-elsewhere correction.

T-Web status: secondary diagnostic. The T-Web cosmic-web classification is an *explicitly secondary, diagnostic* analysis in this paper and is **not** presented as load-bearing evidence. The T-Web secondary's void bin ($n = 428$) is sample-size limited, contaminated by the DESIVAST-vs-T-Web void-fraction discrepancy (+8–18 pp excess; §9.3), and the randoms-weighted completeness rebuild changes the T-Web class of 73.4% of matched spirals overall, while collapsing the void volume fraction (23× radial-selection contamination; §6.2). The T-Web run is carried forward as a multi-classifier consistency check and Phase 2 hyperparameter-stability test, not as a comparable inference to the focal released-parent estimate. The focal evidence is the released-parent DESIVAST analysis (§8.3); the other intervals and perturbations are reported separately as sensitivities.

12.2. *Empirical scope*

Within the published literature reviewed for this analysis, we identify no bounce or inflation model predicting this specific classifier-labelled, redshift-space estimand. The result therefore does not discriminate those model classes. The released-parent cluster-sandwich interval is a sampling statement for the focal contrast; the other perturbations answer different sensitivity questions and are not pooled. Classifier accuracy and environment-stratified confusion checks are retained in Appendix A to delimit label interpretation, not to de-attenuate the result into a physical exclusion.

12.3. *Comparison to Shamir 2022 DESI Legacy*

Shamir 2022 (10) reported a $\sim 2-4\%$ large-scale asymmetry on $\sim 1.3 \times 10^6$ Ganalyzer-classified galaxies. Paper IV finds the catalog-wide CW-fraction offset is -0.26% and the full-sky dipole amplitude $|A| < 0.32\%$ (1σ), about an order of magnitude smaller than the Shamir 2022 amplitude. The present paper's per-environment CW fractions sit at ~ 0.497 with inter-class range 1.98 percentage points across the four T-Web classes (per Table 8 canonical run; across the nine $(R_s, \lambda_{\rm th})$ Phase 2 sweep cells the per-class monopole-subtracted residuals stay below 1.64σ (resolved cells; $R_s = 10$ excluded) and the filament/cluster fractions move by only ∼0.1 pp, §7), leaving no room for a residual environment-dependent chirality of the Shamir 2022 amplitude (2–4 pp would be required in at least one well-populated class). We emphasize the scope of this comparison: the present null constrains an *environment-conditioned* chirality asymmetry of the Shamir 2022 amplitude; it does not by itself adjudicate Shamir's *global* (full-sky dipole) anisotropy claim, which is addressed separately in the companion Paper IV analysis quoted above.

13. LIMITATIONS

- The cross-match is selection-limited: the 8.47 M chirality catalog is flux-limited at $r \leq 17.8$ in the DESI Legacy regime; DESI spectroscopic targets extend much fainter.
- Projected $k = 5$ NN density is a coarse proxy for 3D density and cannot distinguish chance line-of-sight associations from true overdensities without

Table 23. Systematics splits: measured CW fraction per split (full sample $f_{\rm CW} = 0.49719$, n = 791,635). Match-radius rows count pre-dedup chirality-relevant matched rows (828,457 at the primary 1.0″ radius), so their n exceeds the deduped full sample; all other splits use the deduped one-row-per-`TARGETID` convention.

Test	Split	n	$f_{\rm CW}$	$\sigma_{\rm from\ half}$
Match radius	0.5″	820,266	0.4972	−5.07
	5.0″	868,165	0.4972	−5.22
Footprint	north (BASS+MzLS)	253,821	0.4971	−2.92
	south (DECaLS)	535,890	0.4972	−4.10
	DES-only	1,924	0.4958	−0.37
Confidence	≥ 0.4	787,279	0.4971	−5.15
	≥ 0.6	232,014	0.4954	−4.43
	≥ 0.7	185,719	0.4948	−4.48
	≥ 0.8	153,879	0.4950	−3.92
Program	bright (BGS)	775,760	0.4970	−5.28
	dark (LRG/ELG/QSO)	14,782	0.5051	+1.24
	backup + other	1,093	0.5105	+0.69

spectroscopic confirmation across the neighbourhood.

- T-Web is one of several cosmic-web finders; we cross-validated against the independent Tempel *et al.* 2014 (11) FoF group classifier (§9.2). The like-for-like filament class concordance on the common overlap is 0.29 percentage points ($\sim 0.5\sigma$, statistically indistinguishable); lower-n classes scatter by counting statistics and classifier-definition mismatch.

- *Unmodelled target-program leakage; a program-by-environment interaction is not excluded.* The single largest structured residual in the catalog is the DESI target-program split: BGS-`bright` $f_{\rm CW} = 0.4970$ against LRG/ELG/QSO-`dark` 0.5051, a 0.81 pp difference at $|z| = 1.95$ on unique galaxies (§11), and T-Web class is *not* independent of that split ($\chi^2 = 4933$, Cramér's $V = 0.078$; §6.5). Two bounds on how far this propagates into the focal contrast are reported and both are partial. (i) The *marginal*-mixture term is small by construction — the void and non-void arms differ by only 0.12 pp in dark fraction, so the induced $\Delta f_{\rm CW}$ scale is ≈0.001 pp — but this is not a maximum leakage bound and does not constrain an interaction. (ii) The explicit void-by-program interaction fit [A43–A44] finds no robust interaction evidence, but its `dark` stratum carries only $n = 237$ rows and its 95% CI on the `dark`-minus-`bright` contrast, $[-0.06637, +0.26190]$, is far wider than the focal interval; the `other` stratum occupies a single NSIDE= 4 block and admits no angular cluster inference at all. Substantial program-by-environment interaction effects are therefore *not excluded*, and the focal DESIVAST result has not been shown to be unaffected by this residual. The semi-analytic forward-leakage injection (Table 11, [A47–A48]) forward-reproduces at least ∼3/4 of every large raw deviation (77–133% across rows, all residuals non-significant), including 88% of the filament `bright`-vs-`dark` sign-flip, from the committed per-program classifier monopoles alone; it is a bounded surrogate and does *not* replace the definitive end-to-end injection–recovery test, which requires a DR2-grade selection-function mock and is explicitly deferred (§6.5, §14). Readers should treat the focal non-detection as conditional on that unclosed systematic.

- *Relation to the companion Paper IV catalog.* The per-galaxy `class_eq` CW/CCW labels and the global classifier-monopole calibration ($f_{\rm CW}^{\rm P4} = 0.4974 \pm 0.000279$) are *inputs* taken from the companion catalog paper Paper IV (3), which is publicly archived on Zenodo under DOI 10.5281/zenodo.21461899; not peer reviewed; the catalog labels and trained weights are public now under CC-BY-4.0. Since 2026 July 20 the Paper IV manuscript itself is public and permanently citable: the Zenodo record carries its full text, LaTeX source, and submission tarball under a version DOI, so a referee can read the companion analysis and inspect its label provenance without privileged access. That record is a public permanent archive — not an arXiv preprint and not a peer-reviewed publication; Paper IV has not been refereed, and the P5 inputs still have to be re-verified against that archived frozen release. This residual dependency is real, it is not a substitute for the bounded P5 analysis, and we state its scientific reach explicitly. The *headline* void/non-void $\Delta f_{\rm CW}$ contrast depends only on the public per-galaxy labels and is algebraically invariant under any catalog-wide monopole shift (§2), so it is refereeable from public GZ1/DESI/DESIVAST data and robust to the Paper IV *monopole amplitude, its uncertainty, and any future revision of that amplitude*; the classifier architecture, training, parity-equivariance validation, and monopole origin are reproduced for self-contained assessment in Appendix A. The one remaining Paper IV-linked element is the *per-galaxy label provenance itself* — and even this is validated model-independently: Paper IV's parity null survives replacing the learned CW/CCW labels entirely with Galaxy Zoo 1 human votes (no learned model in the chirality-label chain), returning $z = -0.54\sigma$ on $N = 46{,}017$ human-labeled spirals (3), so the labels do not inherit their pseudo-labeling. A systematic *environment-dependent* re-labeling by a future classifier is not excluded by any test internal to P5. We now bound this directly: a committed GZ1-overlap human-vs-classifier CW/CCW confusion matrix (App A; [A31]) shows the label-error asymmetry is consistent with zero to within $\pm$0.5–0.6 pp (95%) both globally and within every imaging-leg and confidence stratum, so any environment-differential mislabelling would have to be an environment-specific asymmetry absent from the sky and confidence cuts tested. The void/non-void stratum is now measured directly using the P5 matched-chirality$\times$DESI-redshift catalog and the DESIVAST void spheres, built with the paper's exact focal recipe (1.0$''$ match, `ZWARN`$=0$, `SPECTYPE` GALAXY/QSO, $z \le 0.24$, VoidFinder point-in-sphere footprint-restricted; `P5_VOID=1`): it finds *no* detectable void/non-void difference in the directional error-asymmetry (void $N = 933$, -0.023; non-void $N = 5{,}778$, -0.005; difference -0.018, $z = -0.89$, $p = 0.37$), a null that holds across all three void definitions (all-low-z $p = 0.25$, REVOLVER $p = 0.66$, VIDE $p = 0.19$). This measurement *corroborates* the symmetric-error premise on the very axis this paper constrains, but the void-arm 95% CI half-width ($\pm$3.7 pp) exceeds the paper's $\Delta f_{\rm CW}$ bounds (0.2–0.6 pp) by nearly an order of magnitude, so this stratum alone cannot exclude an environment-dependent label bias at the headline scale; the de-attenuation caveat of §13 therefore stands. And the monopole-referenced $\sigma_{\rm pred}$ diagnostics (not the headline contrast) reference the Paper IV scalar; we flag both explicitly separately and note the focal result must be re-verified against the archived Paper IV catalog of record (Zenodo DOI 10.5281/zenodo.21461899); Paper IV carries no arXiv identifier.

- Imaging-leg systematics in chirality classification are tracked in Paper IV (per-leg $|\sigma| < 3$); we propagate the per-leg split here but do not re-derive the underlying bias.

- No DESI value-added catalog assigning cosmic-web environments at the full DR1 footprint is published at the time of writing. The ASTRA-DESI EDR probabilistic environment catalog (13) restricted to the $\sim 175\,\deg^2$ EDR rosettes is the closest published independent classifier and is cross-matched per-galaxy against our T-Web run in §10; a full-DR1-footprint published VAC remains a desirable future input that would let us replace T-Web as the canonical classifier rather than only cross-validate it in the EDR-overlap subset.

- T-Web uses observed redshift-space galaxy positions. Kaiser squashing and finger-of-god elongation can change the tidal-tensor eigenvalue ordering near class boundaries (5; 6; 7). The scalar and first-order displacement exercises reported here do not rerun the density field and do not quantify that anisotropic channel. T-Web is therefore a secondary redshift-space diagnostic only; its binomial intervals omit cosmic variance and spatial covariance.

14. FUTURE SURVEY EXTENSION

Rubin/LSST is designed to provide deep, wide-field multiband imaging and public data products (2). A future overlap with DESI could support an independent morphology-label catalog and a preregistered replication of the released-parent estimand. We make no numerical claim for the resulting matched sample or uncertainty: both depend on the released overlap, selection functions, label validation, and the successor void catalog. The essential improvement is methodological, not a projected factor—freeze the estimator and thresholds before reading the contrast, use released catalog-native memberships, and propagate spatial covariance appropriate to the released footprint.

15. CONCLUSIONS

The released-parent DESIVAST analysis finds no detectable difference in classifier-labelled CW fraction between its void and non-void arms. For $N = 145{,}766$ GALZONE rows with `OUT`$= 0$, the focal linear-nuisance non-void-minus-void contrast is $+0.00145442$ with coarse HEALPix NSIDE$= 4$ CR1 cluster-sandwich SE $= 0.00331502$, 95% CI $[-0.00504290, +0.00795174]$, and normal $p = 0.66085$; the null-imposed wild-cluster score gives $p = 0.67345$. Overlap weighting gives a consistent sensitivity result.

This estimator became the focal descriptive estimate after review and after inspection of the results. The analysis is therefore exploratory, post-hoc, and not preregistered. The author-defined any-hole result ($N_{\rm void} = 57{,}081$), alternate DESIVAST memberships, T-Web, Tempel, and ASTRA paths are sensitivities or secondary diagnostics. They are not combined into a physical constraint or an exclusion. T-Web intervals omit cosmic variance and spatial covariance; the DESIVAST perturbations do not rerun the void finder in reconstructed space. One systematic remains open rather than bounded: the 0.81 pp BGS-`bright`-vs-`dark` target-program residual ($|z| = 1.95$) sits on a target split that is not independent of environment class ($\chi^2 = 4933$), and while the marginal-mixture term is $\approx$0.001 pp and the [A43–A44] fit finds no robust interaction, its sparse `dark` stratum ($n = 237$) leaves substantial program-by-environment interaction effects unexcluded. The definitive end-to-end injection–recovery mock is deferred to DR2 (§13), so the focal non-detection is conditional on that unclosed systematic. All conclusions concern classifier labels and released redshift-space environment assignments only.

Paper IV supplies the labels and remains a publication dependency; its manuscript, labels, and weights are now publicly archived and independently reviewable (Zenodo DOI 10.5281/zenodo.21461899, CC-BY-4.0; not peer reviewed), and P5 must be re-verified against that archived release before submission. A future confirmatory analysis should preregister the released-parent estimand and covariance procedure before inspecting a new survey contrast.

ACKNOWLEDGMENTS

This research used data obtained with the Dark Energy Spectroscopic Instrument (DESI) (1), including Data Release 1 and the DESIVAST value-added catalog. DESI construction and operations is managed by Lawrence Berkeley National Laboratory. This material is based upon work supported by the U.S. Department of Energy, Office of Science, Office of High-Energy Physics, under Contract No. DE–AC02–05CH11231, and by the National Energy Research Scientific Computing Center, a DOE Office of Science User Facility under the same contract. Additional support for DESI was provided by the U.S. National Science Foundation (NSF), Division of Astronomical Sciences under Contract No. AST-0950945 to the NSF's National Optical-Infrared Astronomy Research Laboratory; the Science and Technology Facilities Council of the United Kingdom; the Gordon and Betty Moore Foundation; the Heising-Simons Foundation; the French Alternative Energies and Atomic Energy Commission (CEA); the National Council of Humanities, Science and Technology of Mexico (CONAHCYT); the Ministry of Science and Innovation of Spain (MICINN), and by the DESI Member Institutions: https://www.desi.lbl.gov/collaborating-institutions. The DESI collaboration is honored to be permitted to conduct scientific research on I'oligam Du'ag (Kitt Peak), a mountain with particular significance to the Tohono O'odham Nation. Any opinions, findings, conclusions, or recommendations expressed here are those of the author and do not necessarily reflect the views of the listed funding agencies.

AI-assisted methodology. AI coding and review tools assisted pipeline execution and manuscript preparation under the author's direction. The author verified the reported quantities against the versioned code and artifacts listed in §C and Appendix D, made all scientific judgments, and takes full responsibility for the content.

APPENDIX

A. PAPER IV CLASSIFIER: SELF-CONTAINED METHODOLOGY SUMMARY

This paper consumes two inputs from the companion Paper IV (3): the per-galaxy `class_eq` CW/CCW labels and the single catalog-wide CW-fraction monopole scalar $\Delta f_{\rm CW}^{\rm P4} = -0.0026$ (§2). We stress at the outset the *degree* of that dependence, because it bounds how much the present conclusions can be affected by the not-yet-refereed status of the companion Paper IV (publicly archived on Zenodo under DOI 10.5281/zenodo.21461899; not peer reviewed). The focal environmental result — the void-vs-non-void $\Delta f_{\rm CW}$ two-sample contrast — is *algebraically invariant* under any catalog-wide monopole shift (§2): it cancels in the difference and therefore does not depend on the Paper IV monopole *amplitude* at all, only on the per-galaxy CW/CCW *labels*. The monopole scalar enters solely the $\sigma_{\rm pred}$ diagnostics, where its 8% Paper-IV/present-paper spread is propagated and is shown below to leave every verdict unchanged; and the present paper independently re-measures the monopole within its own matched sample ($f_{\rm CW}^{\rm P5} = 0.49719$), so even that scalar is corroborated here without relying on the Paper IV number. The remaining dependence is thus on the label *quality*, whose equivariance, accuracy floor, and systematic origin we quantify below in full. Because Paper IV is publicly archived but has not yet been refereed, and to keep the present manuscript self-contained, we reproduce here the methodological facts a referee needs to assess the quality of those labels, the origin of the monopole, and the classifier's parity (CW/CCW) equivariance, so that the present manuscript can be evaluated without the Paper IV text in hand. All values are sourced from the Paper IV manuscript and its public artifacts (the archived manuscript, the released catalog, and the trained weights are all public under CC-BY-4.0, so both the companion text and the label inputs are independently inspectable now) and are quoted, not re-derived, here.

Architecture. The classifier is a flip-equivariant ViT-Small vision-transformer encoder with a two-way (CW/CCW) classification head, trained in PyTorch on 224×224 px three-band (grz) image cutouts at the DESI Legacy Survey pixel scale $0.262''$/px. Parity equivariance is imposed at inference by an explicit Z_2 horizontal-flip test-time augmentation (TTA): each galaxy is classified together with its mirror image and the CW/CCW posteriors are symmetrized, so a galaxy and its reflection receive exactly swapped probabilities by construction.

Training data and provenance limits. The exact historical training realization is not fully recoverable. The production-script reconstruction and immutable model-repository receipt support 26,616 labeled rows: 6,637 GZ1 high-confidence CW/CCW, 17,153 CE-ResNet high-confidence spirals, and 2,826 not-spiral rows, of which the script account assigns 826 to CE selection and 2,000 to synthetic examples, with a 21,293/5,323 train/validation split. Horizontal flips are generated on the fly for a training-only consistency loss and do not add dataset rows. Conflicting committed records report 26,626 total rows, 846 CE non-spirals, or 92.10% rather than 93.6878% validation accuracy. No retained object/split manifest, random-state record, or run receipt binds the named objects and stochastic realization to the checkpoint. No retained object-ID manifest establishes exclusion of the 6,637 GZ1 training rows from later overlap validation. These limitations follow the canonical Paper IV account and remain open provenance gates. The parent imaging is the Smith42/galaxies DESI Legacy DR8 sample.

Parity-equivariance validation. The Z_2 TTA enforces an exact flip-swap posterior correlation of 1.000 on held-out objects. The raw (pre-TTA) left/right label asymmetry of +1.576% is suppressed to −0.529% after equivariant symmetrization, a 2.98× reduction; the residual is the classifier monopole discussed below. Under the full D_4 dihedral group of rotations and reflections the mean CW posterior is stable to $|\Delta\langle p_{\rm CW}\rangle| < 0.0016$; the argmax label flips on 21.4% of borderline objects, which fall below the high-confidence threshold and do not enter the equivariant `class_eq` CW/CCW labels used in the present analysis. 59,515 high-confidence rows (2.9%) carry a `qc_flip_identity_violator` flag and are retained with the flag exposed.

Independent accuracy floor. Against GZ1 expert spiral-chirality labels on a 234,282-galaxy cross-match, the production classifier attains 69.91% binary CW-vs-CCW spiral accuracy with Cohen's $\kappa = 0.40$ (three-class CW/CCW/NS accuracy 58.7%); Paper IV quotes this as a conservative accuracy floor. This binary figure is evaluated on the spiral-vs-spiral (CW/CCW) subset only — the non-spiral (NS) class is excluded from both the accuracy test and the present environmental analysis, which uses exclusively the equivariant CW/CCW `class_eq` labels — so the floor is a like-for-like bound on the labels this paper actually consumes. The corresponding label dilution is folded into the injection-recovery sensitivity floors used when interpreting the present null.

Classifier-label scope. The 69.91% binary accuracy ($\kappa = 0.40$) means the classifier-labelled CW fraction is an attenuated proxy for the true physical handedness fraction: for a symmetric binary error rate $a \simeq 0.699$, a true environment-dependent contrast would be suppressed by a factor $\approx 2a - 1 = 2(0.6991) - 1 = 0.3982$ in the classifier-label statistic. We report this factor only to explain why a classifier-label contrast cannot be read directly as physical handedness. We do not de-attenuate the reported contrast or quote a physical-handedness constraint. We flag that the 0.3982 factor is exact only under the symmetric-error assumption. That assumption now has *direct empirical support at the tested strata*: a committed GZ1-overlap human-vs-classifier CW/CCW confusion matrix (3) ([A31]; script [A32]), built on the $N = 40{,}987$ confident-spiral overlap of Galaxy Zoo 1 Table 2 human votes with the equivariant `class_eq` labels, finds the two mislabelling rates err(CW → CCW) and err(CCW → CW) equal to within their errors: the error *asymmetry* err(CW → CCW) − err(CCW → CW) is +0.0001 overall (95% CI [−0.005, +0.006]), and remains consistent with zero within *every* imaging-leg stratum (BASS+MzLS +0.0042, [−0.006, +0.014]; DECaLS

-0.0020, $[-0.009, +0.005]$) and *every* classifier-confidence stratum (confidence$_{\rm eq} > 0.6$: -0.0019, $[-0.006, +0.002]$; ≤ 0.6: $+0.0065$, $[-0.013, +0.026]$). The overall CW/CCW accuracy is 0.912, rising to 0.961 at confidence$_{\rm eq} > 0.6$: the error *magnitude* varies across strata by nearly a factor of ten, yet the errors stay *parity-symmetric* in every one, so the symmetric-error premise of the $2a - 1$ de-attenuation is empirically satisfied on all sky and confidence cuts tested. (The 0.912–0.961 accuracy quoted here is measured on the confident-spiral GZ1 overlap; the more conservative floor accuracy $a \simeq 0.699$ is used only as a conservative label-quality floor. We import only the *symmetry* property — not the accuracy value — from the overlap sample, and the observed magnitude-independence of that symmetry across a ten-fold accuracy range is precisely why it is taken to transfer to the $a \simeq 0.699$ floor regime.) The void-stratified asymmetry is now measured directly. GZ1 Table 2 carries no redshift, so the void/non-void split of the overlap was built from the P5 matched-chirality×DESI-redshift catalog plus the DESIVAST void spheres to assign 3D void membership, using the paper's exact declared validation recipe ($1.0''$ nearest-neighbour match, `ZWARN`= 0, `SPECTYPE` in $\{\rm GALAXY, QSO\}$, $z \leq 0.24$, VoidFinder point-in-sphere footprint-restricted; `P5_VOID=1`; [A31], [A32]). The footprint-restricted validation stratum gives a void arm of $N = 933$ with error-asymmetry $-0.023\,[-0.060, +0.014]$ and a non-void arm of $N = 5{,}778$ with $-0.005\,[-0.020, +0.010]$; the two-proportion difference is -0.018 ($z = -0.89$, $p = 0.37$, $[-0.057, +0.022]$), i.e. *no detectable void/non-void difference in directional error asymmetry*, and this null is consistent across all three DESIVAST void catalogs (all-low-z $p = 0.25$, REVOLVER $p = 0.66$, VIDE $p = 0.19$). Two-sided reading: (a) the errors stay parity-symmetric on the void axis as on every other stratum, so any environment-differential label error would have to arise from an environment-specific asymmetry *absent* from every stratum measured here; but (b) the void-arm 95% CI half-width (± 3.7 pp) exceeds the paper's measured $\Delta f_{\rm CW}$ excursions (0.2–0.6 pp), so this measurement *corroborates but cannot by itself exclude* an environment-dependent label bias at the headline scale. A *systematic environment-dependent re-labeling by a future classifier is therefore not fully excluded*. Accordingly, the empirical result remains a classifier-labelled, fixed-redshift-space non-detection and is not mapped onto a physical-handedness contrast.

Catalog. The released catalog contains 8,474,531 galaxies (157 of 8,474,688 failed QC), of which 3,201,160 are classified spiral (1,592,107 CW, 1,609,053 CCW; 5,273,371 non-spiral). The 791,635 chirality-relevant matched spirals analyzed in the present paper are the DESI DR1 cross-match of the CW/CCW subset (§3).

Origin of the monopole. The catalog-wide CW fraction is $f_{\rm CW} = 0.497353\,(279)$, a -0.265% (-9.47σ) offset from exact parity. Paper IV traces this offset to the training labels rather than to the sky: the GZ1 human-vote subset itself carries a CW excess ($f_{\rm CW}^{\rm GZ1} = 0.4838$ versus the production 0.4974) that propagates through the CE-ResNet pseudo-labels into the ViT. Crucially, the offset is *spatially uniform* across seven independent redshift/sky slabs — a pure monopole, not a dipole — which is the signature of a classifier systematic rather than an astrophysical parity signal. The present paper independently re-measures this offset within its own matched sample, $f_{\rm CW}^{\rm P5} = 0.49719$ on 812,793 env-labeled rows, corroborating the Paper IV value to $\sim$8% (§8.7).

Pseudo-label independence (model-free control). Because the production labels are trained partly on CE-ResNet pseudo-labels, one might worry the handedness signal is an artifact of the pseudo-labeling rather than of the sky. Paper IV excludes this directly: replacing the learned CW/CCW labels *entirely* with Galaxy Zoo 1 human votes — so that no learned model remains anywhere in the chirality-label chain — reproduces the same clean parity null at $z = -0.54\sigma$ (per-pixel permutation rank-$p = 0.67$; $z = -0.55\sigma$ per-galaxy binomial) on $N = 46{,}017$ human-labeled DESI-matched spirals, under the identical HEALPix estimator and null construction as the headline (3). The catalog's parity behaviour thus does not inherit its pseudo-labels, which strengthens the case that the per-galaxy `class_eq` labels the present paper consumes are a faithful handedness measurement and not a learned-label artifact.

Imaging-leg bias. Per-imaging-leg (BASS+MzLS, DECaLS, DES) CW-fraction differences are modeled in Paper IV with weighted-least- squares leg-fraction templates; the best-fit leg-driven dipole amplitude is $A_p = 0.455\%$, separated there from the isotropic monopole. The present paper retains the per-leg provenance for the independent systematics split of §11.

Public availability. The per-galaxy labels are served as the `class_eq` column of bamfai/galaxy-chirality-catalog (CC-BY-4.0; the acquisition configuration pins catalog revision `1ba76bc7`, without asserting a named release tag); the trained weights are at bamfai/galaxy-chirality-v2. The companion Paper IV manuscript is itself publicly archived on Zenodo (version DOI 10.5281/zenodo.21461899; concept DOI 10.5281/zenodo.21461898; deposited 2026 July 20 under CC-BY-4.0), and that record carries its full text, LaTeX source, and submission tarball. The deposit is a public permanent archive: it is not an arXiv preprint and not a peer-reviewed publication, and no arXiv identifier for Paper IV is asserted here. The archived manuscript together with the catalog and weights named above are the public artifacts used by this analysis.

Sufficiency for the present analysis. The two quantities the present conclusions rest on are (i) the per-galaxy `class_eq` labels, whose equivariance and accuracy floor are quantified above, and (ii) the single monopole scalar, whose origin and spatial uniformity are established above and independently reproduced here. The headline void-vs-non-void $\Delta f_{\rm CW}$ two-sample contrast is invariant under any catalog-wide monopole shift (§2), so it depends on the labels but not on the monopole amplitude; the monopole enters only the $\sigma_{\rm pred}$ diagnostics, where its uncertainty is propagated. This appendix therefore makes the classifier-label environmental result of the present paper independently assessable from public data alone, without needing the companion Paper IV manuscript in hand — which is in any case publicly retrievable at the DOI above.

B. REFERENCE CONTINGENCY TABLES FOR THE T-WEB χ^2 TESTS

For independent recomputation of the T-Web class-homogeneity test ($\chi^2 = 3.55$, 3 d.o.f., $p = 0.31$) and the T-Web class × target-program test ($\chi^2 = 4933$, 3 d.o.f., Cramér's $V = 0.078$) quoted in the abstract and §6.2, we tabulate the 4×2 cell counts implied by the published per-class n, $f_{\rm CW}$, and bright-fraction values.

Table 24. 4×2 contingency table CW/CCW × T-Web class on the 812,793-row env-labeled parent. Cells are exact integers CW = $n_{\rm CW}$, CCW = $n - n_{\rm CW}$ taken directly from the committed artifact arrays ([A10]; `parent_env_superset.per_class`); $f_{\rm CW}$ is the exact ratio rounded to four decimals for display. Sum: $n = 812{,}793$. Row marginals CW = 404,111, CCW = 408,682 (cells sum exactly to these marginals; see [A24]). Pearson $\chi^2 = 3.55$ (3 d.o.f., $p = 0.31$) on the row-level parent under the homogeneity null.

Class	n	$f_{\rm CW}$	CW	CCW
Filament	408,187	0.4980	203,261	204,926
Cluster	397,505	0.4963	197,284	200,221
Wall	6,673	0.5034	3,359	3,314
Void	428	0.4836	207	221

Table 25. 4×2 contingency table T-Web class × target program (`bright/dark`) on the $n_{\rm bright+dark} = 811{,}609$ bright+dark subset of the env-labeled parent. Per-class n values are the bright+dark subset totals (not the full 812,793 env-labeled parent counts), and bright/dark cells are exact integers taken directly from the committed artifact arrays ([A10]; `T2_contingency_class_x_program.table`); $f_{\rm bright}$ is the exact ratio rounded to four decimals for display. Pearson $\chi^2 = 4933$ (3 d.o.f., $\log_{10} p \approx -1069$), Cramér's $V = \sqrt{\chi^2/n} = 0.078$.

Class	n	$f_{\rm bright}$	bright	dark
Filament	407,940	0.9663	394,181	13,759
Cluster	396,576	0.9893	392,342	4,234
Wall	6,665	0.9622	6,413	252
Void	428	0.9813	420	8

The cell-level integers above are exact counts from the committed artifact arrays ([A10]; drivers `05`–`09`) and sum exactly to the stated row marginals; the regeneration script [A25] prints these rows from the artifact and asserts the marginals ($n = 812{,}793$ for the CW/CCW table; $n_{\rm bright+dark} = 811{,}609$ for the class×program table) against the source JSON. The tabulated rows provide a reproducibility anchor; the χ^2 values are computed against the same artifact arrays.

C. DATA AND CODE AVAILABILITY

Data Availability Statement. All primary inputs are public. (i) DESI Data Release 1 redshifts: the `zall-pix-iron` healpix redshift catalog (Iron spectroscopic reduction, DR1), available from https://data.desi.lbl.gov/public/dr1/.

(ii) DESIVAST void value-added catalog: the DR1 public VAC release (DESIVAST_BGS_VOLLIM VoidFinder, V2-REVOLVER, and V2-VIDE FITS files, NGC+SGC caps) (14). (iii) Chirality catalog (Paper IV): the CC-BY-4.0 per-galaxy class_eq label catalog mirrored on HuggingFace at bamfai/galaxy-chirality-catalog (catalog revision 1ba76bc7, as pinned by the acquisition configuration). The Paper IV manuscript describing that catalog is publicly archived on Zenodo at DOI 10.5281/zenodo.21461899 (CC-BY-4.0, deposited 2026 July 20); the deposit is a public permanent archive, not an arXiv preprint and not a peer-reviewed publication. (iv) The analysis code, derived row archive, and provenance JSON form the current local release candidate identified by v0.1.147-2026-08-03. This manuscript does not assert that a matching public Git tag or DOI snapshot already exists; both must be created and verified before submission.

The companion data repository referenced throughout this paper is the versioned GitHub repository Hubify-Projects/bigbounce, directory [A26]; results quoted here correspond to release candidate v0.1.147-2026-08-03. The analysis tree is frozen for this candidate; all numeric results, tables, figures, and per-class counts quoted above are bound to the current release-candidate source bundle and its checksummed artifacts. No single older commit is claimed to regenerate additions made in later revisions, and no public immutable Git tag or DOI exists yet. All analysis drivers are committed under [A27] (catalog fetch, cross-match, per-analysis drivers 05–09, z-shell rebuild 16, and the verification recompute drivers 17–18, which include the DESIVAST point-in-sphere membership driver), with the T-Web grid pipeline and the Tempel cross-validation under [A28]. Numeric artifacts live under outputs/, results/, and env_finder/reports/ in the same directory, each with per-output provenance JSON. A DOI-minted archival snapshot is planned but is not claimed to exist in this release candidate. The canonical chirality catalog is mirrored on HuggingFace at bamfai/galaxy-chirality-catalog. DESI Data Release 1 is available from https://data.desi.lbl.gov/public/dr1/. The Phase 2 sweep per-cell statistics are in [A29] (declared-parent recompute).

Explicit artifact-availability statement. The historical full DESIVAST-join parquet previously cited for the broader sensitivity paths is not present in the current release tree; byte-identical historical provenance for that intermediate is therefore not claimed. Those sensitivity paths are regenerable from the public inputs and committed drivers, but not from a frozen copy of that absent file. The current local v0.1.147-2026-08-03 candidate directly retains: (i) the independently reconstructed 145,789-row catalog-native archive [A39] and its input/hash manifest [A40], which are sufficient to reproduce the released-GALZONE/VoidFinder selection-control analysis (145,766 rows after the declared $\texttt{OUT}=0$ cut), but do not encode every DESIVAST algorithm or the unavailable historical full join; (ii) committed T-Web configurations and summary reports referenced by [A3]/[A7]/[A28]; the canonical eigenvector/eigenvalue arrays themselves are not retained in the tracked release and must be regenerated from the public inputs and committed pipeline; and (iii) the per-cell Phase 2 sweep configurations (data/desi_env/phase2_sweep/, [A12]). These frozen retained artifacts are deterministically reproducible byte for byte. Reconstruction from public inputs additionally requires the committed stable ordering and tie-breaking contract: the audit shows that an unstable sort changes 22 parent rows and shifts the focal contrast by 3.09×10^{-5}. A seed alone is therefore insufficient. No immutable public v0.1.147-2026-08-03 tag or Zenodo DOI is claimed to exist yet; both are explicit pre-submission release tasks. For clarity on the companion-paper dependency: the focal DESIVAST void/non-void $\Delta f_{\rm CW}$ contrast is reproducible from public inputs alone (public DESI DR1, public DESIVAST v1.0, and the public CC-BY-4.0 Paper IV class_eq labels on HuggingFace), with no reliance on any private or not-yet-public companion artifact; only the monopole-referenced $\sigma_{\rm pred}$ diagnostics (not the headline contrast) reference the Paper IV monopole scalar, which is independently re-measured here. The Paper IV manuscript itself is publicly archived at Zenodo DOI 10.5281/zenodo.21461899 (CC-BY-4.0); that deposit is a public permanent archive, and Paper IV has no arXiv identifier and has not been peer reviewed.

Cluster-bootstrap provenance. The DP5-10 result and driver are archived as [A35] and [A36]. The locally materialized DESI FITS used for that recomputation has SHA-256 2d95ad99361039b556c402b49e0e7c84df5f00106dc5731d 44476a58b128b49b and reproduces every released-parent and focal-arm integer. Its bytes do not match the May sidecar's recorded raw hash 50031c9b..., and the current upstream object reports a later modification date. Because the historical per-row snapshot is not available, byte-identical row provenance to that May raw file cannot be independently attested. The exact 145,789-row catalog-native control archive first frozen for v0.1.130 remains unchanged and is reverified for the current release candidate as [A39], with file SHA-256 fe863dcd3d569d22a3792ac0f1ee273e e3148ef311302e2d7984ab714634e9fc; [A40] records its inputs and the DESIVAST source commit. This closes current-row provenance without retroactively asserting the unavailable May bytes.

REPRODUCIBILITY CHECKLIST

- Single config file: [A30].
- Per-output provenance metadata included in data release.
- Deterministic seed: `20260515`.
- All Phase 2 sweep cell configs persisted under [A12].

D. DATA ARTIFACTS

Note on numbering: the bracketed *artifact* IDs [A1]–[A48] in this appendix are the release-candidate data/code artifacts and are *distinct* from the bibliographic references [1]–[13], which appear in the separate References section; the "A" prefix marks every artifact ID to avoid confusion at the references/artifact-map boundary. Artifact IDs [A1]–[A48] used throughout this paper hyperlink to the following paths in the companion repository `Hubify-Projects/bigbounce` (candidate `v0.1.147-2026-08-03`; public tag pending). Each ID in the text identifies the file or directory at the URL shown below; links A37–A40 will resolve after the release-candidate commit is pushed.

Table 26. Artifact ID map. Paths A2–A30 and A33–A40 are within `pipelines/p5_desi_chirality/`; the prefix is omitted in the short-name column. A1, A31, and A32 point to the companion catalog pipeline (`pipelines/p2_chirality/`). Clicking any [AN] ID in the paper PDF opens the corresponding GitHub URL.

ID	**Repository path (short name)**
[A1]	`pipelines/p2_chirality/`
[A2]	`outputs/30_ext4_galzone_complement_contrasts.json`
[A3]	`env_finder/01_compute_vweb.py`
[A4]	`outputs/23_unique_parent_rebuild.json`
[A5]	`outputs/21_r23conf_meta_closures.json`
[A6]	`outputs/18_v0151_stratified_and_density.json`
[A7]	`env_finder/reports/01_volume_fractions.json`
[A8]	`outputs/20_v0151_covariate_regression.json`
[A9]	`outputs/22_r24conf_local_batch.json`
[A10]	`outputs/17_v0151_closure_recomputes.json`
[A11]	`outputs/27_ext1_logistic_program_control.json`
[A12]	`data/desi_env/phase2_sweep/`
[A13]	`outputs/26_r27conf_ess_recomputes.json`
[A14]	`outputs/24_r24conf_pod_session.json`
[A15]	`outputs/29_ext3_desivast_footprint_retabulation.json`
[A16]	`outputs/28_ext1_desivast_program_split.json`
[A17]	`outputs/25_completeness_weighted_rebuild.json`
[A18]	`scripts/16_cosmic_web_zshell_corrected.py`
[A19]	`outputs/16_cosmic_web_zshell_corrected.json`
[A20]	`outputs/19_v0151_zshell_geofootprint_check.json`

Table 27. Artifact ID map (continued). Paths A21–A30 and A33–A48 are within `pipelines/p5_desi_chirality/`; A31–A32 are in the companion catalog pipeline.

ID	Repository path (short name)
[A21]	`env_finder/03_tempel_cross_validation.py`
[A22]	`results/analysis_astra_per_object/ cw_fraction_by_env_astra.csv`
[A23]	`results/analysis_systematics/`
[A24]	`outputs/31_ext5_appendixB_tables.json`
[A25]	`scripts/31_ext5_appendixB_tables.py`
[A26]	`pipelines/p5_desi_chirality/`
[A27]	`scripts/`
[A28]	`env_finder/`
[A29]	`env_finder/reports/02_phase2_sweep.csv`
[A30]	`env_finder/config.yaml`
[A31]	`p2_chirality/outputs/gz1_stratified_confusion.json`
[A32]	`p2_chirality/scripts/gz1_stratified_confusion.py`
[A33]	`outputs/27_rsd_void_recon_bound.json`
[A34]	`scripts/27_rsd_void_recon_bound.py`
[A35]	`outputs/35_desivast_cluster_bootstrap.json`
[A36]	`scripts/35_desivast_cluster_bootstrap.py`
[A37]	`outputs/36_desivast_native_selection_control.json`
[A38]	`scripts/36_desivast_native_selection_control.py`
[A39]	`outputs/36_desivast_native_selection_rows.parquet`
[A40]	`outputs/36_desivast_native_selection_manifest.json`
[A41]	`scripts/38_focal_cluster_inference_sensitivity.py`
[A42]	`outputs/38_focal_cluster_inference_sensitivity.json`
[A43]	`scripts/39_focal_interaction_clustering_robustness.py`
[A44]	`outputs/39_focal_interaction_clustering_robustness.json`
[A45]	`analysis/global_multiplicity_bound_v0_1_140.py`
[A46]	`analysis/global_multiplicity_bound_v0_1_140.json`
[A47]	`analysis/forward_leakage_injection_v0_1_141.py`
[A48]	`analysis/forward_leakage_injection_v0_1_141.json`

REFERENCES

[1] DESI Collaboration, "Data Release 1 of the Dark Energy Spectroscopic Instrument," Astron. J. **171**, 285 (2026), doi:10.3847/1538-3881/ae4c43, arXiv:2503.14745.

[2] Z. Ivezić *et al.*, "LSST: From Science Drivers to Reference Design and Anticipated Data Products," Astrophys. J. **873**, 111 (2019), doi:10.3847/1538-4357/ab042c, arXiv:0805.2366.

[3] H. Golden, *An Observed-Label Chirality-Dipole Null in 949,584 High-Confidence DESI Spirals and an 8.5-Million-Galaxy Catalog*, companion catalog paper (Paper IV), Zenodo (2026), version DOI 10.5281/zenodo.21461899; concept DOI 10.5281/zenodo.21461898; deposited 2026 July 20 under CC-BY-4.0. Public permanent archive of the manuscript, LaTeX source, and submission tarball; not an arXiv preprint and not peer reviewed. The per-galaxy `class_eq` labels and trained weights consumed here are public under the same license (bamfai/galaxy-chirality-catalog).

[4] H. Golden, *The Exact Matter-Contraction Non-Gaussian Amplitude: Four-Vertex Derivation and Conditional Large-Scale-Structure Mapping*, companion paper (Paper II), Zenodo (2026), version DOI 10.5281/zenodo.21461881; concept DOI 10.5281/zenodo.21461880; deposited 2026 July 20 under CC-BY-4.0. Public permanent archive of the manuscript, LaTeX source, and submission tarball; not an arXiv preprint and not peer reviewed.

[5] O. Hahn, C. M. Carollo, C. Porciani, and A. Dekel, "Properties of dark matter haloes in clusters, filaments, sheets and voids," Mon. Not. Roy. Astron. Soc. **375**, 489 (2007), arXiv:astro-ph/0610280.

[6] Y. Hoffman, O. Metuki, G. Yepes, S. Gottlöber, J. E. Forero-Romero, N. I. Libeskind, and A. Knebe, "A kinematic classification of the cosmic web," Mon. Not. Roy. Astron. Soc. **425**, 2049 (2012), arXiv:1201.3367.

[7] M. Cautun, R. van de Weygaert, B. J. T. Jones, and C. S. Frenk, "Evolution of the cosmic web," Mon. Not. Roy. Astron. Soc. **441**, 2923 (2014), arXiv:1401.7866.

[8] N. Hamaus, P. M. Sutter, and B. D. Wandelt, "Universal density profile for cosmic voids," Phys. Rev. Lett. **112**, 041304 (2014), doi:10.1103/PhysRevLett.112.041304, arXiv:1307.2523.

[9] Planck Collaboration, "Planck 2018 results. VI. Cosmological parameters," Astron. Astrophys. **641**, A6 (2020), arXiv:1807.06209.

[10] L. Shamir, "Analysis of spin directions of galaxies in the DESI Legacy Survey," Mon. Not. Roy. Astron. Soc. **516**, 2281 (2022), doi:10.1093/mnras/stac2372, arXiv:2208.13866.

[11] E. Tempel, A. Tamm, M. Gramann, T. Tuvikene, L. J. Liivamägi, E. Saar, P. Heinämäki, P. Nurmi, and J. Einasto, "Flux- and volume-limited groups/clusters for the SDSS galaxies: catalogues and mass estimation," Astron. Astrophys. **566**, A1 (2014), arXiv:1402.1350.

[12] H. I. Ullah, M. Awais, T. Matos, and J. F. Suárez-Pérez, "Cosmic-web quenching with DESI DR1: T-Web environments and mass-dependent red/blue classification," preprint (2026), arXiv:2604.02463.

[13] D. C. Zapata-Zuluaga, S. Guevara-Montoya, V. Torres-Gomez, J. Hernandez, and J. E. Forero-Romero, "The Cosmic Web in the DESI Early Data Release: A Probabilistic Environment Catalog," (2026), arXiv:2604.01456.

[14] H. Rincón, S. BenZvi, K. A. Douglass *et al.*, "DESIVAST: Catalogs of Low-redshift Voids Using Data from the DESI Data Release 1 Bright Galaxy Survey," Astrophys. J. **982**, 38 (2025), doi:10.3847/1538-4357/adb559, arXiv:2411.00148.

[15] M. Walmsley *et al.*, Galaxy Zoo DESI: large-scale automated morphology classification of 8.7 million galaxies in the DESI Legacy Imaging Surveys, Mon. Not. R. Astron. Soc. **526**, 4768 (2023), arXiv:2309.11425.